Dipl.-Ing. Sandro Krauss

Response of the Earth's thermosphere during extreme solar events

A contribution of satellite observations to atmospheric evolution studies

DISSERTATION

Zur Erlangung des akademischen Grades
Doktor der technischen Wissenschaften

Doktoratsstudium der Technischen Wissenschaften
Doctoral School Geosciences, Class of Geodesy

Technische Universität Graz

Betreuer:
Univ.-Prof. Dr.techn. Mag.rer.nat. Roland Pail
Institut für Theoretische Geodäsie und Satellitengeodäsie

Graz, December 2012

Deutsche Fassung:
Beschluss der Curricula-Kommission für Bachelor-, Master- und Diplomstudien vom 10.11.2008
Genehmigung des Senates am 1.12.2008

EIDESSTATTLICHE ERKLÄRUNG

Ich erkläre an Eides statt, dass ich die vorliegende Arbeit selbstständig verfasst, andere als die angegebenen Quellen/Hilfsmittel nicht benutzt, und die den benutzten Quellen wörtlich und inhaltlich entnommenen Stellen als solche kenntlich gemacht habe.

Graz, am …… ……..
(Unterschrift)

Englische Fassung:

STATUTORY DECLARATION

I declare that I have authored this thesis independently, that I have not used other than the declared sources / resources, and that I have explicitly marked all material which has been quoted either literally or by content from the used sources.

…… ……..
date (signature)

Acknowledgement

First of all, I would like to take the opportunity to thank all colleagues which were involved in our joint Russian-Austrian project under the RFBR grant 09-02-91002-ANF-a and the Austrian Science Fund (FWF) grant I 199-N16. Special thanks to the project leaders Helmut Lammer and Yuri N. Kulikov who supported my thesis with their extensive knowledge and great ideas. In this context I want to mentioned that parts of the thesis were already published in the course of the project in Krauss et al. 2012.

I would also like to thank my supervisor Roland Pail who continued to support my thesis also after his change to the University of Technology, Munich. Furthermore, Bibiana Fichtinger who never ceased answering my enquiries concerning astronomical issues and Sean Bruinsma for providing me with the GRACE accelerometer calibration parameters.

Last, but definitely not least I want to thank my colleague Walter Hausleitner from the Space Research Institute in Graz with whom I have spent countless hours discussing problems and developing approaches to solutions.

Abstract

In this interdisciplinary study in the field of astronomy and geodesy the thermospheric response during extreme solar flares that irradiated the Earth's upper atmosphere is analysed. It is suggested that such events can serve as proxies for the intense electromagnetic and corpuscular radiation environment of the Sun and other stars during their early phases of evolution. Accelerometer measurements aboard the GRACE spacecraft are used too investigate the atmospheric density and its temporal and spatial variation. The measurements comprise the non-gravitational forces acting on the satellite, which is orbiting at an altitude of about 450 km. At that height level the atmospheric drag force, which depends on the atmospheric density is of particular interest. For this reason, the observations must be reduced by non-gravitational forces originating from the solar radiation pressure and Earth albedo. The density variations in the thermosphere are analysed over 7.5 years with a special focus on extreme solar events like the X17.2 flare during the so-called Halloween period in 2003 or the X2.0 flare in November 2004. Furthermore, a comparison with empirical thermosphere models like the NRLMSISE-00 and the Jacchia-Bowman 2008 is performed. Based on the additional analysis of EUV measurements from the TIMED satellite during these solar flares a connection between the acceleration measurements and theoretical studies related to thermospheric heating and expansion caused by the solar EUV flux is established.

Kurzfassung

In dieser interdisziplinären Studie auf dem Gebiet der Astronomie und Geodäsie werden die Auswirkungen von extremen Sonneneruptionen auf die obere Erdatmosphäre untersucht. Es wird angenommen, dass solche Ereignisse als Proxies für die Strahlungsintensität der Sonne und anderer Sterne in ihrer frühen Entwicklungsphase angesehen werden können. Um die zeitlichen und räumlichen Veränderungen in der atmosphärischen Dichte zu untersuchen, werden Beschleunigungsmessungen der Satellitenmission GRACE herangezogen. Die Messungen enthalten sämtliche nicht-gravitative Kräfte die auf den Satelliten in einer Höhe von ungefähr 450 km wirken. In dieser Flughöhe spielt vor allem der Luftwiderstand eine große Rolle. Aus diesem Grund müssen die Messungen zunächst um die Störkräfte ausgehend vom Strahlungsdrucks der Sonne und des Erdalbedo reduziert werden. Die Dichtevariationen in der Thermosphäre werden über einen Zeitraum von siebeneinhalb Jahren untersucht, wobei der Fokus auf extremen Sonneneruptionen, wie dem X17.2 Flare während der sogenannten Halloween Periode 2003 oder einem X2.0 Flare im November 2004, liegt. Desweiteren werden die berechneten Dichten mit jenen der empirischen Atmosphärenmodellen NRLMSISE-00 und Jacchia-Bowman 2008 verglichen. Basierend auf einer zusätzlichen Analyse von EUV Messungen des TIMED Satelliten wird eine Verbindung zwischen extremen Sonneneruptionen und früheren Studien über thermosphärische Aufheizungs- und Expansionsprozesse hergestellt.

Contents

List of Figures

List of Tables

LIST OF TABLES

Chapter 1

Introduction

The evolution of planetary atmospheres is closely related with the intensity of the solar radiation and the particle environment of the Sun or a planet's host star over time. Several previous studies [e.g., Zahnle and Walker, 1982, Guedel et al., 1997, Guinan et al., 2003, Ribas et al., 2005, Guedel, 2007, Claire et al., 2012] have shown that the young Sun was more active in the past than today. For this reason, it is important to study the related consequences this might have had for the development of planetary atmospheres [Lammer et al., 2012]. At present, there exist several theoretical atmosphere models [e.g. Kulikov et al., 2007, Tian et al., 2008a,b] which calculate exospheric temperatures and densities depending on the extreme ultraviolet (EUV) radiation level among other things. Based on in-situ measurements by the Gravity Recovery and Climate Experiment (GRACE; Tapley et al. [2007]) and observation based empirical models like the NRLMSISE-00 (MSISE-00; Picone et al. [2003]) and Jacchia-Bowman 2008 (JB08; Bowman et al. [2008]) it is attempted to validate the results from the theoretical models.

Thus, this thesis represents an interdisciplinary study of astronomy and geodesy that focuses on the response of the Earth's thermosphere during extreme solar flares, like the X17.2 solar flare which occurred during the so-called "Halloween period" in 2003. Therefore, a general overview of the Sun and its interaction with the Earth's environment is presented in Section 2.

In order to get information concerning the actual state of the Earth's upper atmosphere, accelerometer measurements recorded by the low Earth orbiter mission GRACE are investigated. Former studies [e.g. Bruinsma et al., 2006, Tapley et al., 2007, Sutton, 2008, Doornbos et al., 2009] have shown that these observations are suitable to investigate variations in the neutral density of the thermosphere. Referring to this, Section 3 describes how the accelerometer measurements are properly calibrated and which non-gravitational forces are part of the measurement.

In the subsequent Section it will be explained how the measurements can be used to deduce the

ambient neutral atmosphere densities. In this context, the variable drag coefficient and thus the gas-surface interaction is of major importance. Since the beginning of the space age numerous studies [e.g. Gustafson, 1958, Schamberg, 1959, Sentman, 1961, Cook, 1960, 1965] have dealt with this issue. The approach, which is used in this thesis to determine the drag coefficient is an analytical expression of Sentman's treatise elaborated from Moe and Moe [2005]. Based on the calculated dynamic drag force coefficient, the resulting neutral densities are analysed for several time periods including the Halloween flare in 2003.

A comparison between the estimated neutral densities from GRACE and those from the empirical thermosphere models MSISE-00 and JB08 is performed in Section 5. Thereby, periods of different solar activity levels are analysed and weaknesses of the empirical models, mainly due to the usage of daily averaged solar activity indices, are discussed.

Section 6 describes how a connection between extreme solar events and the Sun at a younger age and with a higher EUV radiation can be established. For this reason, the spectra of the X17.2 flare are investigated in the EUV range by using data from the Solar EUV Experiment (SEE) aboard the Thermosphere Ionosphere Mesosphere Energetics and Dynamics (TIMED) satellite. Afterwards, the analysed EUV enhancement due to the flare is compared with the EUV radiation of the quiet Sun during moderate solar activity. Based on these analysis, pseudo solar activity indices, which are related to the activity maximum of the flare event, are computed and used for a re-evaluation of the empirical thermosphere model JB08. The resulting thermospheric densities and exobase temperatures are then compared with results from the theoretical models by Kulikov et al. [2007], Tian et al. [2008a,b].

In a further step, the data records from the GRACE spacecraft (S/C) during a second solar flare which occurred in November 2004 are analysed. This solar event is particularly interesting since it happened at a time when the S/C observed the impact of the flare radiation without a large time delay. Thus, it offers the rare possibility to directly compare the in-situ measurements with the results from the theoretical models.

Finally, estimated exospheric temperatures from the empirical model JB08 and the theoretical models are compared for different EUV levels and the implications of the results for Earth-type N_2 atmospheres which are exposed to higher solar or stellar EUV fluxes are discussed.

Chapter 2

Space Weather

"Space Weather refers to conditions on the Sun and in the solar wind, magnetosphere, ionosphere and thermosphere that can influence the performance and reliability of space-borne and ground-based technological systems and can endanger human life or health. Adverse conditions in the space environment can cause disruption of satellite operations, communications, navigation and electric power distribution grids, leading to a variety of socioeconomic losses [Wright et al., 1995]."

Since the beginning of the space age in the early 1960's, space weather has been of major importance. Contrary to the weather on Earth, where all relevant processes happen in the troposphere up to an altitude of 20 km, space weather deals with the space environment starting in the thermosphere at approximately 90 km and extends all the way to the Sun.
The Sun continuously emits two types of energy into space, namely electromagnetic and corpuscular radiation [Moldwin, 2008]. The latter is what we call solar wind - the release of energetic charged particles, mostly protons and electrons, from the Sun's corona. This magnetised plasma also carries the Sun's magnetic field outward, forming the interplanetary magnetic field (IMF).
The following sections comprise a description of the Sun's environment, where space weather has its origin, and the Earth's atmosphere, which is influenced by radiation emitted from the Sun.

2.1 The Sun

The Sun is the star that is located in the centre of the solar system and contains 99% of the solar system's total mass [Hanslmeier, 2002]. The mean distance from Earth is approximately 1.49×10^8 km and defines one astronomical unit (AU). This distance is equivalent to 8.28 minutes in terms of the speed of light. The Sun has a radius $R_\odot$ of about 7×10^5 km, a mass $M_\odot$ of

1.99×10^{30} kg, and consists of hot plasma. Studies on nearby stars and meteorites led to the conclusion that the Sun is a typical star about 4.5 Gyrs old [Moldwin, 2008]. At that time it came to a hydrostatic equilibrium, which means that the gravity force, acting inwards, becomes equal to the pressure of gas which is pushing outwards. From a mathematical point of view this means that a rough estimate of the centre pressure p_c can be calculated, if we equate the gravitational acceleration g with an estimate for the centre pressure from the hydrostatic equation:

$$\frac{dp}{dh} = g\rho \sim \frac{p_c}{R_\odot}. \tag{2.1}$$

Using

$$g = \frac{GM_\odot}{R_\odot^2}, \tag{2.2}$$

the centre pressure can be written as

$$p_c = \frac{G\ M_\odot \rho}{R_\odot}, \tag{2.3}$$

where G indicates the gravitational constant ($G = 6.673 \times 10^{-11} \mathrm{m^3 kg^{-1} s^{-2}}$).
If we assume that the Sun is a perfect sphere, the density ρ can be calculated by

$$\rho = \frac{3\ M_\odot}{4\ \pi\ R_\odot^3}, \tag{2.4}$$

thus Eq. 2.3 yields a centre pressure of $p = 2.4 \times 10^{14}$ N m^{-2}. In order to get an estimate of the core temperature T_c, the ideal gas law can be used

$$T_c = \frac{m\ p_c}{\rho\ k}. \tag{2.5}$$

Here k denotes the Boltzmann constant ($k = 1.38 \times 10^{-23}$kg) and m the mass, which was assumed to be 0.84×10^{-27}kg, since the core consist mostly of hydrogen protons. Even if we assumed some simplifications in this example, we obtain a core temperature of 1.2×10^7K, which is actually quite close to the real core temperature of 1.5×10^7 K.
Due to these high temperatures, electrons are stripped from nuclei of atoms (mostly hydrogen). Hence, protons or nuclei of hydrogen are whipping around the core and from time to time two protons collide, starting a proton-proton chain reaction. Thereby, hydrogen is converted to helium plus energy. The generated photons travel from the centre of the star through the different layers of the Sun to the outer space. The structure of the Sun with its different regions is illustrated in Fig. 2.1. In the first step, the heat is transferred from the core through the radiation zone by ions of hydrogen and helium emitting photons (i.e. electromagnetic radiation that acts like discrete particles).

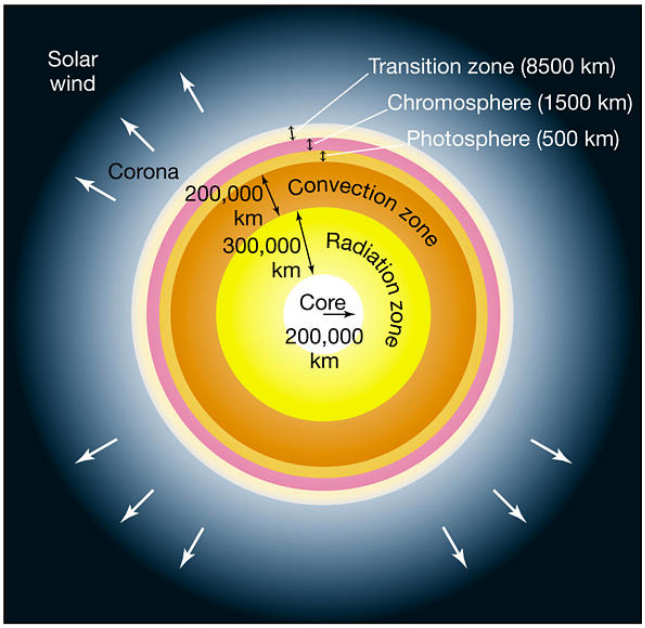

Figure 2.1: The main regions of the Sun ©Pearson Prentice Hall Inc. (2005).

In the convection zone, which extends from the surface to a depth of 2×10^5 km, the energy is transported through fluid motion. The temperature at the bottom of this zone is approximately 2×10^6 K due to the radiation coming from the radiative zone. Contrary to that, we have a significantly cooler surface temperature of about 5800 K. This large difference in temperature leads to a process called convection. This means, that the hotter and less dense gas rises to the surface, emits radiation and heat into space, and finally cools down and sinks again. However, due to the rotation of the Sun this convection process is rather turbulent than uniform.

Above the convection zone we find the photosphere, which in fact denotes the visible surface of the Sun. From this region the energy generated by the Sun is ejected into space. The surface of the photosphere is marbled with light and dark regions, which are called granules. They occur due to the convection currents in the underlying layer. The brighter parts mark the regions where the hotter and less dense plasma is located. The darker areas denote the cooler descending gas.

Above this region we find the chromosphere, the transition zone, and finally the corona. These regions are often referred to as the atmosphere of the Sun. The chromosphere is a layer of approximately 1500 km thickness with a temperature of about 20000 K. Since the density decreases rapidly to merely 10^{-4} of the photosphere density, the chromosphere is only visible during solar eclipses, when the moon blocks the bright photosphere [Moldwin, 2008]. It can be observed through the red visible spectral line Hα at a wavelength of 653.3 nm. This emission line is emitted at higher

temperatures by hydrogen atoms when an electron makes a transition to the second lowest energy level. Concerning the various wavelength and the related energy, Fig. 2.2 shows the electromagnetic spectrum ordered right-to-left from low to high energy. The relationship between the energy

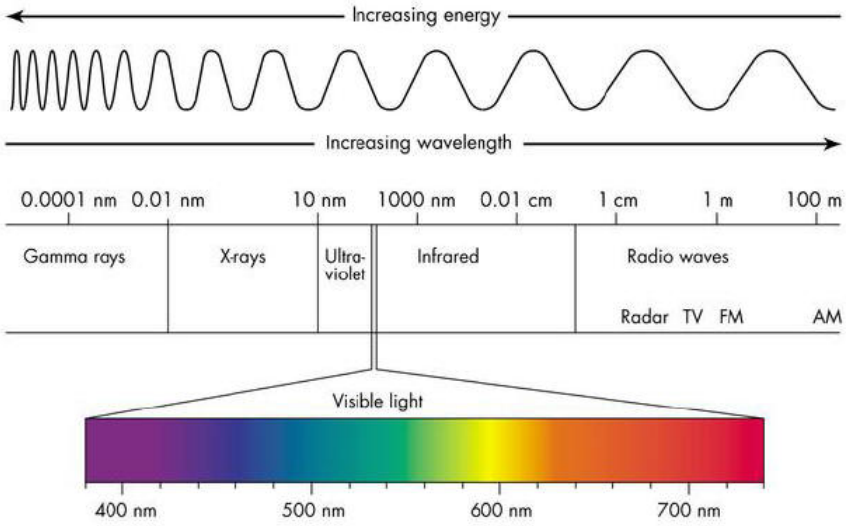

Figure 2.2: Electromagnetic spectrum ordered right-to-left from low to high energy.

of the electromagnetic radiation (E) and the frequency (f) can be expressed by

$$E = h \cdot f, \tag{2.6}$$

where h denotes the Planck's constant (6.626×10^{-34} J s).

In the left panel of Fig. 2.3 the thin red chromosphere of the Sun during a total solar eclipse is illustrated. The centre panel shows the solar corona, which can expand to millions of kilometres into space. Thus, the solar corona also denotes the outermost region of the Sun's atmosphere, where we find extreme high temperatures, up to some million degrees Kelvin. This is most likely due to induction by the Sun's magnetic field and sonic pressure waves from the regions below.

Based on the wavelength (i.e. colour), it is also possible to determine the temperature by applying Wien's displacement law

$$T \cdot \lambda_{max} = 2.898 \times 10^{-3} [\text{m K}], \tag{2.7}$$

which relates the emitted energy with the temperature of a black body radiator. According to Planck's law a black body is an idealised object, which absorbs all incident electromagnetic radiation, regardless of the intensity and wavelength. Since a body in thermal equilibrium emits the same amount of energy as it absorbs, a black body radiator is therefore also an idealised thermal

Figure 2.3: Left: reddish chromosphere during an solar eclipse in 1999, ©Luc Veatour; centre: solar corona, again during an total solar eclipse, ©NASA/John Walker; right: coronal loop observed by the TRACE satellite, ©NASA.

radiator, whereby the emission spectrum solely depends on the temperature. In short, when the temperature increases, also the energy increases, hence the radiation maximum occurs at shorter wavelengths.

Because of the open magnetic field lines, the corona continuously extends into outer space forming the solar wind. In so-called "active regions" coronal holes can be found. These structures in the lower corona and transition zone are associated with closed magnetic field lines that connect magnetic regions around sunspots on the solar surface [Hanslmeier, 2002]. The right panel in Fig. 2.3 illustrates a typical coronal loop observed by the TRACE[1] satellite. Through coronal loops the corona is involved in all phenomena which are linked to the magnetic field and occur at different altitudes of the Sun. In the following the Sun's magnetic field as well as phenomena like solar flares and coronal mass ejections (CME) are further described.

2.1.1 Solar Magnetism

The Sun's magnetic field is a dipole field, which means that a magnetic north and south pole is present. The orientation of the field is defined in such a way that the field lines point outward at the magnetic north pole and inward at the magnetic south pole. In the case of the Sun, the structure and orientation of the magnetic field changes over a period of 22 years. The complex magnetic field originates from strong electric currents within the star. Due to the high temperatures, the charged particles move around and create complex magnetic fields inside the Sun. Additionally, due to the differential rotation of the Sun, the plasma rotates slower at the poles than at the equator, resulting in field lines, which are wrapped around the Sun (see Fig. 2.4). Approximately every

[1] http://trace.lmsal.com/

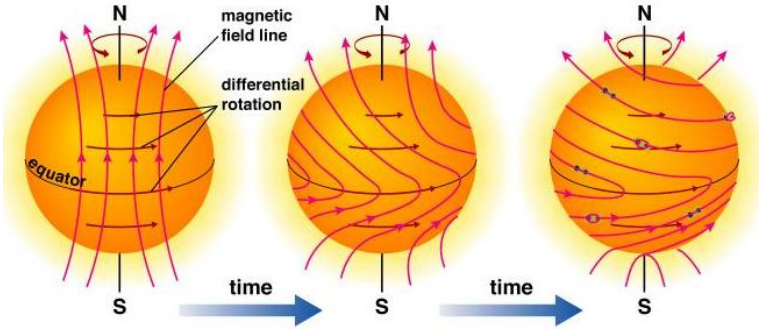

Figure 2.4: Illustration of the differential rotation of the Sun. ©Addison Wesley

11 years a pole reversal can be observed, which is associated with an increase in solar activity. This behaviour can be proven by illustrating the progress of the number of sunspots over a longer period of time. In Fig. 2.5 the number of sunspots is illustrated in a so-called "Butterfly Diagram". Such a diagram visualises not only the progress of the sunspot number, but also the equatorward

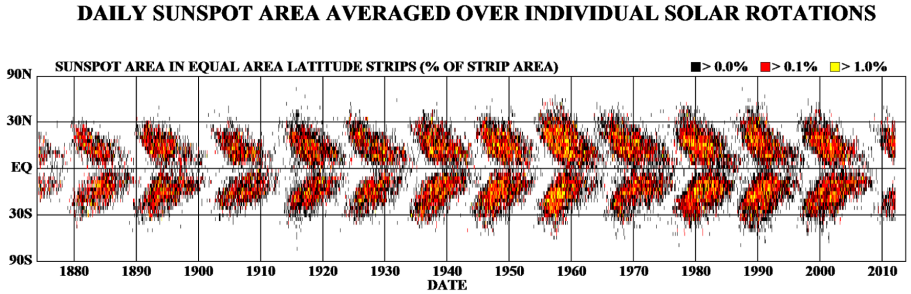

Figure 2.5: Sunspot numbers in a Butterfly-Diagram during the last 135 years. ©NASA

motion of the sunspots during an activity cycle. It depicts, that sunspots arise at latitudes of $\pm 30°$, have a maximum number and expansion around $\pm 15°$, and when the solar minimum is reached, they are located near the equator. Sunspots are darker regions within the photosphere having a much stronger magnetic field than the surrounding surface. The darker colour results from the fact that these regions are slightly cooler compared to the surrounding photosphere (about 4500 K versus 5800 K). Figure 2.6 displays sunspots, recorded on September, 30 in 2011. A typical sunspot consists of a dark core, the umbra and a slightly brighter penumbra region. Usually they occur in groups, whereby consecutive groups have different magnetic polarities. The magnetic field lines break through the north polarity sunspot, make a loop over the solar surface and enter in the south polarity sunspot. Due to the strong magnetic field in the sunspots, these regions are often

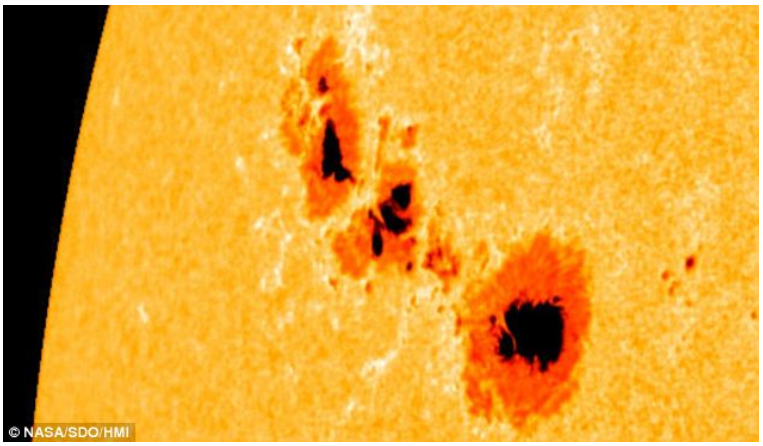

Figure 2.6: Sunspots observed on September, 30 in 2011 ©NASA/SDO/HMI

the origin of explosive energy releases within the photosphere, so-called solar flares.

2.1.2 Solar Flares

The first recorded observation of a solar flare was in 1859 by Richard Carrington who observed a white light flare above a sunspot. Flares are powerful explosions and occur in magnetic active regions where a rapid change in the direction of the local magnetic field occurs. The favoured mechanism to explain the sudden energy release in the order of 10^{25} J, is magnetic reconnection [Hanslmeier, 2002] - a physical process, which occurs in electrically conductive plasma. Considering a magnetic topology with anti-parallel field lines, which move towards the current sheet, it may happen that the magnetic field vanishes due to diffusion at a certain point [Baumjohann and Treumann, 2012]. As a result, the lines of magnetic force break and rejoin in a lower magnetic energy state (Fig. 2.7). Thereby, magnetic energy is converted into kinetic energy through acceleration or heating of charged particles [Yamada et al., 2010]. Since solar flares produce electromagnetic radiation in the short wavelengths of X-rays and ultraviolet (UV), it can be assumed that the temperatures are very high.

In general, we distinguish between three different phases during a solar flare. In the first phase, the pre-flare stage, we can observe an increase of soft X-rays. In the second phase, the so-called impulsive phase, the soft X-ray flux rises faster and hard X-rays and gamma rays are emitted quite impulsively. In the third phase, the gradual phase, the emission of hard X-rays and gamma rays decreases exponentially within minutes. Contrary to that, the soft X-rays are still rising to a later peak value.

Solar flares can be classified depending on the intensity of their emission in optical, radio or X-ray

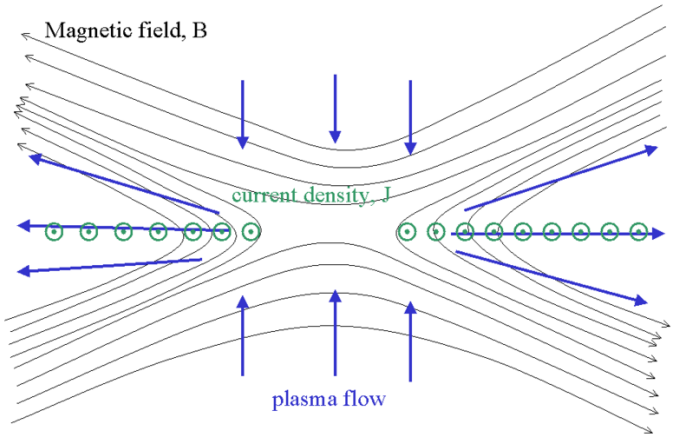

Figure 2.7: Illustration of magnetic reconnection ©SMesser, 2005.

radiation. In the following the different types of classification schemes are listed as stated in [Bhatnagar and Livingston, 2005]. In the optical classification (Tab. 2.1) the size of the flaring region in Hα is the crucial factor. Furthermore the flares are subdivided depending whether the flare was faint (F), normal (N) or bright (B). This means, a flare classified as 4B was bright and covered an

Importance Class	**Area A at disk 10^{-6} sol. hemisphere**	**Radio Flux at 5000 MHz in sfu**
S	A $<$ 200	5
1	200 $\leq$ A $<$ 500	30
2	500 $\leq$ A $<$ 1200	300
3	1200 $\leq$ A $<$ 2400	3000
4	A $\geq$ 2400	3000

Table 2.1: Optical and radio classification scheme of solar flares [Bhatnagar and Livingston, 2005].

area greater than 2400×10^{-6} of the disk. The radio classification (Tab. 2.1) is based on the flux intensity at the frequency of 5000 MHz, measured in solar flux units (1 sfu = 10^{-22} W m^{-2} Hz^{-1}). Based on the dynamic spectrum of radio bursts it is also possible to distinguish between confined flares (Type III, V) and eruptive flares (Type II, IV) [Hanslmeier, 2002]. The latter ones are associated with CMEs and have a long duration of more than one hour. On average about ten eruptive events occur per year. In contrast to that, there exist more than 1000 confined flares per year, which have a duration of less than one hour and are typically less intense.

Additionally, the size of the flare can also be linked to the peak intensity of the emission, extending from 10^{-8} to 10^{-4} W m^{-2}, as can be seen in Tab. 2.2. Since 1970 such a classification based

Importance class	**Peak-Flux in 1-8 $\AA$ [W m^{-2}]**
A	10^{-8} – 10^{-7}
B	10^{-7} – 10^{-6}
C	10^{-6} – 10^{-5}
M	10^{-5} – 10^{-4}
X	$\geq 10^{-4}$

Table 2.2: Soft X-ray classification scheme of solar flares.

on soft X-ray observations of the Sun in the 1-8 $\AA$ band is performed by using the Geostationary Operational Environmental Satellite (GOES) of NOAA. Thereby, large X-class flares have the most significant influence on the Earth's environment. Due to the intense and long-term radiation and the associated increase of heat and energy, an expansion of the upper Earth's atmosphere takes place.

To conclude this section, the left panel in Fig. 2.8 shows the extreme 3B/X28.0 solar flare, which occurred on November, 4 in 2003. Since the radiation travels at the speed of light, the impact in the Earth atmosphere can be observed approximately 8.28 minutes after the outburst. In the right panel of Fig. 2.8, the halo CME on October, 28 in 2003 recorded with SOHO/LASCO (Large Angle and Spectrometric Coronagraph) is shown. This event, also known as the "Halloween Event", caused major disturbances in the Earth environment and will be discussed in Sec. 2.1.4.

2.1.3 Coronal Mass Ejections

In 1973, significantly after the discovery of a solar flare by Carrington, Richard Tousey for the first time observed a CME using a space-based coronagraph. This instrument is a telescopic device which blocks the bright light from the Sun disk in order to observe nearby objects. Due to their diffuse structure, ill-defined edges and high velocities, CMEs are difficult to detect and to characterise [Lilensten, 2007].

In the past it has been proven that magnetic reconnection is also responsible for CMEs. During a CME up to 10^{12} kg of hot coronal plasma may be ejected into space. The charged particles can reach velocities of 2000 km s^{-1}, setting up a shock wave in front of them. Such a bow shock occurs when the velocity of the particles exceeds the speed of sound of the background material [Moldwin,

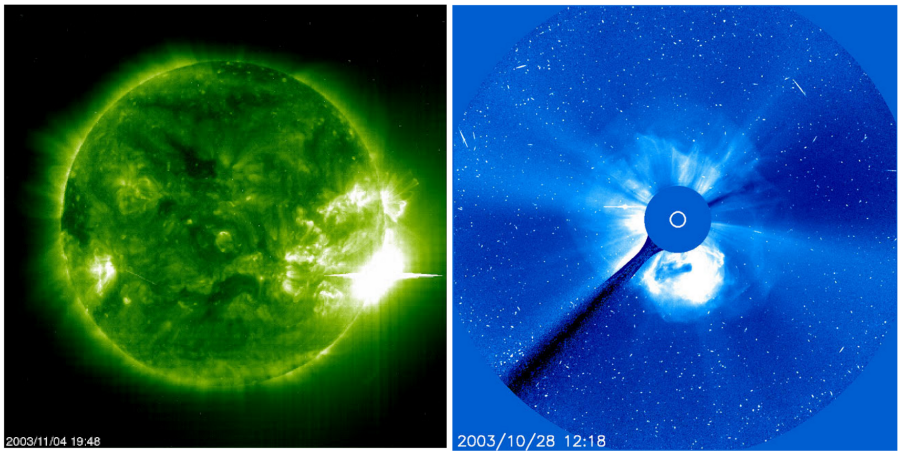

Figure 2.8: The left panel shows the extreme 3b/X28.0 solar flare, which occurred on Nov. 4 in 2003, recorded by SOHO/EIT (Extreme ultraviolet Imaging Telescope) at a wavelength of 19.5 nm. The right panel displays an image taken by the SOHO/LASCO (Large Angle and Spectrometric Coronagraph), which shows the huge halo CME, which was associated by the 4b/X17.2 flare on October 28, 2003. ©NASA/ESA

2008]. It is important to note that such a shock wave in the interplanetary space is a good particle accelerator. Thus, a CME pushes a large number of charged particles, which may excite a geomagnetic storm when they interact with the Earth magnetic field. Figure 2.9 illustrates the interaction between the IMF and the Earth magnetic field. Basically, the Earth's magnetic field becomes compressed on the dayside and is extended on the nightside, due to the IMF. If the IMF has a southward directed component (blue lines), it merges with the Earth magnetic field lines (green area). As a result the solar wind transports the merged field lines (red lines) across the polar cap towards the nightside where they will reconnect again [Baumjohann and Treumann, 2012]. Thus, charged particles may precipitate along the terrestrial field lines at the poles, causing significant ionisation and inducing the well-known aurora phenomena.

2.1.4 The Halloween Period

During this spectacular solar activity period in late October and early November 2003, several X-class flares, more than 40 CMEs, five solar energetic particle events, and two strong geomagnetic storms occurred [Krauss et al., 2012]. One of these extreme events was the X17.2 flare on October 28 in 2003. The strong flare started at 09:51 UT, had its maximum peak at 11:10 UT, and ended at 11:24 UT resulting in an exposure time of approximately 90 minutes[1]. It was associated with

[1] http://vso.nso.edu/cgi/catalogue

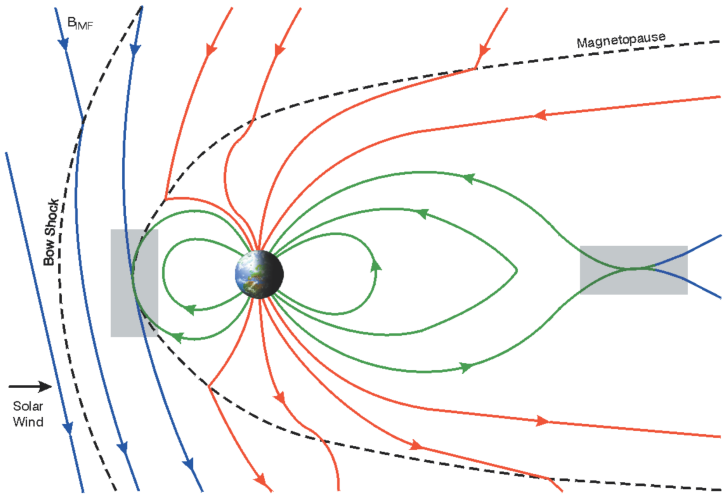

Figure 2.9: Interaction between the IMF and the Earth magnetic field [Committee on Solar and Space Physics, 2004].

a very fast halo CME, located in the active region AR 10486 at S16E08 (Fig. 2.8, right panel). Through the impressive velocity, which was larger than 2200 km s^{-1}, the CME was one of the fastest ever recorded. The United States Geological Survey Boulder magnetometer[2] measured a sudden impulse at the surface of 140 nT at 06:13 UT on October 29, equivalent to a transit time of merely 19 hours. The huge solar eruption caused electrical blackouts in southern Sweden and damaged several transformers in South Africa. The powerful EUV radiation of the solar flare and the subsequent strong particle emissions of relativistic protons and the gradual and impulsive electrons due to the CME had also immense consequences for the upper atmosphere of the Earth. In the present study, the focus is particularly on the impact of the X17.2 solar flare. A the closer look at the influences of the CME is beyond the scope of this thesis and will be treated in future analysis.

2.2 The Earth's Atmosphere

The atmosphere of the Earth with its various layers plays an important role in protecting mankind from dangerous electromagnetic and corpuscular radiation originating from the Sun. One often used distinction criteria for the different layers is the height depending temperature profile, which

[2] http://www.swpc.noaa.gov/rt_plots/bou_12h.html

is illustrated on the left side of Fig. 2.10. Worth mentioning are the three maxima and two minima of the temperature curve.

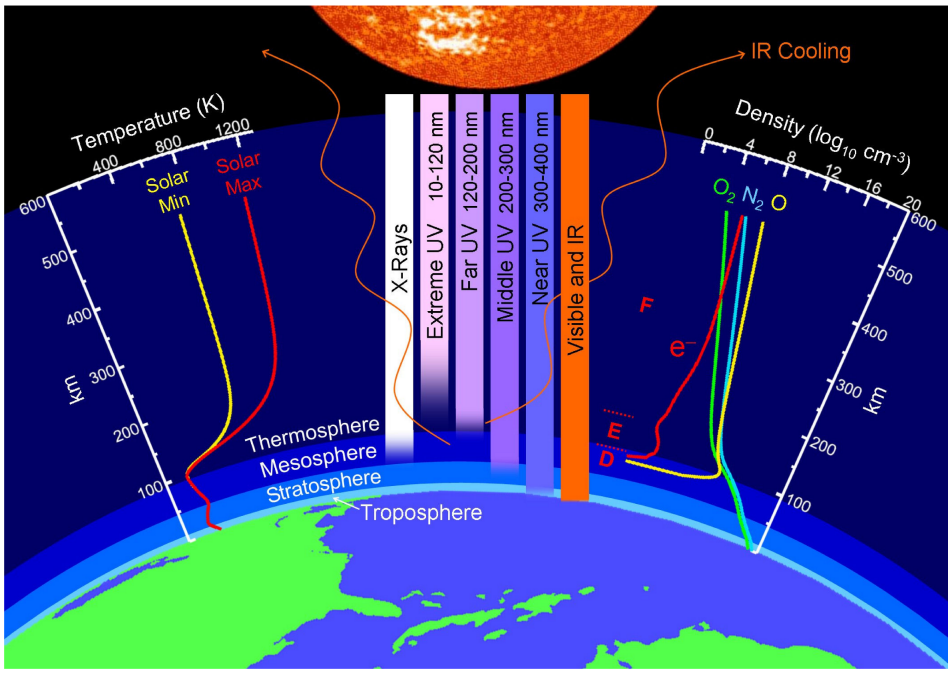

Figure 2.10: Profile of the Earth's atmosphere. Credit: John Emmert/NRL

The first maximum arises through the heating of the Earth's surface. Basically, the electromagnetic radiation from the Sun, in the wavelength of visible light (380–750 nm), passes through the Earth's atmosphere and heats the surface to a mean temperature of approximately 255 K. However, due to atmospheric counter-radiation, which is widely known as the greenhouse effect, the surface as well as the lower atmosphere gets additionally heated. This is because the re-emitted energy of the Earth's surface has a much higher wavelength ($\sim$10μm). As a result, this infrared radiation (IR) is absorbed by greenhouse gases (e.g. water vapour, carbon dioxide, methane or ozone) and re-radiated to the Earth. According to Wien's displacement law (Eq. 2.7) the induced additional heating by the IR radiation is in the order of about 33 K, resulting in a mean surface temperature of $\sim$ 288 K.

The layer which is located closest to the Earth's surface is the troposphere. It denotes the lowest part of the atmosphere, whereby the upper boundary strongly depends on the geographical latitude. In polar regions it has the merest expansion up to 7 km, whereas in tropical regions it reaches from the surface to roughly 20 km. The troposphere contains about 80% of the total atmosphere mass and 99% of the total water vapour content. The electromagnetic radiation emitted by the

Sun heats the lower atmosphere, the continental surface and the oceans unevenly, depending on the incident angle of the sunlight and the duration of the incoming radiation. Based on these temperature differences winds are generated [Moldwin, 2008]. Thus, it is the region where all weather relevant processes happen. Due to the reduced heating from the surface, the temperature is decreasing with increasing height. Beside the temperature, also the density and the atmospheric pressure decrease. In the tropopause, the upper boundary of the troposphere, the temperature reaches ∼220 K.

The next higher layer is known as the stratosphere and extends to approximately 50 km. Since the temperature in the transition region between the troposphere and the stratosphere is rather low, almost no water vapour is present. The stratosphere is of utmost importance for life on Earth. Within this layer UV in a wavelength range greater than 242 nm is absorbed by the ozone molecules [Proelss, 2001]. In this absorption process electromagnetic radiation is transformed to heat, hence the temperature is again rising. Till the beginning of the next layer, the mesosphere, the temperature increases to 270 K. In the mesosphere the temperature drops to a minimum value. This is because the absorption is rather low and the re-emitted radiation is quite effective due to the existing carbon monoxide [Proelss, 2001]. On average, the temperature is approximately between 120 and 160 K in the mesosphere.

In the following layer, the thermosphere, the temperature is increasing steadily. The layer starts at ∼90 km above the Earth's surface and does not have a clearly defined transition to the exosphere at approximately 500 km. The thermosphere comprises the biggest part of the atmosphere regarding the volume. However, it makes up less than one percent of the total mass of the complete atmosphere above 100 km. "The region is an externally-forced deterministic system, wherein instabilities are strongly suppressed due to the dominance of molecular diffusion" [Forbes, 2007]. Contrary to the lower part of the atmosphere, where we generally find molecular nitrogen (N_2) and oxygen (O_2), the thermosphere consists mainly of atomic oxygen (O) and in smaller parts of N_2 and helium (He) [Proelss, 2001]. In this region nearly the complete X-ray and EUV radiation ($\lambda \leq 242$ nm) is absorbed, thus the layer is strongly correlated with the level of solar activity. As a result of the absorption of X-ray and UV radiation, the temperatures may rise beyond 1500 K, implying an expansion of the complete layer. This is why the thermosphere does not have a clearly defined upper limit. Embedded in the thermosphere is the ionosphere. Ionisation occurs when an electron is detached from an atom or molecule by energetic particles or solar high-energy radiation. Depending on the height, the ionosphere can be divided into three main layers, namely the D-, E- and F-layer. An illustration of the layers combined with the electron profile is shown on the right side of Fig. 2.10 (red curve). The transition to the interplanetary space is called the exosphere. It

contains mainly hydrogen, and since collisions between atoms are rather rare, it is the only layer in which gas molecules may escape from the Earth's gravitational field.

As is generally known, the atmospheric density decreases exponentially with increasing height. The further away from the Earth's surface, the less weight is in the air column above. Thus, the air pressure exerted by the weight of the atmosphere, also decreases with increasing height. A relationship between the density, the pressure and the temperature can be established through the ideal gas law, which is defined as

$$\rho = \frac{p\ M}{R\ T}. \tag{2.8}$$

Here M indicates the molecular weight of the gas [kg mol^{-1}] and R the gas constant (R=8.3144 J K^{-1} mol^{-1}). An alternative notation of the ideal gas law, which is frequently used in the literature, is based on the particle density n and can be written as

$$p = n\ k\ T, \tag{2.9}$$

where k denotes the Boltzmann-constant. The vertical structure of the atmosphere is mainly governed by hydrostatic equilibrium, which implies that the pressure gradient force is in balance with the downward force from the gravity g. This relation is described by the hydrostatic equation

$$\frac{dp}{dh} = -\rho(h)g(h). \tag{2.10}$$

A combination of Eq. 2.8 and Eq. 2.10 yields

$$\frac{1}{p} \cdot \frac{dp}{dh} = -\frac{M(h)g(h)}{RT(h)}. \tag{2.11}$$

Based on a subsequent integration we obtain the barometric formula which indicates atmospheric pressure as a function of height

$$p(h) = p(h_0)\exp\left(-\int_{h_0}^{h} \frac{dz}{H(z)}\right) \quad \text{with} \quad \frac{1}{H(h)} = \frac{M(h)g(h)}{RT(h)}, \tag{2.12}$$

where H describes the pressure scale height. If we express Eq. 2.11 in terms of ρ, the density as a function of height can be written in a similar way:

$$\rho(h) = \rho(h_0)\exp\left(-\int_{h_0}^{h} \frac{dz}{H^*(z)}\right) \quad \text{with} \quad \frac{1}{H^*(h)} = \frac{1}{H(h)} + \frac{1}{T(h)}\frac{dT(h)}{dh}, \tag{2.13}$$

here H^* indicates the density scale height. Both scale heights are very important for the description of any atmosphere. They describe the vertical distance $(h-h_0)$ in which the pressure or the density changes by a factor of 1/e. This means, that if the Earth's atmosphere will be heated (e.g. the

radiation of a solar flare), it will cause an increase in the scale height and a corresponding expansion of the atmosphere. As a result, the atmosphere layer at a certain density level is lifted to a higher altitude.

2.3 Impacts on the Earth's Environment

Like weather in general, also space weather may have an impact on different aspects of our everyday's life. As already mentioned in Sec. 2.1.2, it may happen that due to the intense radiation of a solar flare and the associated heating and expansion of the thermosphere, high-frequency (HF) radio blackouts may occur. In HF communication the ionosphere is used to reflect the signal, which makes a long-range communication possible. This means that the HF radio communication depends on the ionosphere density and thus on the solar and geomagnetic activity level.
Solar storms may also have an impact on the Global Navigation Satellite System (GNSS). When the GNSS signal travels through the atmosphere, it experiences a significant delay due to the ionosphere which is a dispersive medium. Receivers with two or more frequencies can eliminate most of the influences by computing an ionosphere-free combination of frequencies. However, since the majority of navigation receivers today use only L1-signals, the influence of the ionosphere has to be modelled in order to improve the positioning. Since solar flares are phenomena with an almost instantaneous impact, the modelling becomes a quite challenging task [Krauss et al., 2011].
In addition to the satellite signals, also the satellites themselves are influenced by solar phenomena. Depending on the satellite's altitude, different aspects are important (Tab. 2.3). The main

Orbit Type	**Altitude [km]**	**Missions**
Low Earth Orbit (LEO)	200–2000	GRACE, GOCE, JASON 1,2, ISS
Medium Earth Orbit (MEO)	2000–35786	GPS, GALILEO, LAGEOS 1,2
Geosynchronous Orbit (GEO)	35786	EGNOS, GOES, Meteosat
High Earth Orbit (HEO)	>35786	Cluster II, Double Star, OGO
Lagrangian Point Orbit (LPO)	Lagrangian Point	ACE, SOHO

Table 2.3: Classification of satellite orbits depending on their altitude.

danger for satellites, orbiting in LPO and HEO is the permanent exposure to the high-energy radiation. This may cause surface charging, deep dielectric charging, or from UV radiation solar arrays degradation. At altitudes of LEOs, the atmospheric drag is by far the most dominant force acting on the S/C. Since it depends on the atmospheric density which highly varies with both time and space, its influence is difficult to model. When a solar flare or a CME strikes the Earth, it

will heat the thermosphere. This in turn leads to an expansion of the thermosphere and the S/C is slowed down due to the denser atmosphere.

But not only in space, also on the Earth's surface solar storms may have a tremendous impact on our daily life. As mentioned in Sec. 2.1.3, fast CMEs typically drive shock waves, which produce energetic particles and can lead to variations in the electric currents in the ionosphere and magnetosphere. Based on Faraday's law of induction, such currents can induce voltages and currents in long conductors like pipelines or electric power lines and may lead to an overload of electrical components [Moldwin, 2008]. For example, in March 1989 a huge solar storm caused serious damage to a power grid in Quebec, Canada. As a result, the energy supply in the entire province Quebec collapsed for nine hours. Furthermore a transformer at the Salem New Jersey Nuclear Plant GSU was permanently damaged due to the same solar storm (Fig. 2.11). Also during the above

Figure 2.11: Permanent damage to the Salem New Jersey Nuclear Plant GSU Transformer caused by a geomagnetic storm occurred on March 13, 1989. Photos courtesy of PSE&G. The picture was taken from `http://science.nasa.gov`.

described "Halloween Period" in 2003 several power grids were affected by the solar storm. This included 15 transformers in South Africa and a power grid in Malmö, Sweden, which experienced a 20 to 50 minutes electrical blackout and affected approximately 50000 customers [Marusek, 2007]. Considering the extensive consequences of such power outages, the importance of understanding space weather and the effect of solar activity on Earth becomes obvious.

Chapter 3

In-situ Measurements from the GRACE S/C

Since the beginning of the 21st century satellite missions were launched aiming to extend the knowledge of the detailed structure of the Earth's gravity field. In order to separate the gravity field signals from other accelerations and noise, modelling the non-gravitational forces acting on the S/C is of major importance. For this purpose the satellites are equipped with accelerometers, which additionally offer the possibility to investigate the atmospheric density and its temporal and spatial variation. At present there are two LEO satellite missions in orbit, which are equipped with such instruments: the twin-satellite mission GRACE and the very low orbiting mission Gravity Field and Steady-State Ocean Circulation Explorer (GOCE; Drinkwater et al. [2003]). In addition

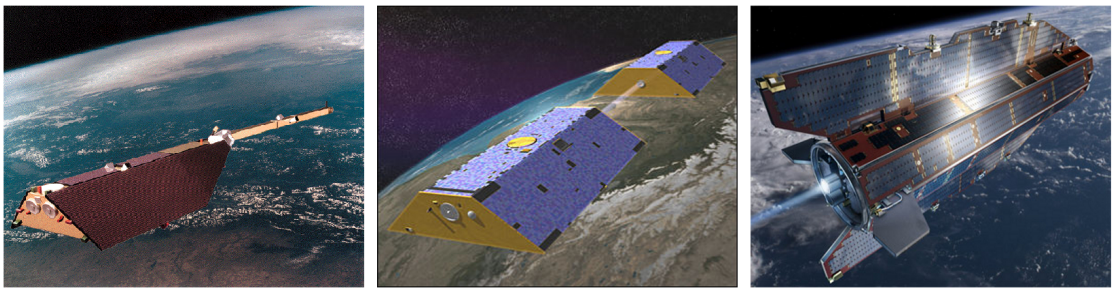

Figure 3.1: Overview of low Earth satellites (L-R: CHAMP, GRACE, GOCE) ©GFZ Potsdam, ESA.

to these two operational missions, ten years of data from the preceding Challenging Minisatellite Payload (CHAMP; Reigber et al. [2002]) mission are available. CHAMP a German satellite mission operated by the GeoForschungsZentrum Potsdam (GFZ) was launched in July 2000. Beside the

profiling of the Earth's atmosphere, it was dedicated to the global investigation of the Earth's gravity, magnetic and electric field. The left panel of Fig. 3.1 shows a picture from the satellite. The initial altitude of the S/C was 454 km, with a scheduled decay lifetime of about five years enclosing the solar maximum in 2001. Actually the satellite remained in orbit for more than ten years and provided important science data. On February 22 in 2010 CHAMP was turned in a scheduled manoeuvre and configured to fly with boom trailing. After 58277 revolutions around the Earth the satellite burned as planned in the atmosphere above the Sea of Okhotsk on September 19 in 2010.

In March 2002 a joint mission of the National Aeronautics and Space Administration (NASA) and the German Space Agency - GRACE (middle panel in Fig. 3.1) - was launched from the Plesetsk cosmodrome. The mission consists of two identical S/C which fly in a near polar orbit approximately 220 kilometres apart from each other. They use a microwave ranging system to accurately measure (within 10 μm) changes in the velocity and the inter-satellite distance. Thus, it is perfectly suited to monitor the temporal variations of the Earth's gravity field. Since gravity is related to mass and its transport in the Earth's system, also oceanography and geophysics benefit from the GRACE data. In Tab. 3.1 the key mission parameters are shown, followed by some science mission objectives [Kramer, 2002].

Mission Parameters	
Eccentricity	< 0.005
Inclination	89 deg
Revolution Period	94 min
Initial/Present Mass	487 kg / 468 kg
Cross-sectional Area	0.96 m^2
Initial/Present Altitude	505 km / 458 km

Table 3.1: GRACE mission parameters. The satellite mass and mean altitude are given for the mission start in 2002 and the present time (Sep. 1, 2012).

GRACE Science Objectives
Enable a better understanding of ocean surface currents and ocean heating transport
Measure changes in the sea-floor pressure
Study ocean mass changes
Measure the mass balance of ice sheets and glaciers
Measure changes in the continental hydrology and global water cycle

Table 3.2: Science objectives of the GRACE mission [Kramer, 2002]

Contrary to other satellite missions, the GRACE S/C act themselves as primary science instruments [NASA, 2006]. Orbit differences due to variations in the Earth's gravity field are visible in the form of changes in the distance between the two satellites. Thereby, the distance is estimated by means of K-band measurements of the microwave ranging system. Since the range also depends on non-gravitational forces, the S/C carries a SuperSTAR accelerometer (SSA). When determining atmospheric mass densities from these SSA measurements, the mission has general advantages compared to its predecessor CHAMP. Since the GRACE mission consist of two S/C, orbiting at close distance, both S/C experience nearly the same forces. This, offers the possibility to verify the results obtained from one satellite with the other. Another point is the simpler shape of the GRACE S/C compared to CHAMP, which is an advantage when estimating atmospheric mass densities.

In March 2009 one of the most challenging LEO missions was launched at the Plesetsk cosmodrome. After many years of preparations the first electrostatic gravity gradiometer was launched into space aboard the GOCE satellite (right panel in Fig. 3.1). With this instrument it is possible to provide a very accurate and detailed global model of the Earth's gravity field and geoid [ESA, 1999]. To accomplish this task, GOCE is orbiting at an extreme low altitude of approximately 255 km. At such an operational height the influence of the drag force has such a large impact that ion thrusters must be used to continuously compensate the drag force. Thus, information concerning the atmospheric density can only be derived from the analysis of the ion propulsion system. Since the present study focuses on the response of the Earth thermosphere from extreme solar storms, the GOCE mission is not as well suited as the other mentioned LEO missions. Due to the launch date in 2009, the satellite was so far operating mostly during periods of low solar activity. Because of the extension of the mission lifetime to autumn 2013, the S/C will now also be in space during the next solar maximum, which is expected in mid 2013. However, according to the latest predictions of the current solar cycle 24 it seems that the present cycle might be the smallest since more than 100 years. Thus, the probability of extreme solar flares, that can be used as solar proxies, is smaller.

3.1 Data Products from GRACE

In order to calculate atmospheric mass densities, it is not sufficient to solely use accelerometer measurements. It is also necessary to gather information concerning the position and velocity of

the satellite as well as general specifications like the actual satellite mass, the shape and miscellaneous surface properties of the S/C. In case of the GRACE mission, all kinds of data products are available through the Information System and Data Centre (ISDC) in Potsdam. The ISDC is a service portal, operated by the GFZ-Potsdam and providing geoscientific geodata to the community. The majority of the data are global geo-monitoring products from various projects (e.g. CHAMP, GRACE, GGOS, ICGEM). The products include satellite orbits, Earth's gravity field data as well as geomagnetic and atmospheric data for various fields of research.

In the present study Level-1B data products (L1B), that stem from preprocessed Level 1A and Level 0 data are used. Thus, the applied data are correctly time-tagged and the sampling rate is reduced from the high rate data of the previous levels [Case et al., 2010]. Additionally, erroneous measurements and outliers are already eliminated and data gaps are filled by interpolation.

In addition to these L1B data products also a macro-model of GRACE is used Bettadpur [2007].

Specific	**Area**	**Unit Normal (SRF)**			**Emiss.**	**Absorb.**
Panel	**m^2**	**x**	**y**	**z**	**(IR)**	**(Visible)**
Boom	0.046				0.62	0.34
Front	0.955	1.0	1.0	0.0	0.62	0.34
Rear	0.955	-1.0	0.0	0.0	0.62	0.34
Nadir	6.071	0.0	0.0	1.0	0.75	0.12
Zenith	2.167	0.0	0.0	-1.0	0.81	0.65
Starboard (outer)	3.155	0.0	0.767	-0.642	0.81	0.65
Starboard (inner)	0.228	0.0	-0.767	0.642	0.62	0.34
Port (outer)	3.155	0.0	-0.767	-0.642	0.81	0.65
Port (inner)	0.228	0.0	0.767	0.642	0.62	0.34

Table 3.3: Macro-model for the GRACE S/C [Bettadpur, 2007]. Unit normals are given in the science reference frame.

The model is an important element in the determination process and provides information concerning the properties of each individual satellite plate. This includes the size, the unit normal, the material as well as the emissivity and absorptivity/reflectivity coefficients for each panel of the satellite. The macro-model of the GRACE S/C is summarised in Tab. 3.3, and a simplified illustration of the leading satellite, including the orientation of the accelerometer frame (AF) and the science reference frame (SRF), is shown in Fig. 3.2.

The following is a list of the L1B data products which were mentioned above and are used in the course of the determination process

- GA-OG-1B-ACCDAT (acceleration data)

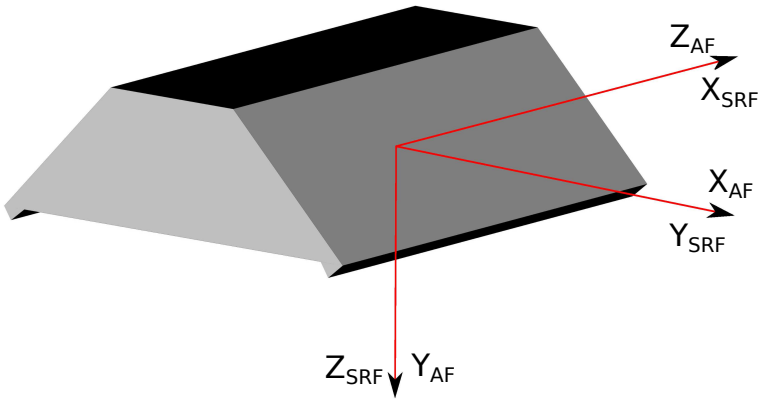

Figure 3.2: Scheme of the leading GRACE S/C, with the accelerometer reference frame (AF) and science reference frame (SRF). Both frames have their origins at the centre of mass of the satellite and are pointing towards the other GRACE satellite.

- GA-OG-1B-NAVSOL (orbit data)
- GA-OG-1B-MASDAT (mass data).

Acceleration and orbit data records are discussed in the next Sec. 3.1.1. The mass data simply include information on the satellite mass based on thruster usage observations. As mentioned above, the S/C had an initial weight of 487 kg, which is steadily decreasing due to the consumption of fuel.

3.1.1 GPS Navigation Data

Among numerous instruments the GRACE S/C also carries a Black-Jack GPS Receiver. It provides the precise relative and absolute timing for the data and of course the absolute position of the satellite [NASA, 2006]. Position and velocity is thereby given in the Conventional Terrestrial Reference System (CTS) with a sampling rate of one minute. In Fig. 3.3 a short excerpt of a typical navigation file is illustrated. The header record comprises various information like the producer agency, the institution, the file format, the satellite name and the time system which is used. The standard time system for L1B data products of GRACE is the GPS time (GPST). The GPST counting began on January 6 in 1980 when it was in agreement with the Universal Time System (UTC). Since then, GPST and UTC differ due to the fact that no leap seconds are introduced in GPST. For the GRACE mission the reference epoch is defined differently, namely T_0 = Jan. 1, 2000.

If different data products are used it must be ensured that all of them refer to the same spatial

```
PRODUCER AGENCY                : NASA
PRODUCER INSTITUTION           : JPL
FILE TYPE ipGNV1BF             : 5
FILE FORMAT 0=BINARY 1=ASCII   : 1
NUMBER OF HEADER RECORDS       : 25
SOFTWARE VERSION               : $Id: gni1a2gnv1b.c 1.10 05/13/06 03:00:12 l0t $
SOFTWARE LINK TIME             : @(#) 2007-01-03 19:38:46 glk  j2
REFERENCE DOCUMENTATION        : GRACE Level 1 Software Handbook
SATELLITE NAME                 : GRACE B
SENSOR NAME                    : GRACE B
TIME EPOCH (GPS TIME)          : 2000-01-01 12:00:00
TIME FIRST OBS(SEC PAST EPOCH): 346766340.000000 (2010-12-27 23:59:00.00)
TIME LAST OBS(SEC PAST EPOCH) : 346852860.000000 (2010-12-29 00:01:00.00)
NUMBER OF DATA RECORDS         : 1443
PRODUCT CREATE START TIME(UTC): 2011-01-10 22:04:49 by l0tol1
PRODUCT CREATE END TIME(UTC)   : 2011-01-10 22:04:49 by l0tol1
FILESIZE (BYTES)               : 366354
FILENAME                       : /GB-OG-1B-NAVSOL+JPL-G2-28_B_01.asc

INPUT FILE NAME                : GNI1A<-GNI1A_2010-12-27_B_01.dat
INPUT FILE TIME TAG (UTC)      : GNI1A<-2011-01-10 20:46:20 by l0tol1
INPUT FILE NAME                : GNI1A<-GNI1A_2010-12-28_B_01.dat
INPUT FILE TIME TAG (UTC)      : GNI1A<-2011-01-10 21:20:54 by l0tol1
INPUT FILE NAME                : GNI1A<-GNI1A_2010-12-29_B_01.dat
INPUT FILE TIME TAG (UTC)      : GNI1A<-2011-01-10 22:04:31 by l0tol1
END OF HEADER
346766340 B E 6191355.640783115 1292052.293373006 2584455.780598453
0.001970638464495948 0.002301783104293863 0.002854485420250567 2916.609690716956
282.802986682405 -7065.252932149931 2.409655418793632e-06 2.334870067402852e-06
2.565165438887413e-06  00000000
```

Figure 3.3: Example of the a Navigation Data File, including the header and two data record lines.

reference frame. However, since the acceleration measurements are given in the AF we have to transform the orbital data. In the first step, the orbital data must be transformed from the given CTS to the Conventional Inertial Reference System (CIS). This can be accomplished by applying several rotations, taking into account the corrections due to nutation and precession and considering sidereal time and polar motion. In the following section the individual correction terms are briefly discussed.

3.1.2 Transformation from CTS to CIS

The transformation from the CTS to the CIS requires four rotation matrices. Following Hoffmann-Wellenhof et al. [2001] a connection between the CIS and the CTS can be established by:

$$\mathbf{x_{CIS}} = M\ S\ N\ P\ \mathbf{x_{CTS}}. \tag{3.1}$$

The matrices M, S, N, and P denote the rotations due to polar motion, Earth rotation, nutation and precession. For the rotation from the Celestial Ephemeris Pole (CEP) to the orientation of the Conventional International Origin (CIO) the pole coordinates x_p and y_p are necessary to set up the matrix M (Eq. 3.2)

$$M = \begin{pmatrix} 1 & 0 & x_p \\ 0 & 1 & -y_p \\ -x_p & y_p & 1 \end{pmatrix}. \tag{3.2}$$

In the present study information concerning the Earth orientation parameters (EOP) are taken from the IERS Bulletin A. The rotations due to nutation and precession were implemented by using the official Fortran subroutines[1], which are in agreement with the IERS 2003 conventions [McCarthy and Petit, 2004] and thus with the GRACE processing standards [Bettadpur, 2007]. Therewith, the small periodic perturbations of the Earth's rotation axis, which originate from monthly and annual variations of the lunar and solar torque [Montenbruck and Gill, 2001], as well as the secular change in the orientation of the Earth's rotation axis and the equinox are considered.
Also the Greenwich Apparent Sidereal Time (GAST), which measures the hour angle of the true equinox, was estimated using Fortran routines from the IERS in order to set up the rotation matrix S

$$S = \begin{pmatrix} \cos \mathrm{GAST} & \sin \mathrm{GAST} & 0 \\ -\sin \mathrm{GAST} & \cos \mathrm{GAST} & 0 \\ 0 & 0 & 1 \end{pmatrix}. \tag{3.3}$$

Finally, since the CTS is a rotating reference frame the rotation of the axis has to be considered when transforming velocities from the CTS to CIS. Thus, an additional rotation matrix dU must be calculated. Following Montenbruck and Gill [2001] this additional term can be determined by

$$\frac{dU(t)}{dt} \approx M \; \frac{dS}{dt} \; N \; P. \tag{3.4}$$

Thereby, the time-dependent derivative of the rotation matrix due to sidereal time can be written as

$$\frac{dS(t)}{dt} = \omega_{\oplus} \begin{pmatrix} 0 & 1 & 0 \\ -1 & 0 & 0 \\ 0 & 0 & 0 \end{pmatrix} S, \tag{3.5}$$

where $\omega_{\oplus}$ indicates the Earth's angular velocity (IERS2003; $\omega_{\oplus} = 7.292115 \times 10^{-5}$rads$-1$).

3.1.3 Transformation from CIS to SRF

After transforming the coordinates and velocities to the CIS, another transformation into the SRF has to be performed. This can be accomplished by using quaternions. The theory of quaternions was first described by Sir W.R. Hamilton in 1843 [Hamilton, 1843] and applied to mechanics in three-dimensional space. Quaternions belong to the complex numbers and are 4-tupels, forming a non-commutative division ring [Sakulin, 2004]. The quaternion q can be split into a scalar part q_0 and a vector part $\mathbf{q}$:

$$\mathbf{q} = [q_0, \underline{q}], \underline{q} = (q_1, q_2, q_3) \tag{3.6}$$

$$\mathbf{q} = q_0 + \mathbf{i}q_1 + \mathbf{j}q_2 + \mathbf{k}q_3 \tag{3.7}$$

[1] http://tai.bipm.org/iers/conv2003/conv2003_c5.html

In the case of GRACE, the quaternions can be determined by using the inertial position and velocity vector [Wu et al., 2006]. In doing so the unit vectors of the SRF are calculated by

$$\mathbf{Z_i} = \mathbf{R_i}/|\mathbf{R_i}| \tag{3.8}$$

$$\mathbf{Y_i} = (\mathbf{Z_i} \times \mathbf{R_i})/|\mathbf{Z_i} \times \mathbf{R_i}| \tag{3.9}$$

$$\mathbf{X_i} = (\mathbf{Y_i} \times \mathbf{R_i})/|\mathbf{Y_i} \times \mathbf{R_i}| \tag{3.10}$$

where $\mathbf{X_i}$, $\mathbf{Y_i}$, $\mathbf{Z_i}$ denote the inertial position of the S/C in the respective axis. The inertial position and velocity is described by $\mathbf{R_i}$ and $\dot{\mathbf{R}}_\mathbf{i}$. As a result we gain the rotation matrix A,

$$A = [\mathbf{X_i}\ \mathbf{Y_i}\ \mathbf{Z_i}] \tag{3.11}$$

and finally the 4-tupel quaternions q_0, q_1, q_2, q_3:

$$q_0 = \sqrt{1 + A_{1,1} + A_{2,2} + A_{3,3}}/2 \tag{3.12}$$

$$q_1 = -(A_{2,3} - A_{3,2})/4q_0 \tag{3.13}$$

$$q_2 = -(A_{3,1} - A_{1,3})/4q_0 \tag{3.14}$$

$$q_3 = -(A_{1,2} - A_{2,1})/4q_0 \tag{3.15}$$

Based on these quaternions we are able to build the 3 × 3 rotation matrix R_{IS} to transform position and velocity from the CIS to the SRF.

$$R_{IS} = \begin{pmatrix} q_1^2 - q_2^2 - q_3^3 + q_0^2 & 2(q_1q_2 + q_3q_0) & 2(q_1q_3 - q_2q_0) \\ 2(q_1q_2 - q_3q_0) & -q_1^2 + q_2^2 - q_3^3 + q_0^2 & 2(q_2q_3 + q_1q_0) \\ 2(q_1q_3 + q_2q_0) & 2(q_2q_3 - q_1q_0) & -q_1^2 - q_2^2 + q_3^3 + q_0^2 \end{pmatrix} \tag{3.16}$$

$$\begin{pmatrix} x \\ y \\ z \end{pmatrix}_{SRF} = R_{IS}^T \cdot \begin{pmatrix} x \\ y \\ z \end{pmatrix}_{CIS} \tag{3.17}$$

3.1.4 Transformation from SRF to AF

In the last step we have to re-order the coordinate axis in order to get the orbit position and velocity in the desired AF. Since the systems of the two S/C of GRACE are oriented towards each other, an additional distinction has to be made.

GRACE-A:

$$\begin{pmatrix} x \\ y \\ z \end{pmatrix}_{AF} = \begin{pmatrix} y \\ z \\ x \end{pmatrix}_{SRF} \tag{3.18}$$

GRACE-B:

$$\begin{pmatrix} x \\ y \\ z \end{pmatrix}_{AF} = \begin{pmatrix} -y \\ z \\ -x \end{pmatrix}_{SRF} \tag{3.19}$$

However, it has to be noted that on December 9 in 2005, the order of the two satellites GRACE A and B has been changed. Before this specific date GRACE-A was leading GRACE-B, afterwards GRACE-A was the trailing satellite. Therefore the last two equations must be exchanged if the determination process falls after December 9, 2005.

3.1.5 Observations from the SuperSTAR-accelerometer

In order to measure non-gravitational forces acting on the satellite, each GRACE S/C carries a SSA. The instrument, displayed in Fig. 3.4, was built by the Office National d'Etudes et de Récherches Aerospatials (ONERA) and uses the principle of electrostatic levitation in order to suspend a proof-mass within an electrostatic cage [NASA, 2006]. The SSA is rigidly mounted

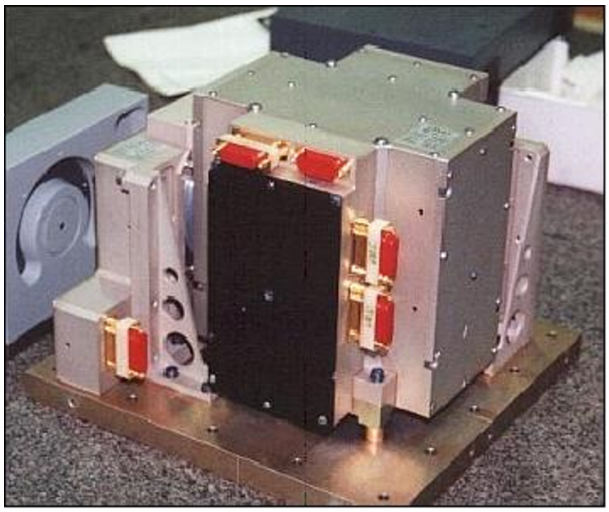

Figure 3.4: SuperSTAR accelerometer (image credit: ONERA/CNES)

at the centre of gravity of the satellite. The distance change between the proof-mass and the electrode cage, or rather the control force which is necessary to keep the proof-mass centred, is a measure of the non-gravitational accelerations acting on the satellite. This includes forces like air drag, solar radiation pressure and the optical and IR radiation emitted by the Earth. In Tab. 3.4 some specifications of the SSA are summarised. As in the case of the GPS Navigation data,

SuperSTAR Accelerometer Specifications	
Measurement Bandwidth	5×10^{-5} to 10^{-1} Hz
Measurement Range	$\pm 5 \times 10^{-5}$ m s^{-2}
Measurement Accuracy	1×10^{-10} m s^{-2}

Table 3.4: Specifications of the SSA aboard the GRACE satellites.

all observations of the SSA can be obtained from the ISDC. The L1B accelerometer records are available with a sampling rate of one second and are given in the GPST frame. The data product comprises linear and angular accelerations in all three axes. In the present study, only the linear accelerations in the along-track axis are analysed. Since the measurements are largely influenced by instrumental biases, a data calibration has to be performed. In this process, specific bias and scale parameters must be applied.

3.1.6 Calibration of the Raw Acceleration Data

In order to use the observations of the SSA in the further density determination, the raw acceleration measurements a_{raw} have to be calibrated by applying an instrument scale and bias. In this context an advantage of the twin-satellite mission shall be mentioned. Since the two GRACE S/C fly at a relatively close distance from each other, the measured non-gravitational forces must be nearly equivalent. Due to the fact that the calibration process is performed for each satellite separately, there is the possibility to verify the resulting calibrated accelerations a_{cal} against each other. Fig. 3.5 displays the uncalibrated measurements for both GRACE S/C on July 13 in 2003. The accelerations recorded by GRACE A and B look very similar, but their absolute values are different from each other. After the calibration procedure the accelerations of both S/C should deliver the same magnitudes, except for a different sign. This is due to the fact that the AFs of the satellites are oriented against each other.

In the present study two different sets of calibration parameters are used. The first set of parameters was determined following the recommendations by Bettadpur [2009], which are suitable for an initial estimates of scale and bias. The algorithm is based on precise orbit and gravity field

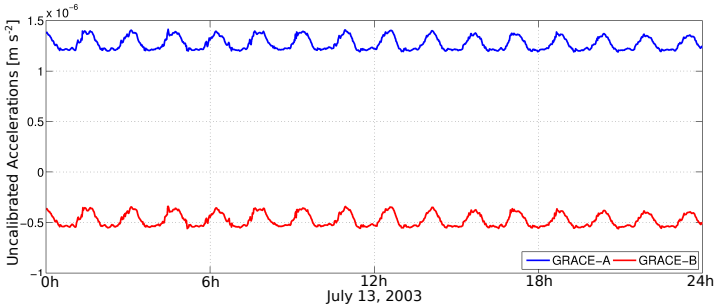

Figure 3.5: Uncalibrated, raw SSA acceleration measurements in along-track direction, observed by GRACE A and B on July 13 in 2003.

determinations between the launch in 2002 and March 31 in 2009. In principle the data calibration process can be written as:

$$a_{\text{cal}} = (a_{\text{raw}} + bias) \cdot scale. \tag{3.20}$$

For the instrument scale Bettadpur [2009] provides time-independent values, which are listed in Tab. 3.5. Contrary to the instrument scale, the bias can change over time. In order to model the

Direction (SRF)	GRACE-A	GRACE-B
X	0.9595	0.9465
Y	0.9797	0.9842
Z	0.9485	0.9303

Table 3.5: Time-independent scale parameters for each axes and each S/C recommended by Bettadpur [2009].

day-to-day variability, the parameter can be estimated by means of a quadratic function, in the form of

$$bias = c_0 + c_1(T_{\text{d}} - T_0) + c_2(T_{\text{d}} - T_0)^2. \tag{3.21}$$

Depending on whether the calculation date T_{d} is before or after March 7 in 2003, different sets of input parameters (c_0, c_1, c_2) must be applied (see Tab. 3.6 and 3.7).
The stated values result from a daily orbit determination and represent best fits for each of the two time spans. In the case T_{d} is prior to March 7, 2003, the reference time is defined as $T_0 = 52532$, otherwise $T_0 = 53736$.

The second set of calibration parameters was kindly provided by the Centre National d'Etudes Spatiales (CNES). The parameters were estimated by processing GPS and accelerometer data in

Direction (SRF)	c_0 [$\mu m\ s^{-2}$]	c_1 [$\mu m\ s^{-2}$]	c_2 [$\mu m\ s^{-2}$]
GRACE-A X	-1.106	2.233×10^{-4}	2.5×10^{-7}
GRACE-A Y	27.042	4.46×10^{-3}	1.1×10^{-6}
GRACE-A Z	-0.5486	-1.139×10^{-6}	1.7×10^{-7}
GRACE-B X	-0.5647	-7.788×10^{-5}	2.4×10^{-7}
GRACE-B Y	7.5101	7.495×10^{-3}	-9.6×10^{-6}
GRACE-B Z	-0.8602	1.399×10^{-4}	2.5×10^{-7}

Table 3.6: Input parameter for the calculation of the accelerometer bias (Eq. 3.21) before March 7, 2003.

Direction (SRF)	c_0 [$\mu m\ s^{-2}$]	c_1 [$\mu m\ s^{-2}$]	c_2 [$\mu m\ s^{-2}$]
GRACE-A X	-1.2095	-4.128×10^{-5}	9.7×10^{-9}
GRACE-A Y	29.3370	6.514×10^{-4}	-3.9×10^{-7}
GRACE-A Z	-0.5606	-2.352×10^{-6}	3.8×10^{-9}
GRACE-B X	-0.6049	-1.982×10^{-5}	3.5×10^{-9}
GRACE-B Y	10.6860	1.159×10^{-3}	-4.3×10^{-7}
GRACE-B Z	-0.7901	4.783×10^{-5}	-6.5×10^{-9}

Table 3.7: Input parameter for the calculation of the accelerometer bias (Eq. 3.21) after March 7, 2003.

daily arcs using the gravity field EIGEN-GL04C [Foerste et al., 2006] and the ocean tide model FES2004 [Lyard et al., 2006]. The data calibration formula can be written as

$$a_{\mathrm{cal}} = (a_{\mathrm{raw}} - bias) \cdot scale. \tag{3.22}$$

Again, the scale parameters are kept constant, and the bias offset is varying with time. Comparing the scale parameters from Tab. 3.5 and Tab. 3.8 slight differences can be seen. However, it can

Direction (SRF)	GRACE-A	GRACE-B
X	0.9640	0.9499
Y	0.9360	0.9112
Z	0.9120	0.8700

Table 3.8: Time-independent scale parameter for each axes and each S/C provided by CNES Bruinsma et al. [2007].

be stated that the effects on the calibrated accelerations are in the order of a few tenths of a

percentage and therefore negligible.

Bruinsma et al. [2007] mentioned, that during low solar activity the simultaneous estimation of bias and scale becomes inaccurate due to the absence of a clear signal and the resulting small magnitude of the accelerations. In Fig. 3.6 time series of bias offsets from both sources, between July 13, 2003 and January 1, 2010 are shown. A significant drift in both series is visible, which can

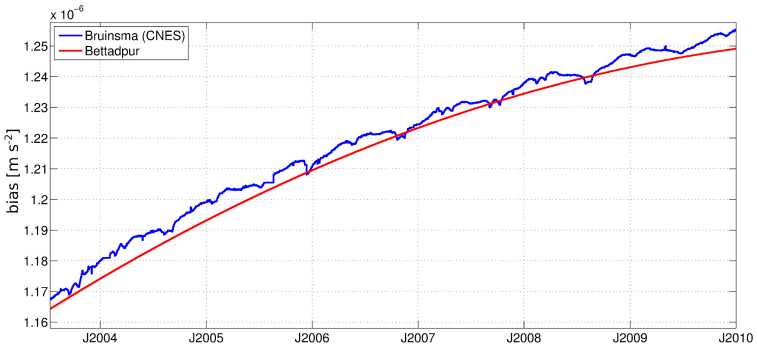

Figure 3.6: Comparison of bias values determined following the recommendations by Bettadpur [2009], and those estimated by CNES, for the GRACE A satellite.

be attributed to the ageing of the SSA [Bruinsma et al., 2007]. Additionally, it is recognisable that the quadratic term from Bettadpur slightly underestimates the results calculated by the CNES, thus yielding accelerations approximately 5% higher after the calibration procedure.

Since the parameter set based on the algorithm by Bettadpur [2009] is only a recommendation for an initial estimation the calibration parameters provided by CNES are used for the further density determination. Evaluating Eq. 3.22 yields calibrated acceleration measurements for both satellites. Finally, if we compare these resulting accelerations it can be seen from Fig. 3.7, that the requirement of equally sized accelerations for both S/C is now fulfilled. However, a closer look at the absolute acceleration values of both S/C (Fig. 3.8) reveals a slight offset between the two measurement series, in the order of approximately 29 seconds. Actually, this behaviour was expected. If the time-shift is converted into a range shift, by assuming a satellite velocity of $\sim$7.6 km s^{-1}, we obtain a distance of 220.4 km, which corresponds very well with the spatial separation of the two S/C. Furthermore, since both satellites are independently calibrated, such a behaviour can be used as an indicator for a proper calibration procedure.

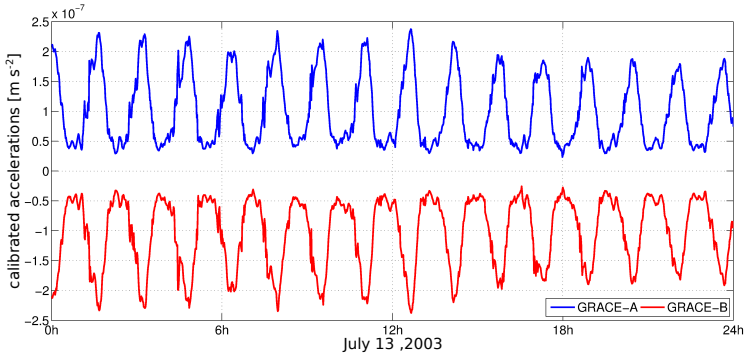

Figure 3.7: Calibrated accelerations for GRACE A and B on July, 13 in 2003.

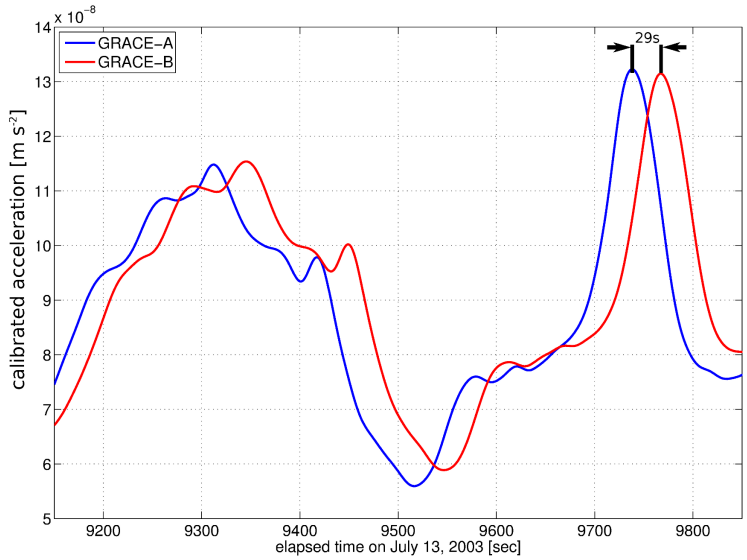

Figure 3.8: Comparison of the calibrated accelerations for GRACE A and B on July 13 in 2003. The offset between the two time series reflects the spatial separation of the two S/C in the order of 220.4 km.

3.2 Influence of Solar Radiation Pressure

As already mentioned in Sec. 3.1.5, the SSA measures all non-gravitational forces acting on the satellite. Thus the previously calibrated accelerations include the influences from the solar radiation pressure and the Earth radiation pressure in addition to the effect of the atmospheric drag force. Since we are solely interested in the variation due to the atmospheric drag, we have to reduce the accelerations by the disturbing forces originating from the other sources.

Table 3.9 summarises the various non-gravitational forces, acting on the S/C and their expected

magnitudes. Since the influence of the Earth radiation pressure is very small ($\sim$ 0.1%), it is

Non–gravitational force	**Magnitude [m s^{-2}]**
Atmospheric Drag (max.)	$\sim 2\times10^{-06}$
Earth Radiation Pressure (optical)	5×10^{-10}
Earth Radiation Pressure (IR)	2×10^{-10}
Solar Radiation Pressure	2×10^{-08}

Table 3.9: List of non-gravitational forces acting on a satellite at an altitude of approximately 500 km and the expected magnitudes [Sutton, 2008].

neglected in the current study. Thus, the calibrated accelerations have to be reduced by the influence of the solar radiation pressure, in order to achieve accelerations, which reflect the impact of the atmospheric drag force. Following [e.g., Sutton et al., 2007, Montenbruck and Gill, 2001] the acceleration due to solar radiation pressure a_{srp}, in the along-track axis can be computed by:

$$a_{\mathrm{srp}} = \sum_{i=1}^{9} \frac{SA_{\mathrm{i}} \cos(\phi_{\mathrm{inc,i}})}{mc} \left[2 \left(\frac{c_{\mathrm{rd,i}}}{3} + c_{\mathrm{rs,i}} \cos(\phi_{\mathrm{inc,i}}) \right) \mathbf{n}_{\mathrm{i}} + (1 + c_{\mathrm{rs,i}}) \mathbf{s}_{\mathrm{i}} \right]. \tag{3.23}$$

Here, S denotes the solar flux constant (1366 W/m^2), c the speed of light, and m the satellite mass. The specific plate area A_{i} as well as the coefficients for specular and diffuse reflectivity c_{rs} and c_{rd} are taken from the 9-plate macro-model of GRACE, described at the beginning of Sec. 3.1. In order to compute the angles between the plate normals and the direction towards the Sun, $\phi_{\mathrm{inc,i}}$, the position vector of the Sun relative to the S/C must be computed at every epoch. If we assume an unperturbed motion of the Earth around the Sun, the position of the Sun in the CTS can be calculated by using a simple series expansion. Following Montenbruck and Gill [2001], the Sun's ecliptic longitude $\lambda_{\odot}$ and distance $r_{\odot}$ can be written as

$$\lambda_{\odot} = \Omega + \omega + M + 6892'' sin(M) + 72'' sin(2M) \tag{3.24}$$

$$r_{\odot} = (149.619 - 2.499\ cos(M) - 0.021\ cos(2M)) \cdot 10^6 \mathrm{km}. \tag{3.25}$$

For the sum of the argument of the perigee ω and the right ascension of the ascending node Ω the proposed values by Montenbruck and Gill [2001] of $\Omega + \omega = 282.94°$ are used. The mean anomaly M can be computed by

$$M = 357.5256° + 35999.049° \cdot (JD - 2451545.0)/36525.0, \tag{3.26}$$

where JD indicates the actual time in Julian date. Consequently, the position of the Sun $\mathbf{r}_\odot$ in the CTS can be written as,

$$\mathbf{r}_\odot = \begin{pmatrix} 1 & 0 & 0 \\ 0 & cos(-\epsilon) & sin(-\epsilon) \\ 0 & -sin(-\epsilon) & cos(-\epsilon) \end{pmatrix} \begin{pmatrix} r_\odot\ cos\lambda_\odot\ cos\beta_\odot \\ r_\odot\ sin\lambda_\odot\ cos\beta_\odot \\ r_\odot\ sin\beta_\odot \end{pmatrix}. \tag{3.27}$$

Here, ϵ denotes the obliquity of the ecliptic at J2000.0 ($\epsilon = 84381.448''$, IERS2003). The ecliptic latitude $\beta_\odot$ vanishes within an accuracy range of 1'. After transforming the position of the Sun from the CTS to the desired AF (see Sec. 3.1.2- 3.1.4), we are able to build the vector $\mathbf{s}_\mathrm{i}$, denoting the i-th satellite-Sun unit vector. Since the i-th unit plate normal $\mathbf{n}_\mathrm{i}$ is known from the macro-model, it is now possible to calculate the desired angles $\phi_{\mathrm{inc,i}}$ between the plate normals and the satellite-Sun vector.

When summing up the individual contributions from each plate (Eq. 3.23), one has to keep in mind that some plates might be shaded by others and therefore may not contribute to the final solution. The same is true for the satellite-Sun eclipse, which means that the S/C is shadowed by the Earth. Thus, if the satellite is eclipsed, the influence of the solar radiation pressure must be completely omitted. Since the influence of the solar radiation pressure is rather small compared

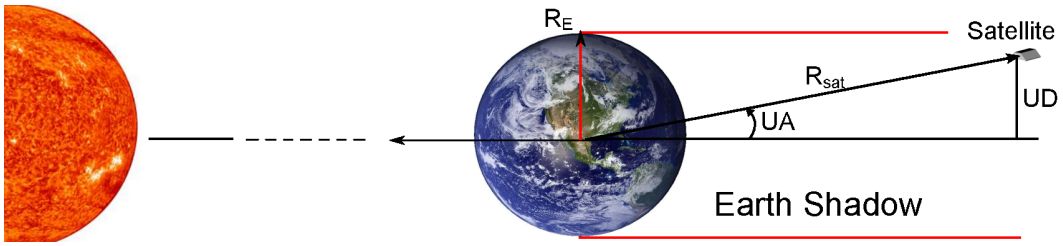

Figure 3.9: Illustration of a cylindrical shadow model, to take into account the satellite-Sun eclipse.

to the atmospheric drag force only a simple cylindrical shadow model was applied in the current study (Fig. 3.9). The illustration demonstrates that the satellite will be shadowed by the Earth if

1. the umbra distance (UD) is smaller than the Earth radius (R_E) and
2. the umbra angle (UA) is less than 90 degree.

It is thus necessary to determine the umbra parameters (UA, UD) in order to decide if the S/C is actually shadowed by the Earth or not. In the present study the calculations are performed following Miller[1]. If the position of both the Sun ($\mathbf{r}_\odot$) and the satellite ($\mathbf{r}_\mathrm{sat}$) is known, the umbra

[1] http://www.amsat.org/amsat/articles/g3ruh/112.html

angle can be determined by

$$\cos(UA) = -\frac{\mathbf{r}_{\odot}\ \mathbf{r}_{\mathrm{sat}}}{|R_{\odot}|\,|R_{\mathrm{sat}}|}, \tag{3.28}$$

where $R_{\odot}$ and R_{sat} denote the distance from the Earth centre to the Sun and the S/C, respectively. The umbra distance can afterwards be determined by

$$UD = R_{\mathrm{sat}} \cdot sin(UA). \tag{3.29}$$

If $UD \leq R_{\mathrm{E}}$ and $UA \leq 90°$ the satellite is shadowed by the Earth. In Fig. 3.10 the alternating situation when the satellite is in the Earth shadow or in sunlight is illustrated for a period of two days. Clearly visible are the ∼15 satellite revolutions per day. Since we now know exactly

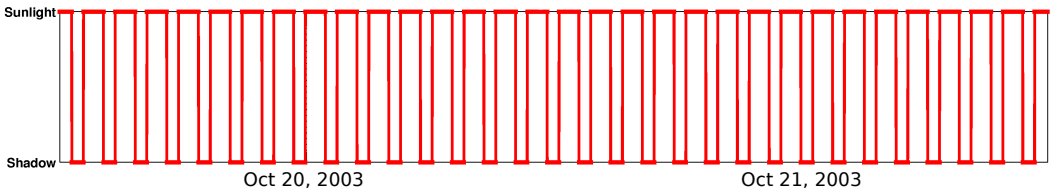

Figure 3.10: Visualisation of GRACE Sunlight illumination.

when the influence of the solar radiation on the S/C has to be considered we are able to calculate the resulting accelerations due to the solar radiation pressure. In the top panel of Fig. 3.11 the estimated accelerations are displayed for a period of one satellite revolution. In total, the acceleration due to the solar radiation pressure is in the order of $\pm 3.6 \times 10^{-8}\mathrm{ms}^{-2}$ during this period of time. It is remarkable that approximately five minutes before and after the eclipse a jump in the time series of the acceleration can be seen. If we take a look at the bottom panel in Fig. 3.11, this behaviour can be attributed to the algorithm that combines the impact on each individual plate. Shortly before and after the eclipse either the large nadir plate gets illuminated by the Sun, resulting in an increased solar radiation pressure.

3.3 Acceleration Characteristics

Now that the SSA accelerations have been properly calibrated and also reduced by the effects of the solar radiation pressure, some features shall be analysed, which will have an effect in the further course of the study.

From Sec. 2.2 we already know, that the total mass density of the Earth's atmosphere decreases with increasing altitude. Consequently, a satellite experiences a larger drag force the lower its altitude. In case of the GRACE S/C the difference in altitude due to orbit eccentricity is approximately

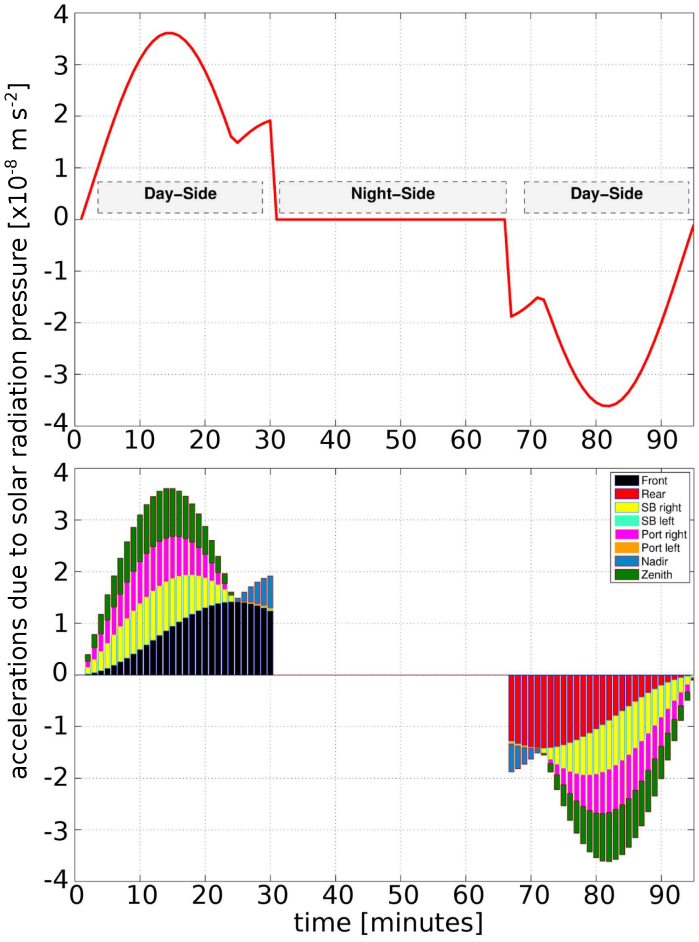

Figure 3.11: Acceleration due to solar radiation over the period of one revolution on July 13, 2003. In the top panel the total solar radiation pressure is shown, in the bottom panel the individual contribution of each plate is illustrated.

50 km. In Fig. 3.12 the satellite height is presented together with the accelerations recorded by the SSA for a period of three revolutions in 2008. As expected, a significant anti-correlation between the satellite altitude and the acceleration is apparent. The slight shift can be explained by the fact that not only the characteristics concerning the orbit height but also other effects are present in the data (e.g. latitude, local time). Thus, the correlations presented here must be perceived with caution.

Another fact is that the density, and thus the drag force acceleration, is higher at the dayside of the Earth than at the nightside due to higher temperatures. This can be proven if we compare the geographic longitude with the calibrated accelerations. As expected, Fig. 3.13 shows larger

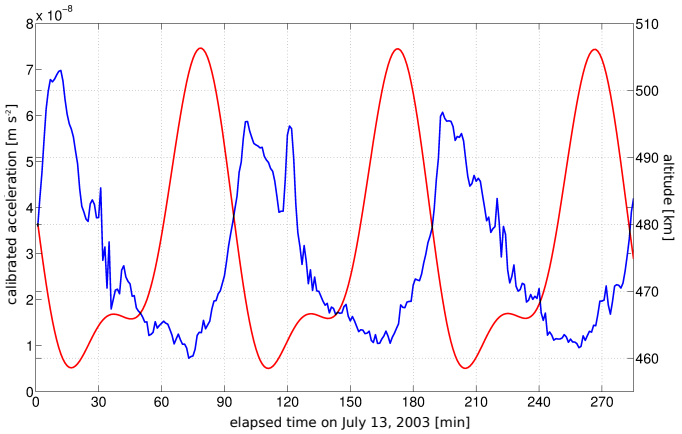

Figure 3.12: Calibrated GRACE accelerations (blue line) and orbit height (red line) on March 21, 2008.

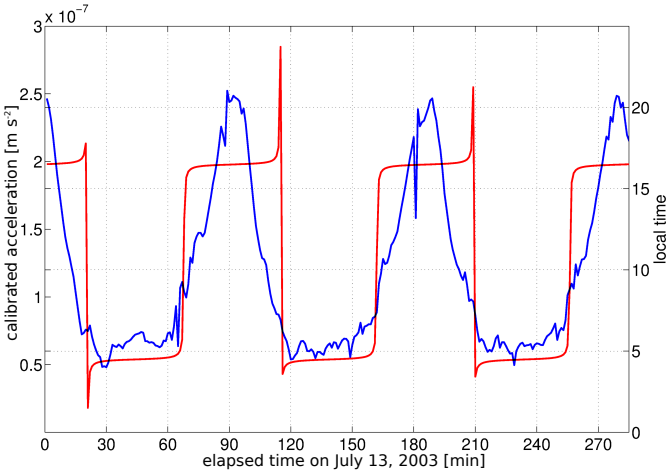

Figure 3.13: Calibrated GRACE accelerations (blue line) and the local time (red line) on March 21, 2004.

acceleration values on the dayside at ∼16:00 LT than on the nightside at ∼04:00 LT.

Chapter 4

Atmospheric Densities

In the present study atmospheric densities from accelerometer measurements aboard the GRACE S/C, which is orbiting at an altitude of approximately 500 km are determined. As we have seen in Sec. 2.2, this means that densities of the upper atmosphere, in particular the Earth's thermosphere are determined. Thereby, the relationship between the atmospheric density ρ and the satellite acceleration measurements a can be established by comparing the drag force F_{D} and Newton's second law:

$$\mathbf{F}_{\mathrm{D}} = \frac{1}{2}\rho\ \mathbf{v}^2\ C_{\mathrm{D}}\ A \quad \text{and} \quad \mathbf{F} = m\mathbf{a} \tag{4.1}$$

Thus, the density at position r and time t can be expressed as,

$$\rho(r,t) = \frac{a_{\mathrm{x}}}{-0.5\ C_{\mathrm{D}}\ \frac{A}{m}\ v_{\mathrm{x}}^2} \tag{4.2}$$

with
- a_{x} ... along track acceleration,
- v_{x} ... along track satellite velocity relative to the atmosphere,
- A ... effective cross section area,
- m ... satellite mass, and
- C_{D} ... satellite drag force coefficient.

Information concerning the actual satellite velocity v_x and the size of the S/C surface A, can be obtained from the navigation data of the S/C and the 9-plate macro-model, respectively (see Sec. 3). The only unknown parameter in Eq. 4.2 is the drag force coefficient C_{D}. This coefficient is a highly complex and variable quantity and defines the resistance of the S/C in the ambient atmosphere. In order to calculate this crucial factor, the interaction between the satellite surface and the ambient gas has to be considered. Since the beginning of the space age in the late 1950's and early 1960's, this coefficient was subject of numerous studies [Gustafson, 1958, Schamberg, 1959, Sentman, 1961, Cook, 1960, 1965].

4.1 The Physical Drag Force Coefficient

Before proceeding with a closer examination of the drag force coefficient C_{D}, an important distinction must be made. In astrodynamics the drag coefficient is often used as a fitting coefficient, in order to force an atmospheric model to agree with the tracking data when constructing a satellite orbit [Moe and Bowman, 2005]. Another possible interpretation is to treat the coefficient as a physical factor from which the computation of the force of the ambient air acting on the satellite in the along track axis is possible.
Without the knowledge of gas-surface interactions from satellites, Cook [1960] made a quite good and widely used estimate for the drag coefficient of $\mathrm{C_D} = 2.2$. Modern technologies provide a better understanding for determining this force coefficient. The formalism underlying this study is an analytical expression of Sentman's treatise of the drag coefficient elaborated from Moe and Moe [2005]. In order to calculate the coefficient some considerations and decisions must be made.

The first distinction concerns the aerodynamic flow regime. There exist three different categories, namely,

- the regime of continuum fluid mechanics,
- the transition regime and
- the regime of free molecular flow.

The three regimes differ in the governing physical phenomena. In a regime of continuum fluid, the intermolecular collisions are the most relevant activity. Contrary to that, the collisions between the atmospheric molecules among each other and the collision between the atmospheric molecules and the satellite surface are of equal importance, in the transition regime. In the case that the collision between the atmospheric molecules and the surface molecules of the S/C plays the most important role, a free molecular regime is present. The decision which regime is appropriate can be made by calculating the so-called Knudsen number K_{n}. This parameter is a measure for the density of the gas flow and can be written as

$$K_{\mathrm{n}} = \frac{\lambda}{L}, \tag{4.3}$$

where λ denotes the mean free path of molecules and L the size of the object. If the ratio between these two parameters is greater than 10, a free molecular flow can be assumed. A transition regime is present when K_{n} is between 0.01 and 10. If the Knudsen number is lower than 0.01 the flow is in the continuum regime.

In order to decide which regime shall be assumed in the case of GRACE, we have to specify the mean free path of molecules and the length of the satellite. In Fig. 4.1 a height profile of the mean free path of molecules is shown [Proelss, 2001].

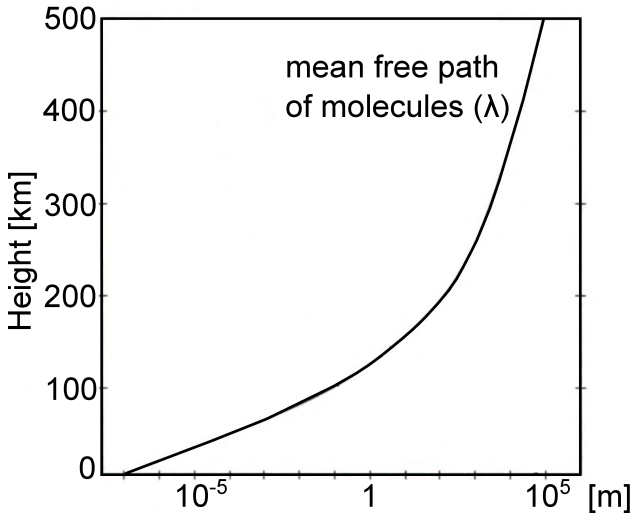

Figure 4.1: Height profile of the mean free path of molecules [Proelss, 2001].

Since GRACE is orbiting at an altitude between 450 and 500 km, λ can be assumed to be in the order of approximately 10^5 m. Furthermore, we know from the macro-model (Sec. 3.1) that the GRACE satellite has a length of 3.15 m. Thus, if we evaluate Eq. 4.3 the ratio is significantly larger than 10, which implies that the assumption of a free molecular flow regime is correct.
This means, that the collision between incident molecules and the surface molecules are much more frequent.
When a molecule hits the S/C surface it will bounce around in the space between the surface atoms and will leave the surface afterwards [Sentman, 1961]. In this context, we distinguish between a specular and a diffuse reflection. A reflection is specular when the angle of re-emitted gas particle is equal to the angle of the incident molecule. An illustration of this behaviour is shown at the left side of Fig. 4.2. In the case of a diffuse reflection, the angle of the re-emitted molecules is completely random and does not depend on the angle of the incident particles. However, in either case the velocity of the incident and the re-emitted molecules may not necessarily be the same. When a molecule hits the satellite, a momentum and energy transfer to the surface takes place. The speed of the re-emitted molecules depends on the amount of energy which is transferred to the S/C surface before re-emission [Storch, 2003]. The accommodation coefficient α is an indicator, how close the kinetic energy of the incoming molecules has adjusted to the thermal energy of the

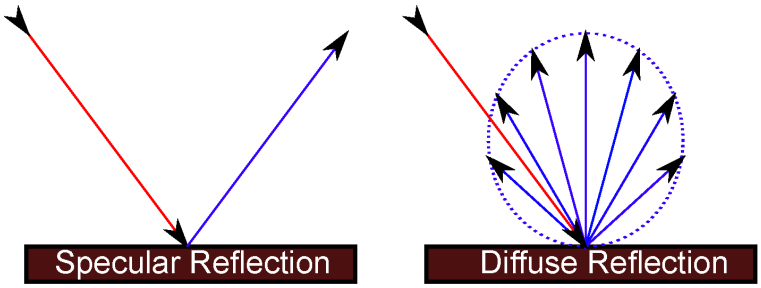

Figure 4.2: Two special types of reflections. In the left panel a specular reflection is illustrated. The angle of incidence is equal the angle of reflection. The right panel shows a diffuse reflection - in this case the angle of reflection is completely random.

surface before it is remitted [Moe and Moe, 2005]. This coefficient is defined as

$$\alpha = \frac{E_\mathrm{i} - E_\mathrm{r}}{E_\mathrm{i} - E_\mathrm{w}}, \tag{4.4}$$

where E_i denotes the kinetic energy of the incident gas molecules, E_r the kinetic energy of the re-emitted molecules. E_w is the energy the molecules would have if they re-emit at the temperature of the surface.

It has to be noted that the surface condition strongly depends on the altitude of the satellite, i.e. the number of oxygen atoms, which hit the surface and are then being absorbed.

Atomic oxygen binds strongly to many surfaces and changes their properties [Pardini et al., 2010]. At an altitude of 500 km the surface of a S/C gets contaminated by the absorbed atomic oxygen molecules [e.g., Hedin et al., 1973, Moe and Moe, 1969, 2005]. Thus, incident molecules loose a large part of their kinetic energy. In contrast to earlier studies, which assumed specular reflectivity above 200 km, recent studies (i.e. Moe and Bowman [2005]) showed that even at altitudes of 700 km it is better to assume a diffuse rather than a specular distribution. Fortunately, Sentman's model can still be justified since it is based on the assumption of a diffuse re-emission.

An almost complete diffuse re-emission means that E_r is nearly equal to E_w, yielding an accommodation coefficient α close to 1. For the present determination process the recommendation by Koppenwallner [2008] (α =0.90) are applied.

Based on the assumption of a free molecular flow, the re-emitted particles will not or very sparsely interact among each other. Thus, the velocity of particles follows a Maxwell-Boltzmann distribution in which the most probable velocity of the molecules, v_re, can then be calculated as

$$v_\mathrm{re} = v_\mathrm{inc}\sqrt{\frac{2}{3}\left[1 + \alpha\left(\frac{3RT_\mathrm{w}}{v_\mathrm{inc}^2} - 1\right)\right]}. \tag{4.5}$$

Here, R represents the universal gas constant (8.314 J K^{-1} mol^{-1}), v_{inc} the velocity of the incident particles which can be equated with the norm of the satellite velocity $\mathbf{v}$ and, T_w the surface temperature of the satellite panel which is assumed to be 273 K [Bruinsma and Forbes, 2003]. For several revolutions on July 13, 2003, the resulting velocity v_{re} combined with the satellite altitude is illustrated in Fig. 4.3. On one hand we can recognise that the velocity certainly anti-correlates

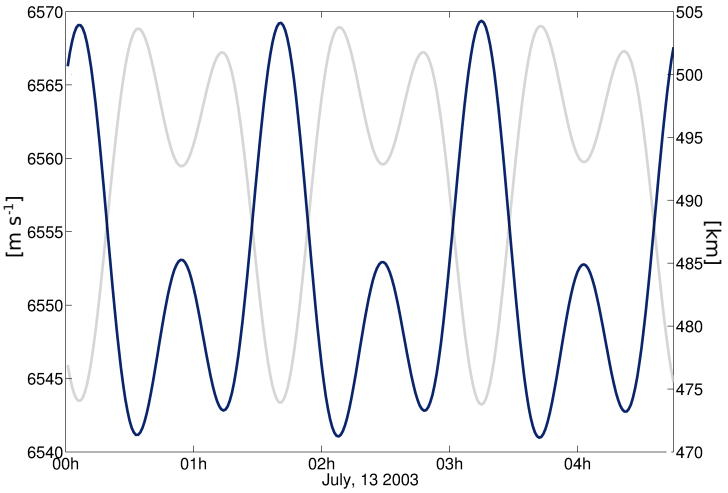

Figure 4.3: Plot of the most probable velocity v_{re} (blue line) and the satellite altitude (gray line) during three orbit revolutions on July 13, in 2003.

with the altitude of the S/C. On the other hand we see that the emitted particles have a lower velocity than the incident gas molecules (v_{inc} ~7600 m s^{-1}), due to the energy transfer.

Another implication of the free-molecule regime is that it does not disturb the flow. Thus, it is permitted to split the complex shape of the satellite into simple flat plates and to sum up the contribution from each of those [Sentman, 1961].
In Sentman's formalism the effect of random thermal motion of the neutral atmosphere molecules is also taken into account, which means that satellite panels that are nearly parallel to the flow will have a significant contribution to the determination process of the force coefficient.

When dealing with the drag force coefficient, we often solely consider the force, acting in the same direction as the incident gas flow v_{inc}. However, there also exists the so-called lift force, which acts perpendicularly to v_{inc} in the plane spanned by the plate normal $\mathbf{n}_{plate}$ and the drag direction $\mathbf{u}_{drag}$ (Fig. 4.4). Hence, the actual force coefficient must be split into two parts - the drag

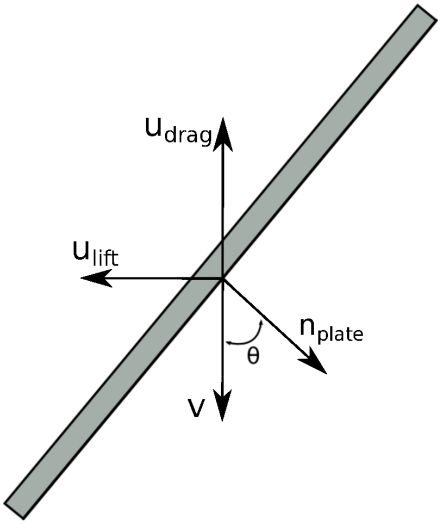

Figure 4.4: Relation of the incident gas flow (i.e. negative satellite velocity $\mathbf{v}$), the plate normal ($\mathbf{n}_\mathrm{i}$), and the drag ($\mathbf{u}_\mathrm{drag}$) and lift ($\mathbf{u}_\mathrm{lift}$) unit vectors.

coefficient C_D and the lift force coefficient C_L. Moe and Moe [2005] defined these coefficients as

$$C_{\mathrm{D,i}} = \frac{A_\mathrm{i}}{A_{\mathrm{ref,i}}}\left[\frac{P_\mathrm{i}}{\sqrt{\pi}} + \gamma_\mathrm{i} Q Z_\mathrm{i} + \frac{\gamma_\mathrm{i} v_\mathrm{re}}{2 v_\mathrm{inc}}(\gamma_\mathrm{i}\sqrt{\pi} Z_\mathrm{i} + P_\mathrm{i})\right] \tag{4.6}$$

and

$$C_{\mathrm{L,i}} = \frac{A_\mathrm{i}}{A_{\mathrm{ref,i}}}\left[l_\mathrm{i} G Z_\mathrm{i} + \frac{l_\mathrm{i} v_\mathrm{re}}{2 v_\mathrm{inc}}(\gamma_\mathrm{i}\sqrt{\pi} Z_\mathrm{i} + P_\mathrm{i})\right], \tag{4.7}$$

where θ denotes the angle between the incident gas particles and the specific plate normal, and γ_i and l_i are abbreviations for $\cos(\theta)$ and $\sin(\theta)$ of that angle. The ratio between the true and the projected plate area is indicated as $A_\mathrm{i}/A_{\mathrm{ref,i}}$. The subscript i indicates that the calculations are performed for each individual satellite panel separately.

The auxiliary quantities G, P, Q and Z are functions of γ_i and the molecular speed ratio s and can be written as

$$P = \frac{e^{-{\gamma_\mathrm{i}}^2 s^2}}{s}, \quad Q = 1 + \frac{1}{2s^2}, \quad G = \frac{1}{2s^2}, \quad Z_\mathrm{i} = 1 + erf(\gamma_i s) \tag{4.8}$$

with

$$erf(x) = \frac{2}{\sqrt{\pi}} \int_0^x e^{-y^2} dy \tag{4.9}$$

The molecular speed ratio s itself is defined as the ratio of the velocity of incident gas flow v_inc and the most probable random speed of the ambient atmosphere molecules v_M.

$$s = \frac{v_\mathrm{inc}}{v_\mathrm{m}} \tag{4.10}$$

Following Kurzweil et al. [2009], v_{m}, the speed at which the Maxwell distribution function has its maximum, is defined as

$$v_{\mathrm{m}} = \sqrt{\frac{2RT_{\mathrm{A}}}{M}}. \tag{4.11}$$

Introducing Eq. 4.11 into Eq. 4.10 gives

$$s = \frac{v_{\mathrm{inc}}}{\sqrt{\frac{2RT_{\mathrm{A}}}{M}}}, \tag{4.12}$$

with:

T_{A}	temperature of the ambient atmosphere [K]
R	universal gas constant:= 8.3144 J kg^{-1} K^{-1}
M	molar mass [kg mol^{-1}]

To evaluate Eq. 4.10 the temperature of the ambient atmosphere T_{A} and the molar mass M of the atmosphere are needed. For the present study, the chemical composition of the atmosphere was obtained by evaluating the empirical thermosphere model MSISE-00. For an average altitude of 500 km the model comprises: 90% oxygen (O), 6% helium (He), 2% nitrogen (N) and 2% molecular nitrogen (N2) yielding a molar mass of M=15.5 kg mol^{-1}. Values for T_{A} were calculated by using the empirical thermosphere model JB08. In Fig. 4.5 the resulting molecular speed ratio is illustrated for the investigation period (2003–2010).

The positive trend can be explained by the fact that the temperature of the ambient atmosphere is

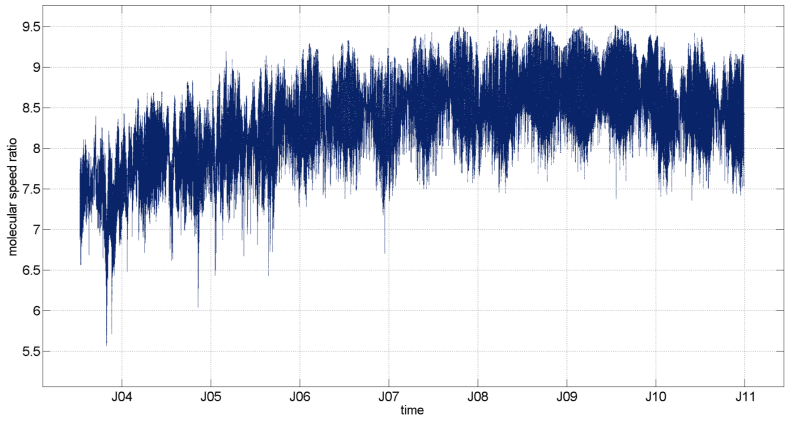

Figure 4.5: Molecular speed ratio for the period July 13, 2003 to December 28, 2010, determined at the altitude of GRACE. The temperature of the ambient atmosphere is taken from the JB08 model, the chemical composition of the atmosphere from the MSISE-00.

decreasing during low solar activity, and since the molecular speed ratio depends on this quantity,

it also decreases over the same period of time.

Still unknown in Eq. 4.6 and 4.7 is the angle γ_i. Thereby two aspects have to be considered: firstly, the influence of the co-rotating Earth atmosphere, and secondly the impact of horizontal winds. Each of them has a certain impact on this drift angle, hence the upcoming chapter will give a closer description concerning this issue.

4.1.1 Variation due to Co-Rotating Earth's Atmosphere

Due to the co-rotating Earth atmosphere, the velocity of the satellite experiences an impact in the cross-track direction. Depending whether the satellite is on an ascending or descending orbit, the deviation can be positive or negative. By using the Earth's angular velocity vector ($\omega_\oplus = 7.292115 \times 10^{-5}\ rad\ s^{-1}$; IERS2003), the wind speed due to the co-rotating Earth's atmosphere $\mathbf{v}_E$ can be determined by

$$\mathbf{v}_E = R_{IS}(\omega_\oplus \times \mathbf{X}_{sat}) \tag{4.13}$$

where R_{IS} denotes the rotation matrix, rotating from the CIS to the SRF of the satellite (see Sec. 3.1.3). $\mathbf{X}_{sat}$ indicates the actual satellite position in the CIS. For the GRACE S/C the calculation of the drift angle due to the co-rotating Earth atmosphere yield a value in the range of approximately ±3.76 degree. The maximal wind velocity occurs at the equator and is in the order of about ±500 m s^{-1}.

4.1.2 Impact of Horizontal Winds

Beside the influence of the co-rotating Earth's atmosphere also horizontal winds, which act relative to the previous effect must be taken into account. For the present drag determination procedure the horizontal wind model HWM07 is included in order to consider this effect. This empirical model provides a representation of the horizontal wind fields of the Earth's atmosphere up to 500 km [Drob et al., 2008]. Basically, it is an extension of the preceding HWM87, HWM90 and HWM93 models. In order to reproduce storm induced thermospheric winds the HWM07 includes the disturbance wind model DWM07 (Emmert et al. [2008]) that depends on the magnetic latitude, the local time and the 3-h K_p geomagnetic activity index.

To evaluate the HWM07, information on the actual time and the geographical position (ϕ, λ, h) are required. The geomagnetic activity is included via the a_p index which is a derivative of the K_p index.

For the development of this sophisticated model a huge number of observations from 35 different instruments covering a period of 50 years were included. A summary of the observational database

is shown in Fig. 4.6.

Table 1. HWM07 Observational Database Summary

Instrument	Location	Height (km)	Years	Local Time	Days	Data Points	Reference
			Satellite				
AE-E NATE[a]	±18.0°N	220–400	1975–1979	both	799	200,500	*Spencer et al.* [1973]
DE 2 WATS[b]	±89.0°N	200–600	1981–1983	both	536	391,500	*Spencer et al.* [1981]
DE 2 FPI[c]	±89.0°N	250	1981–1983	both	308	47,600	*Hays et al.* [1981]
UARS HRDI	±72.0°N	50–115	1993–1994	day	834	30,100,000	*Hays et al.* [1993]
UARS WINDII 5577 Å	±72.0°N	90–300	1991–1996	day	949	24,672,000	*Shepherd et al.* [1993]
UARS WINDII 6300 Å	±42.0°N	200–300	1991–1996	night	243	2,237,942	*Shepherd et al.* [1993]
			Sounding Rocket				
Falling Sphere	8°S–60°N	8–98	1969–1991	both	1,186	96,205	*Schmidlin et al.* [1985]
Rocketsonde	38°S–77°N	2–90	1969–1991	both	5,082	843,000	*Schmidlin et al.* [1986]
TMA	31°S–70°N	59–277	1956–1998	both	276	92,792	*Larsen* [2002]
			Fabry-Perot Interferometer				
Arecibo	18.4°N, 66.8°W	250	1980–1999	night	473	14,198	*Burnside and Tepley* [1989]
Arequipa	16.2°S, 71.4°W	250	1983–2001	night	1048	32,238	*Meriwether et al.* [1986]
Arrival Heights	77.8°S, 116.7°E	250	2002–2005	night	535	54,214	*Hernandez et al.* [1991]
Halley Bay	75.5°S, 26.6°W	250	1988–1998	night	799	82,614	*Crickmore et al.* [1991]
Millstone Hill	42.6°N, 71.5°W	250	1989–2002	night	1,770	68,333	*Sipler et al.* [1982]
Mount John	44.0°S, 170.4°E	89, 96, 250	1991–1996	night	560	2,660	*Hernandez et al.* [1991]
Søndrestrøm	67.0°N, 51.0°W	250	1984–2004	night	1,223	69,734	*Killeen et al.* [1995]
South Pole[d]	90.0°S	86, 250	1989–1999	night	1,091	163,044	*Hernandez et al.* [1991]
Svalbard[e]	78.2°N, 15.6°E	250	1980–1983	night	44	7,472	*Smith and Sweeny* [1980]
Thule	76.5°N, 68.4°W	250	1987–1989	night	172	21,500	*Killeen et al.* [1995]
Resolute Bay	74.7°N, 94.9°E	250	2003–2005	night	166	5,299	*Wu et al.* [2004]
Watson Lake	60.1°N, 128.6°W	250	1991–1992	night	135	28,000	*Niciejewski et al.* [1996]
			Incoherent Scatter Radar[c]				
Arecibo	18.3°N, 66.8°W	100–170	1974–1987	day	149	30,600	*Harper* [1977]
Chatanika	65.1°N, 147.4°W	90–130	1976–1982	day	97	38,721	*Johnson et al.* [1987]
European Incoherent Scatter	69.6°N, 19.2°E	100–120	1985–1987	day	29	2,900	*Williams and Virdi* [1989]
Millstone Hill	42.6°N, 71.5°W	120–400	1983–1987	both	142	23,536	*Salah and Holt* [1974]
Søndrestrøm	67.0°N, 50.9°W	150–400	1983–1987	both	146	19,600	*Wickwar et al.* [1984]
St. Santin[f]	44.6°N, 2.2°E	90–165	1973–1985	day	256	18,382	*Amayenc* [1974]
			Medium-Frequency Radar[g]				
Adelaide	34.5°S, 138.5°E	60–98	2001–2004	both	834	481,634	*Vincent and Lesicar*, 1991
Bribe Island	28.0°S, 153.0°W	60–98	1995	both	280	184,176	*Reid* [1987]
Davis	68.6°S, 78.0°E	50–100	2001–2004	both	730	526,160	*Vincent and Lesicar* [1991]
Poker Flat	65.1°N, 147.5°W	44–108	1979–1985	both	1857	2,746,684	*Murayama et al.* [2000]
Wakkanai	45.4°N, 141.8°E	50–108	1998–2003	both	1538	1,874,672	*Murayama et al.* [2000]
Yamagawa	31.2°N, 130.6°E	60–98	1998–2003	both	1593	1,040,042	*Murayama et al.* [2000]
			Wind and Temperature Lidar				
Fort Collins	40.6°N, 105.1°W	75–115	2002–2002	both	244	93,288	*She et al.* [2004]
			Numerical Weather Prediction Analysis[h]				
NOAA GFS Analysis	Global	0–35	2002–2007	both	1520	–	*Kalnay et al.* [1990]
NASA GEOS4 Analysis	Global	0–55	2002–2007	both	1520	–	*Bloom et al.* [2005]

[a]Cross-track component only.
[b]Zonal component only.
[c]Meridional component only.
[d]Withheld for validation purposes.
[e]From original *Hedin et al.* [1991] database.
[f]Magnetic meridian component only.
[g]Only data below 96 km used.
[h]Greater than 7,257,600 points per day.

Figure 4.6: List of datasets, which were used for the development of the HWM07 model [Drob et al., 2008].

As output parameters the model provides zonal and meridional winds in a North-East-Up (NEU) horizontal coordinate system. However, the density and drag calculations refer to the instrumental frame of the S/C. Thus it is necessary to transform the wind speeds of the HWM07 from the NEU frame ($\mathbf{v}_{\mathrm{HS}}$) to the AF. Knowing the geographical latitude ϕ and longitude λ, the velocities are in the first step transformed to the CTS ($\mathbf{v}_{\mathrm{CTS}}$) using the rotation matrix E

$$E = \begin{pmatrix} -\sin\lambda & -\sin\phi\cos\lambda & \cos\phi\cos\lambda \\ \cos\lambda & -\sin\phi\sin\lambda & \cos\phi\sin\lambda \\ 0 & \cos\phi & \sin\phi \end{pmatrix}. \tag{4.14}$$

$$\mathbf{v}_{\mathrm{CTS}} = E\ \mathbf{v}_{\mathrm{HS}}. \tag{4.15}$$

Afterwards, the transformations mentioned in (Sec. 3.1.1) can be applied. In doing so, we receive wind velocities in along-track, cross-track and nadir direction. To determine the impact on the drift angle, the wind in the cross-track axis is of major importance. In Fig. 4.7 this wind speed is illustrated. Beside of the visible seasonal variations of the wind speed in the cross-track

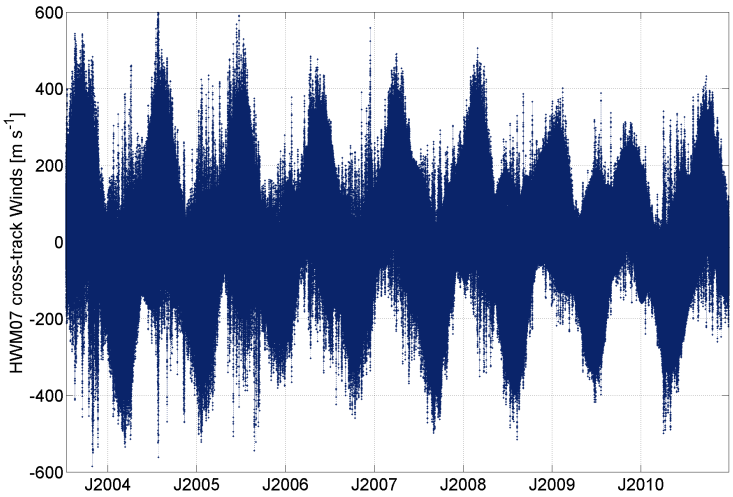

Figure 4.7: Cross-track wind speeds at the GRACE satellite location during July 13, 2003 and December 28, 2010. Values are converted from the HWM07 model.

direction, a decrease of the velocity amplitude with time is observable, which can be attributed to the low solar activity during the end of solar cycle 23.

Another interesting features can be observed by plotting the cross-track wind speeds in a latitude vs. time plot. Figure 4.8 illustrates such a plot during the Halloween period in 2003. Eye-catching are the changes in the wind direction between |90–45| degree, at the time when the CME shock wave stroke the Earth's atmosphere on the morning of October 29. A possible reason for this behaviour is an expansion and contraction of the auroral oval during the period of the disturbances [Rees, 2008]. In order to verify this, measurements of the Earth's magnetic field from the WIND[1] satellite during the same period of time are analysed. In Fig. 4.9 the magnetic field measurements in B_x direction (Earth–Sun) are illustrated, for a short period around 9h12min on October 29. Additionally, wind speed and the geographical latitude are included in the plot. As expected, a significant peak is visible in both time-series at 9h12min (ϕ= |90–45|). Beside this

[1] Comprehensive Solar Wind Laboratory for Long-Term Solar Wind Measurements; http://wind.nasa.gov

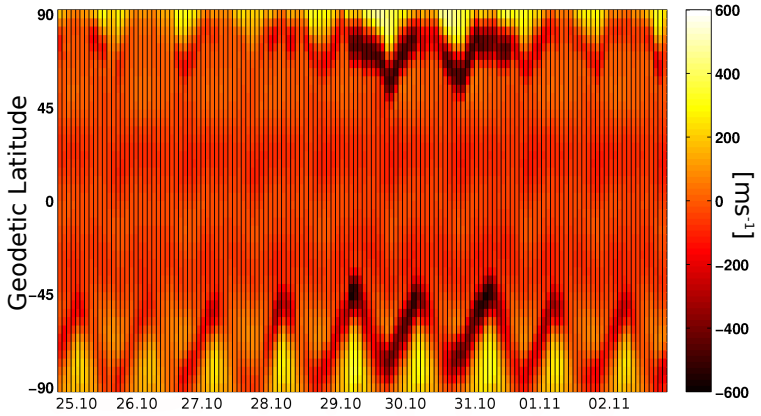

Figure 4.8: Dayside cross-track winds from the HWM07 wind model for the GRACE B S/C: Oct.25 - Nov.02, 2003 | LT: 16:20

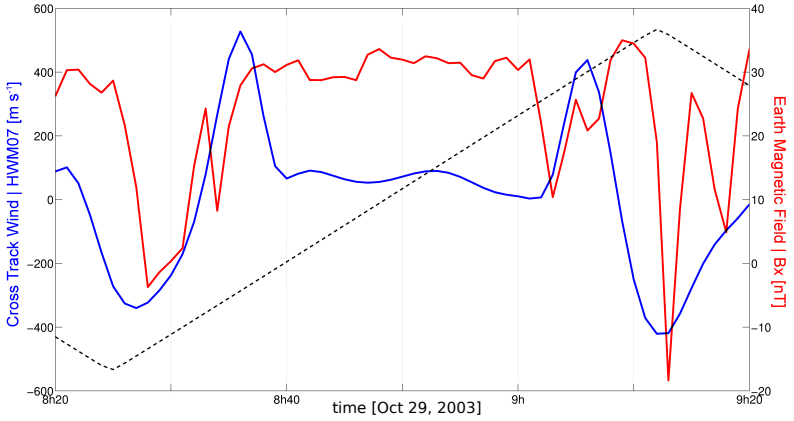

Figure 4.9: Comparison of Earth magnetic field in B_x observed by the WIND satellite (red), cross-track winds from the HWM07 wind model (blue), and the geographic latitude (dashed line) on October 29, 2003

effect, we can recognise in Fig. 4.8 that the wind speeds at low latitudes originated almost always westward (w.r.t y-axis) and are significantly smaller (< 200 ms^{-1}), independent of day- or night-time.

Finally, if we combine both effects, the impact of the co-rotating Earth atmosphere and the influence due to the independent wind speed, we obtain a drift angle θ for the GRACE S/C in the order of about ± 5 degrees depending on whether the S/C are orbiting in an ascending or descending arc.

Now that the influence of the co-rotating Earth's atmosphere and the horizontal winds on the attitude of the S/C have been considered, the force coefficients C_{D} and C_{L} can be determined for each panel separately (Eq. 4.6, 4.7). The individual contributions of each satellite panel are summed up according to Eq. 4.16 unless they are shadowed by any other plate.

$$C_{\mathrm{D}} = \frac{\sum C_{\mathrm{D,i}}\ A_{\mathrm{ref,i}}}{\sum A_{\mathrm{ref,i}}} \quad \text{and} \quad C_{\mathrm{L}} = \frac{\sum C_{\mathrm{L,i}}\ A_{\mathrm{ref,i}}}{\sum A_{\mathrm{ref,i}}}. \tag{4.16}$$

Concerning the final density determination process these coefficients are added to a total drag force coefficient C_{F} whereby the lift force makes up ∼1%. In the left panel of Fig. 4.10 a histogram of C_{F} for GRACE is shown during the period July 13, 2003 to December 28, 2010. As we can see, the resulting force coefficient C_{F} varies between 2.8 and 3.5, with a average value of ∼3.0. The uneven distribution of the coefficient can be explained by the long analysis period. To illustrate this fact,

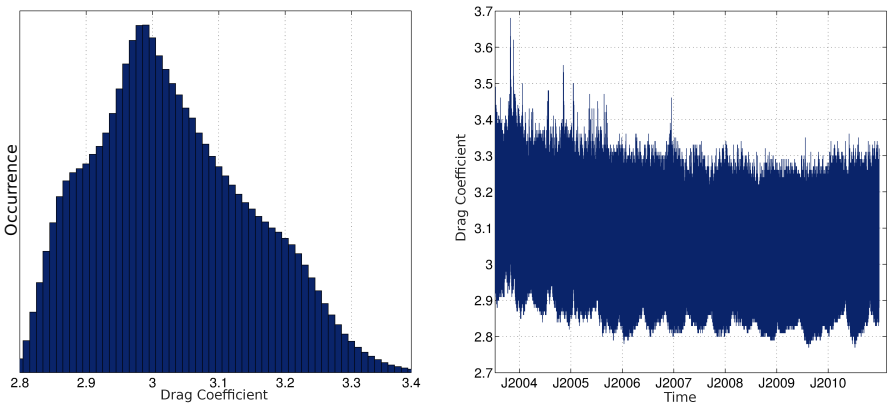

Figure 4.10: On the left side the histogram of the drag force coefficient C_{F} for the GRACE S/C is shown for the period between July 13, 2003 and December 28, 2010. The right panel illustrates the developing of the coefficient during the same period.

the right panel of Fig. 4.10 shows the coefficient during the complete period of investigation. It can be clearly seen that the coefficient decreases at the end of solar cycle 23 in 2008 due to the low solar activity. Furthermore, it has to be noted that the main variation is caused by the elliptical satellite orbit whereby the coefficient increases with decreasing altitude. In case of GRACE the difference in altitude from orbit eccentricity is approximately 50 km.

Since each variable in Eq. 4.2 is now known, it is possible to determine the densities of the Earth's neutral atmosphere. But before the first results of these atmospheric densities based on GRACE accelerometer measurements are presented, an estimation of the achieved accuracy and a discussion of possible error sources shall be performed.

4.1.3 Error Analysis

Since the determination of atmospheric densities is based on both observations and modelling, the resulting densities are affected by both measurement and modelling error [Bruinsma et al., 2004]. Concerning the measurements we have three error sources: the measurement noise, the calibration bias and the calibration scale factor. The main error source in the modelling process can be related to the

- acceleration calibration,
- drag coefficient, and
- neglecting of horizontal winds.

Tab. 4.1 a summarises the required data and their accuracy.

Parameter	**Formal Error**	**Source**
Bias factor	3–5×10^{-9} [m s^{-2}]	Bruinsma et al. [2007]
Scale factor	0.002	Bruinsma et al. [2007]
Uncal. accel. (x-axis)	1×10^{-10} [m s^{-2}]	Touboul et al. [1999]
Orbital position	0.05 [m]	Kang et al. [2006]
Orbital velocity	3×10^{-6} [m s^{-1}]	data product GNV1B
Model temperature	20%	Bruinsma and Forbes [2003]

Table 4.1: Summary of data products which were used in the density determination along with their specified accuracy.

Using these values it is possible to estimate the error in the atmospheric density by building partial derivatives of the specific function $f(x_1, x_2, ..., x_n)$ with respect to the individual parameters $(x_1, x_2, ..., x_n)$. The Gaussian covariance propagation assuming uncorrelated errors can be written as

$$\sigma_{\mathrm{f}} = \sqrt{\sum_{i=1}^{n} \left(\frac{\partial f}{\partial x_i} \right)^2 \sigma_{x_i}^2}. \tag{4.17}$$

The resulting uncertainties in the neutral density, due to the different error sources are summarised in Tab. 4.2. In the case of the horizontal winds, the atmospheric density were estimated once with and once without the HWM07 model.

Further error sources, stemming from the modelling of the radiation pressure, the precision of the instrument as well as the attitude of the S/C and macro-model are considerably less than

Error Source	Uncertainty in Neutral Density
Acceleration Calibration	∼2–4%
Drag Coefficient	∼5–6%
Neglect Horizontal Winds	∼5%

Table 4.2: Summary of uncertainties in the neutral density, due to different error sources.

1% [Doornbos et al., 2009, Sutton et al., 2008]. However, it has to be noticed that in the determination process of the drag and lift coefficient, several assumptions (e.g. molecular mass, accommodation coefficient) were made which certainly introduce an additional level of uncertainty on the resulting force coefficients and the associated atmospheric density.

4.2 Atmospheric Densities based on Accelerometer Measurements

Based on the previously discussed algorithm, atmospheric densities were calculated for a period covering 7 and a half year, starting in July 13, 2003 and ending on December 28, 2010. Thus, the period of investigation covers both high and low solar activities. Figure 4.11 illustrates the last two solar cycles in terms of sunspot number and highlights in red the determination period. Unfortunately, the GRACE S/C were not in space during the solar maximum in 2001 and 2002.

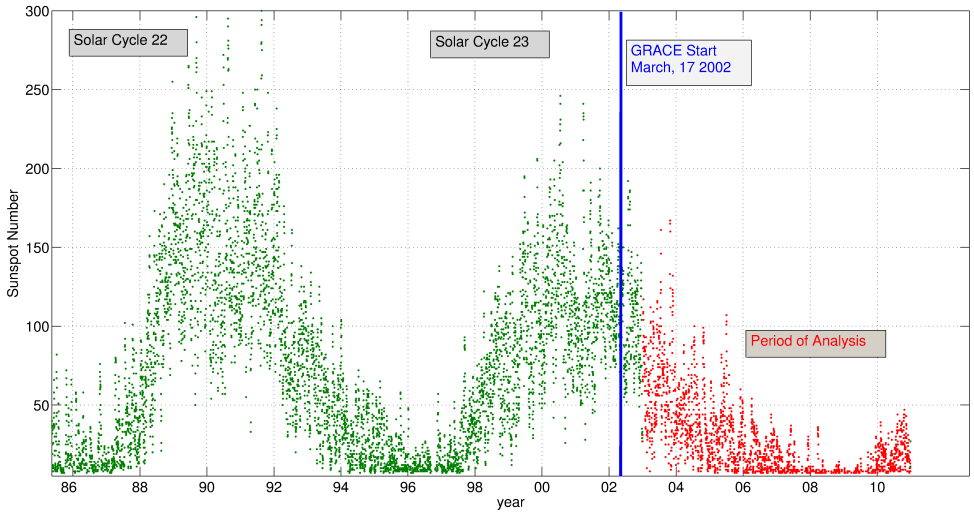

Figure 4.11: Illustration of the last two solar cycles 22 and 23 in terms of sunspot numbers. The blue line indicates the launch date of the GRACE S/C, and marked in red is the period of investigation (July 13, 2003 - December 28, 2010).

However they recorded, for instance, the impact of the solar events during the Halloween period in 2003.

The maximal possible temporal resolution of the computed densities depends on the lowest sampling rate of all data products. In our case these are the satellite ephemeris and the satellite mass data which are available with a sampling interval of one minute. In Sec. 3.3 it was shown that the accelerations are correlated with the varying altitude of the satellite. To overcome this issue, the calculated atmospheric densities ρ are normalised to an average height level of 490 km [Bruinsma et al., 2006]. In order to receive the normalised density ρ_{490} at this altitude, the empirical model JB08 must be evaluated at the true GRACE orbit height and at a constant altitude of 490 km, thus obtaining the densities ρ_{M} and ρ_{M490}. These densities can then be used to normalise the previously calculated density ρ using

$$\rho_{490} = \frac{\rho_{\mathrm{M490}}}{\rho_{\mathrm{M}}}\,\rho. \tag{4.18}$$

In the further course of the study, when we talk of normalised densities, they will always refer to an average height level of 490 km.

Another feature, addressed in Sec. 3.3, is the density variation, which arises due to day- and nightside observations. To illustrate this variation, Fig. 4.12 depicts densities for an arbitrary period of six days in 2006. Due to the absorption of the X-ray and UV radiation, the temperature

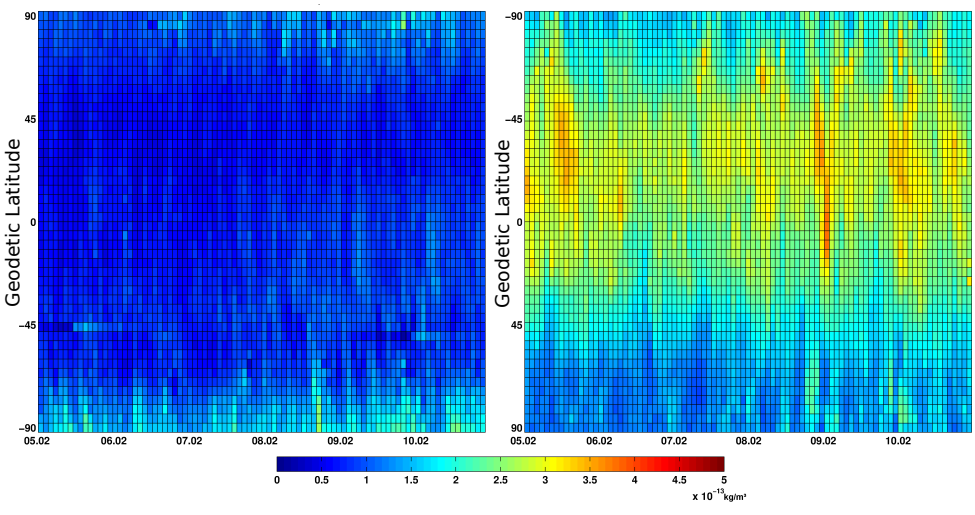

Figure 4.12: Normalised densities of the Earth's atmosphere for six days in February 2006. The left panel shows observations on the nightside at ∼02:50 UT, and the right panel the calculated densities on the dayside at ∼14:50 UT.

rises on the dayside and leads to an expansion of the complete layer. Thus, the calculated densities

are significantly higher compared to those on the nightside. In the further course of the study the density will always refer to the dayside, unless specified differently.

Before examining the response of the atmosphere during the famous Halloween period in 2003, Fig. 4.13 presents a complete time-series of normalised atmospheric densities from July 13, 2003 to December 28, 2010. In accordance with the solar activity (Fig. 4.11), we can clearly see, that

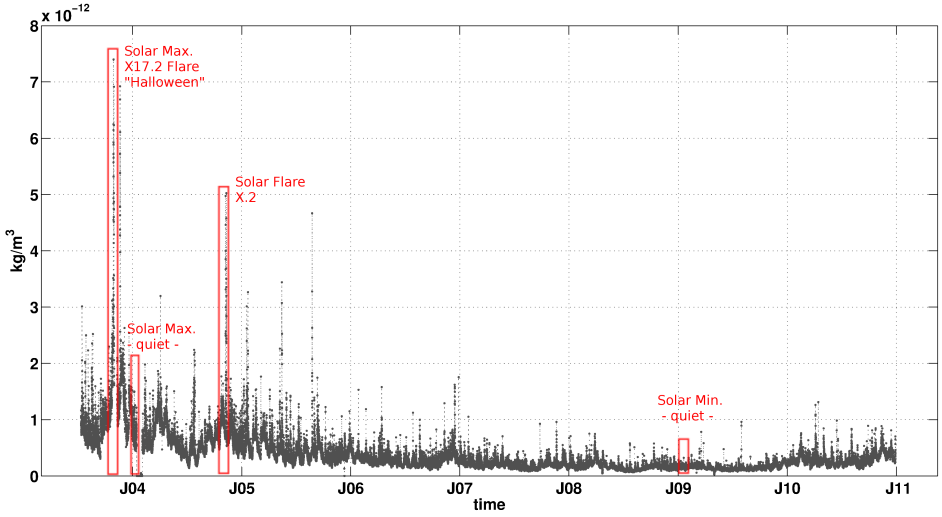

Figure 4.13: Dayside atmospheric densities based on GRACE A accelerometer measurements from July 13, 2003 to December 28, 2012. The densities are normalised to an average height level of 490 km. Marked with red rectangles are periods, which will be discussed in the upcoming part of the thesis - including the Halloween period in 2003, the impact of a X2.0 solar flare in 2004 as well as two short periods - one near solar maximum and the other during solar minimum.

the densities are decreasing towards the end of the solar cycle 23. The segments, marked with red rectangles illustrate specific periods of time which will be part of the density analysis in the further study. Of special interest are the Halloween period in 2003, the impact of a X2.0 solar flare in 2004 as well as two short periods - one near solar maximum and the other during solar minimum.

During the analysis of the accelerations in Sec. 3.3 it has been shown, that due to the small distance between the two GRACE satellites, the accelerations were nearly identical. To illustrate that the same is true for the atmospheric mass densities, Fig. 4.14 shows exemplarily the computed densities for both GRACE A and B for a short period in July 13, 2003. It can be recognised that both S/C indeed yield nearly identical densities. Compared to the absolute accelerations in Fig. 3.8, we see slightly larger variations among the solutions. The reason for this behaviour is the lower sampling rate of one minute and the associated smoothing effect. Nevertheless, Fig. 4.14 demonstrates that the densities from both GRACE S/C represent the response of the atmosphere in the same way.

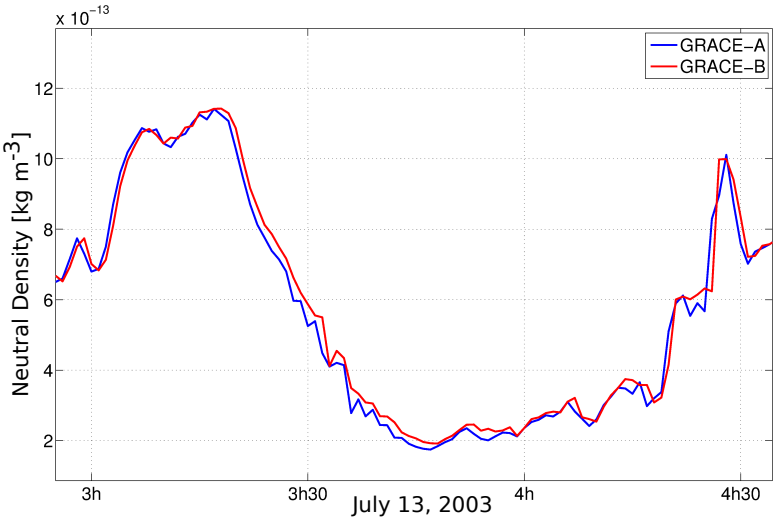

Figure 4.14: Atmospheric densities based on accelerometer measurements from GRACE-A and GRACE-B during on satellite revolution in July 13, 2003.

In the further course of the study we will limit ourselves to display only densities concerning the GRACE-A satellite.

4.2.1 The Halloween Period in 2003

As already stated in Sec. 2.1.4, several X-class flares and associated CME occurred during the Halloween period late October and early November 2003. Since the GRACE S/C were already in space at this time, the impact of these solar events on the Earth's environment must actually have been recorded. In this context, it is crucial to distinguish between an impact originated from a solar flare and a CME.

Since the electromagnetic radiation from a solar flare travels at the speed of light, the impact on the Earth's atmosphere is observable about 8.5 minutes after the eruption. Contrary to that, the velocity of the particles ejected by a CME is much lower and thus, the influence on the upper Earth's atmosphere occurs much later. For example, the CME which was associated with the X17.2 solar flare on October 28 was one of the fastest ever recorded, with a velocity of ∼2200 km s^{-1}. This gives a transit time of about 19 hours from the Sun to the Earth. Accordingly, Fig. 4.15 shows the estimated normalised atmospheric densities from October 28 to 30, 2003. The vertical black lines indicate the eruption time of the X17.2 and the X10.0 solar flare. The impact due to the electromagnetic radiation originating from the flares are marked with vertical lines in cyan. The perturbations related to the associated CMEs are indicated with red vertical lines. It can be

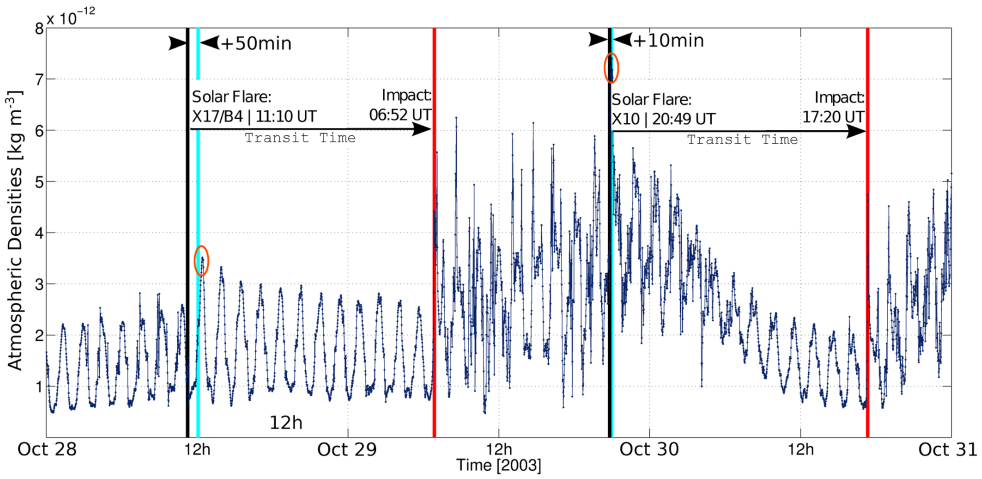

Figure 4.15: Illustration of the transition time between the solar eruptions and the time when the CME hits the upper Earth's atmosphere.

recognised that the impact due to the X17.2 solar flare occurs approximately 50 minutes after the explosion. As stated above, the satellite should measure the perturbation within 8 minutes under normal conditions. However, since GRACE entered the Earth's shadow shortly before the eruption (11:28 UTC, $\phi_{\mathrm{GRACE}} \approx 70°\mathrm{N}$) and remained on the nightside for ∼47 minutes, this density increase can still be related to the X17.2 solar flare, even if it does not reflect the peak intensity of the solar flare. By analysing the times when the the charged particles of the CMEs disturbed the Earth's atmosphere, we see a good consistency with the estimated transit times for both CMEs.

In the case of the second X10.0 solar flare, the impact on the S/C occurs indeed 10 minutes after the outburst. However, since at that time also the CME, associated with the first flare, disturbs the Earth atmosphere, a distinction between the two sources is difficult to realise. Thus, in the present study, the X17.2 solar flare is of major interest. Figure 4.16 depicts the impact of this first event on the Earth atmosphere and the associated density variations in a latitude vs. time plot. Several irregularities appear which can be attributed to the solar events that happened on October 28 at 11:10 UT. As already seen in Fig. 4.15, shortly after 12:00 UT, we observe the first sudden rise in neutral dayside densities of approximately 60% compared to the preceding density values at the equatorial and mid latitudes (Fig. 4.16, region 1). As already discussed, these variations can be related to the electromagnetic radiation of the solar flare. The major impact appeared 19 hours later, when the shock wave of the large CME disturbed the Earth's magnetic field. This lead to a significant increase of the accelerations and thus the neutral density of more than 300% (Fig. 4.16, region 2) compared to the densities before the event. Unlike the density behaviour during the flare

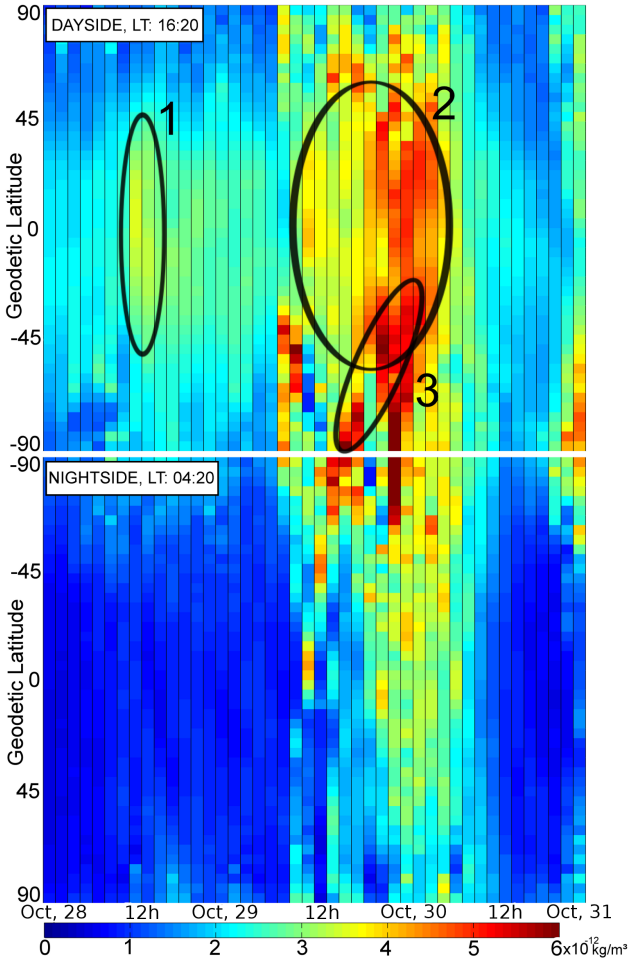

Figure 4.16: Response of the Earth's upper atmosphere to a solar flare and CME in terms of normalised neutral densities determined from GRACE satellite accelerations. The upper panel shows dayside densities at ∼16:20 LT, the lower panel the nightside at ∼04:20 LT. Region 1 corresponds to the measured density enhancement at the satellite orbit location caused by the X17.2 flare. Area 2 and 3 are density enhancements which originated one day after the flare exposure due to the accompanied CME and related high energy particle events.

on October 28, the density increased also on the nightside of the planet. During the night time the largest density enhancements were observed at high latitudes near the South Pole.

One more important detail can be observed in Fig. 4.16 during October 29 on the dayside, namely a travelling atmospheric disturbance which propagates from high latitudes towards the equator within a few satellite revolutions (Fig. 4.16, region 3). Such a longitudinally extended wave front is a response to sudden energy and momentum deposition in the high latitude thermosphere mostly in form of Joule heating [Bruinsma and Forbes, 2008].

However, beside the variation of the non-gravitational accelerations and thus, the atmospheric densities, the effects of such solar events can also be seen in various other satellite and Earth based observations. Since empirical models, discussed in the Sec. 5, are often based on such measurements, the following subsection comprises an analysis of such datasets.

4.3 Comparison with space weather observations

Based on terrestrial and satellite observations, there exists a wide range of geomagnetic and solar indices, which are often used as input parameters for empirical thermosphere models. Thus, possible weaknesses or limitations of a specific index will certainly effect the results of the models. Therefore, this section serves to analyse and to compare the indices with the computed GRACE densities. However, firstly the densities shall be compared not with a specific index, but with in-situ measurements from GOES.

4.3.1 GOES Measurements

The first satellite of a series of GOES was launched in 1975. Since then 14 further S/C were brought into a geostationary orbit. The main task of these satellites, which are operated by the United States National Environment Satellite, Data and Information Service, is weather monitoring and forecasting. Since the beginning, all GOES satellites are equipped with Space Environmental Monitoring instruments. Thus, magnetometer records and data concerning energetic particles and soft X-ray radiation are available since 1975. On July 23, 2001 the GOES-12 S/C was launched, having additionally a solar X-ray Imager (SXI) on board. In Fig. 4.17 observations of GOES-10, in terms of solar X-rays, proton fluxes and records from the earthward component of the magnetic field are illustrated during the Halloween period. In the upper two panels the course of the solar X-rays and the proton flux are given. A significant increase can be observed around noon on October 28 when the X17.2 solar flare arises. Furthermore, we see an increase due to the X10.0 flare which occurred at about 20:50 on October 29. In the bottom panel of Fig. 4.17 the measurements of the earthward magnetic field are displayed. In accordance with the analysis of the atmospheric mass densities, we can see the impact of the charged particles from the CME on the Earth's magnetic field on October 29.

4.3.2 Geomagnetic and Solar Indices

In order to get information on the present status of the geomagnetic and solar activity level various indices have become established over years. In the following subsections a description of several

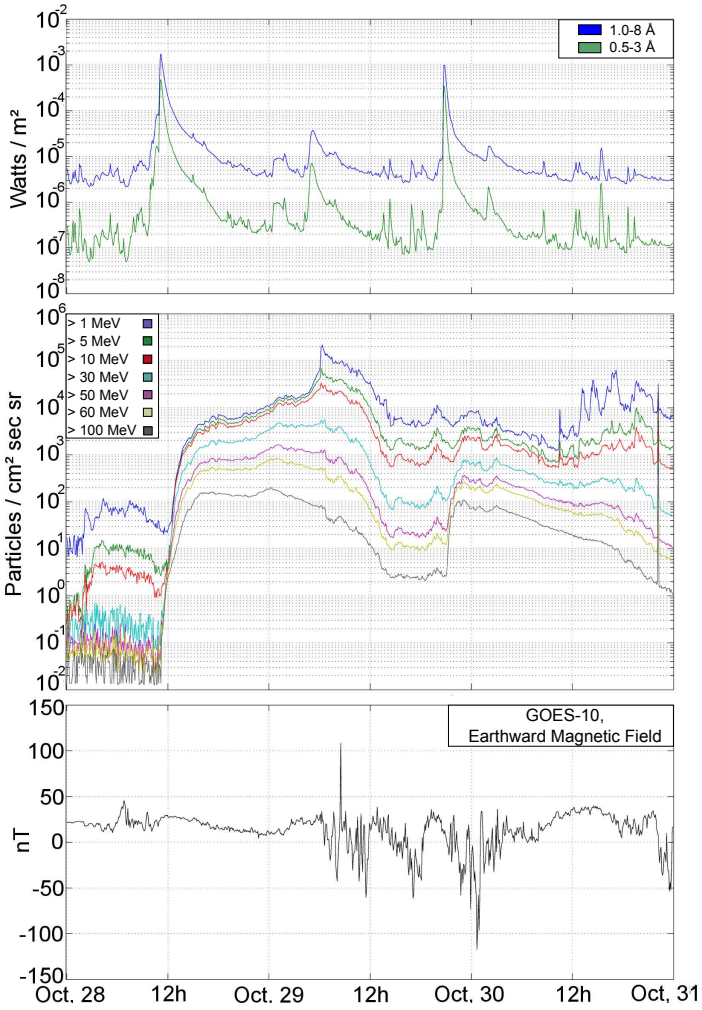

Figure 4.17: Satellite measurements by the geostationary GOES-10 S/C during the Halloween period in 2003. The upper panel shows the solar X-rays, in the middle panel records from the proton fluxes are illustrated. The bottom panel displays measurements from the earthward component of the magnetic field. All data records were obtained by the National Geophysical Data Center (NGDC).

observation based indices is given.

4.3.2.1 K-Index

Based on magnetometer measurements from 13 observatories mainly located at mid-latitudes in the Northern hemisphere (see Fig. 4.18), the planetary three-hour-range Kp index is computed [Bartels et al., 1939]. Thereby, the observatories monitor perturbations in the Earth's magnetic field in the three magnetic field components. At first, each site measures the maximum fluctuations of the horizontal component of the magnetic field compared to a quiet day at the site. This results in a

local, quasi logarithmic K-index ranging from 0 to 9. By using conversion tables which were devel-

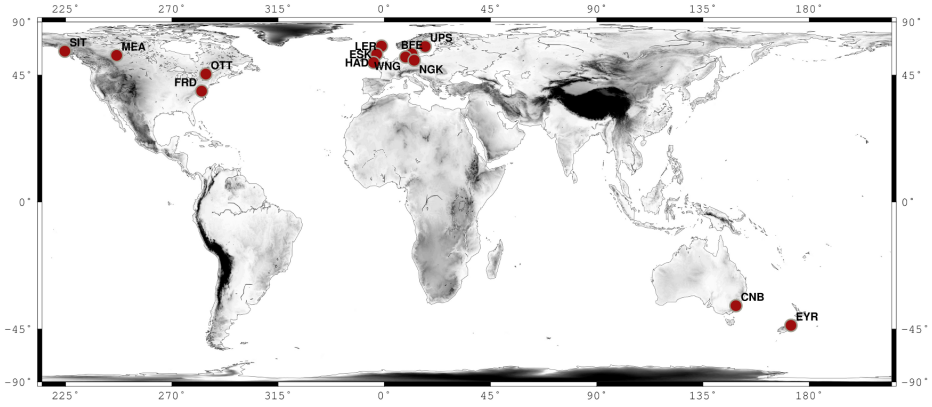

Figure 4.18: Map of the geomagnetic observatories used for the evaluation of the planetary K_p index.

oped by J. Bartels, it is possible to generate a standardized K_s index for each observatory. Since the definition of a "quiet day" is based on historical datasets at each observatory individually, a site at higher geomagnetic latitude needs larger fluctuations for a specific K_s. From these indices a global average can be derived which is known as the planetary K_p index. Both, the K_s and the K_p index are expressed in a range from 0 to 9, but in thirds of a unit (e.g.: 4- is 3 2/3, 4o is 4 and 4+ is 4 1/3).

A disadvantage of the logarithmic scaling of the K-indices is the fact that there is no linear relationship between the index and the measured magnetic fluctuations. Furthermore, the calculation of daily average values is not meaningful. For this reason, the so-called "equivalent three hourly range" index a_p was developed. It is a linear-scaled index and can be derived from the K_p index. Following Bartels the relationship between the geomagnetic indices K_p and a_p can be written as

$\mathbf{K_p}$	0o	0+	1-	1o	1+	2-	2o	2+	3-	3o	3+	4-	4o	4+
$\mathbf{a_p}$	0	2	3	4	5	6	7	9	12	15	18	22	27	32
$\mathbf{K_p}$	5-	5o	5+	6-	6o	6+	7-	7o	7+	8-	8o	8+	9-	9o
$\mathbf{a_p}$	39	48	56	67	80	94	111	132	154	179	207	236	300	400

Table 4.3: Relationship between the geomagnetic indices K_p and a_p.

As we can see from Tab. 4.3, the a_p index has also a fixed range with a maximum value of 400.

Hence, if a strong geomagnetic storm would exceed this upper limit, an empirical thermosphere model (e.g. MSISE-00), which solely uses this index as a proxy for the geomagnetic activity, would underestimate the impact of the specific event.

In the subsequent Fig. 4.19 normalised atmospheric densities as well as the a_p and the D_ST index (cf. Sec. 4.3.2.2) are illustrated for two weeks in January 2005. During this time several CMEs occurred, disturbing the Earth's magnetic field considerably. It is clearly visible that the

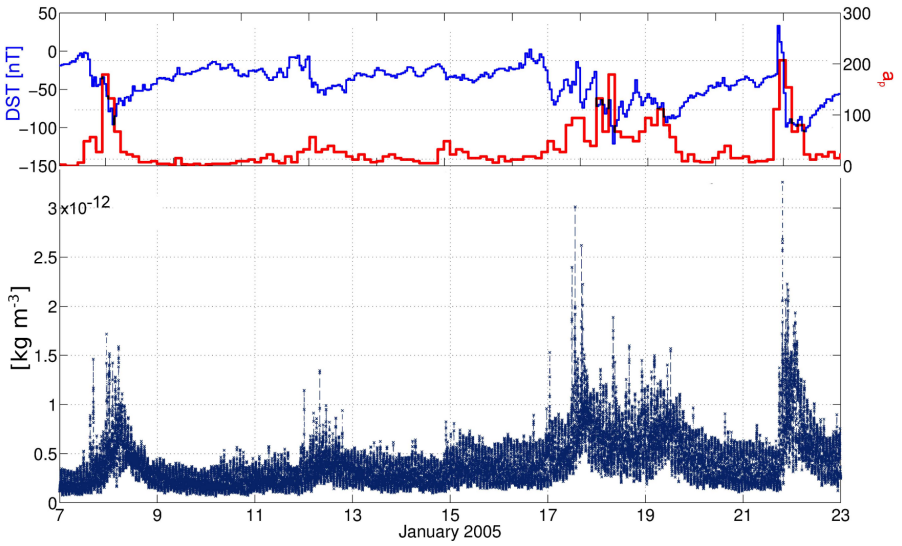

Figure 4.19: Normalised atmospheric densities calculated from GRACE acceleration measurements combined with the geomagnetic indices a_p (red) and D_ST (blue) for January 7 till January 22, in 2005.

atmospheric densities are in good agreement with both geomagnetic indices. However, due to the higher temporal resolution of the D_ST index it adjusts better than the a_p index does.

A variation of the K_p and a_p indices are the three hourly K_m and a_m geomagnetic indices, which are derived from measurements at 21 observatories located in the sub-auroral zones of the Northern and Southern hemispheres. The observatories are divided into different classes depending on their geographical longitude. When estimating global K_m and a_m indices, it is thus possible to balance the individual measurements depending on the longitude of the specific observatory. As in the case of the K_p and a_p indices, there also exists a conversion table between the K_m and a_m values, which is illustrated in Tab. 4.4.

Km	0o	0+	1-	1o	1+	2-	2o	2+	3-	3o
am	0.9	1.4	3.4	5.4	7.4	10.4	13.4	16.4	20.4	26.4
Km	3+	4-	4o	4+	5-	5o	5+	6-	6o	6+
am	33.4	40.4	50.4	60.4	70.4	86.4	103.4	120.4	146.4	173.4
Km	7-	7o	7+	8-	8o	8+	9-	9o		
am	200.4	243.4	286.4	330.4	386.4	443.4	500.4	611.4		

Table 4.4: Relationship between the geomagnetic indices K_{m} and a_{m}.

For further information about the computation of the various K-indices the interested reader is referred to Menvielle et al. [1995].

4.3.2.2 Disturbance Storm Time Index

Another benchmark for the geomagnetic activity is the D_{ST} index. It is based on measurements of the horizontal component of the Earth's magnetic field at four observatories and is expressed in units of nanoTesla. As we can see from Fig. 4.20, all of the sites are at lower latitudes, since observatories at higher latitudes can be blind to energy input during large storms [Huang and Burke, 2004].

The D_{ST} index is an indicator for the strength of the storm-time current in the inner mag-

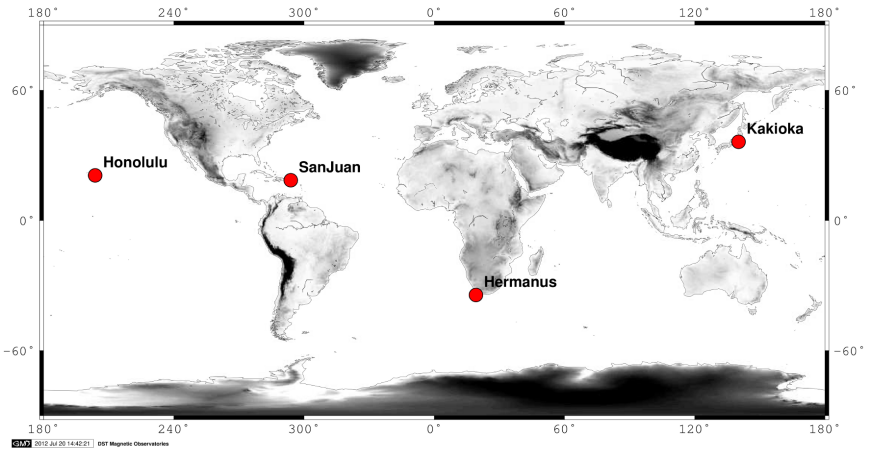

Figure 4.20: Distribution of the four low-latitude magnetic observatories (Honolulu, San Juan, Hermanus and Kakioka).

netosphere, with the advantage that it primarily responds to the magnetospheric variations. In

contrast to that, the previously described K_p index responds mainly to the currents flowing in the ionosphere. Also the higher resolution of the D_{ST} index (one hour) makes it possible to segregate different storm phases [Bowman et al., 2008], thus allowing a more detailed analysis of a geomagnetic storm.

In Fig. 4.21 the different phases of a geomagnetic storm which occurred in 2004 are shown [Bowman et al., 2008]. Additionally, the atmospheric densities calculated from GRACE are displayed in the background. It has to be noted that negative D_{ST} values indicate a geomagnetic storm in

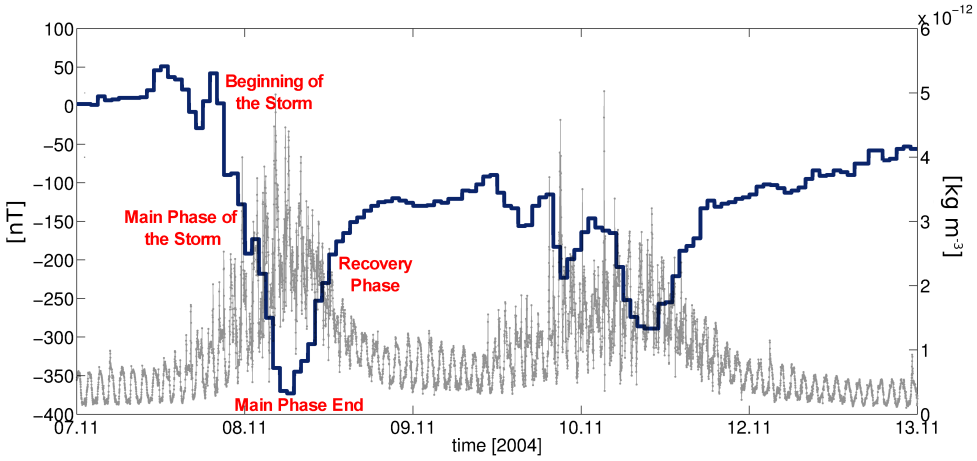

Figure 4.21: D_{ST} index (blue line) during a geomagnetic storms in November 2004. In the background the atmospheric densities (grey line) from GRACE observations are illustrated.

progress. The lower the values the more intense the storm. This is due to the fact that the strength of the surface magnetic field at low latitudes is inversely proportional to the energy content of the ring current. During the main phase of a geomagnetic storm the electric current becomes highly energised due to the impact of the solar wind and produces southward-directed magnetic field perturbations at low latitudes. Thus the direction is opposite the normal field direction [Tobiska et al., 2008b, Bowman et al., 2008]. As we can see in Fig. 4.21, the D_{ST} index suddenly decreases at the beginning of the storm. After the main phase, in the so-called recovery phase, the index slowly increases since the the energy in the ring current decreases.

4.3.2.3 International Sunspot Number (ISN)

The first observation of sunspots were performed by Thomas Harriot and Galileo Galilei in 1610 and provided an indication of the rotation rate of the Sun. In 1749, the first regular daily observations were made at the Zurich observatory in Switzerland. Later on, in 1848, the first systematic

observations of the total number of visible sunspots on the Sun and the number of sunspot groups were performed by Rudolf Wolf.

Based on an 18-year sunspot dataset, Heinrich Schwabe discovered the 11-year sunspot cycle which was already mentioned in the Sec. 2.1.1. Since the counting of the sunspots depends on the ob-

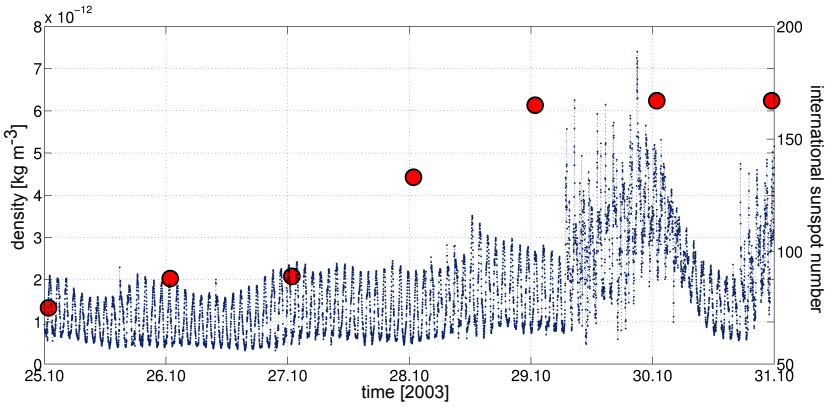

Figure 4.22: Comparison between the atmospheric density (blue line) and the international sunspot number (ISN; red dots) during the Halloween Period in 2003.

server's interpretation and experience, the official daily ISN represents an average value, computed from measurements within a complete network of observatories. In Fig. 4.22 a comparison between the computed densities and the ISN during the Halloween period is shown. We see at a glance that the ISN can only roughly reproduce the course of the densities due to the daily resolution.

4.3.2.4 $F_{10.7}$ Index

The solar radio flux, $F_{10.7}$, represents the actual solar flux at a wavelength of 10.7 cm (2880 MHz) and is given in sfu. The first measurements on a daily basis were done by Covington in 1948. Today, the estimates stem from ground-based observations made by the radio telescope located in Penticton, British Columbia.

The measured radiation originates in the solar low and cooler corona, by electrons in thermal free-free emission in the vicinity of sunspots. Since the radiation does not interact with the Earth's atmosphere, it can be measured all the way to the Earth's surface [Tobiska et al., 2008b]. There are observations at 17h, 20h and 23h UTC, where the value at 20h UTC is archived and provided to the community.

During the processing of the observations, variations due to solar flares are defined as contaminants and filtered from the data [Tapping and Charrois, 1994]. The $F_{10.7}$ index is recognised as a good solar EUV proxy. In most of the thermospheric models it is exclusively used to describe the solar

energy available for thermospheric heating. Based on the previously discussed ISN it is possible to roughly estimate the solar radio flux $F_{10.7}$ by

$$F_{10.7} = 67.29 + 0.316\ \text{ISN} + 0.01084\ \text{ISN}^2 - 0.006813\ \text{ISN}^3 + 0.0000001314\ \text{ISN}^4. \tag{4.19}$$

Thus, it is possible to calculate a predicted $F_{10.7}$ index from the prediction of the sunspot numbers.

4.3.2.5 $M_{10.7}$ Index

The $M_{10.7}$ index is based on measurements by the Solar Backscatter Ultraviolet (SBUV) spectrometer [Frederick et al., 1986] aboard the NOAA 16, 17, 18 satellites. The main purpose of the instrument is the monitoring of the ozone in the Earth's lower atmosphere. However, it also provides discrete measurements of the solar middle ultraviolet radiation. Thereby, the solar spectral band at 280 nm is observed, which comprises photospheric continuum as well as chromospheric line emissions [Tobiska et al., 2008b]. This means that the satellite measures on the one hand the weakly varying photospheric wings, and on the other hand the chromospheric Mg II h and k lines at 279.56 and 280.27 nm.

Based on this data, the $M_{10.7}$ index is derived from the Mg II core-to-wing ratio (cwr), which denotes the relation between the variable core lines and the nearly non-varying wings [Bowman et al., 2008]. In order to be consistent, a linear regression with $F_{10.7}$ is done to gain the $M_{10.7}$ index in units of sfu. Finally, it shall be noted that also the SORCE/SOLSTICE and the ERS-2/GOME satellites perform Mg II cwr measurements.

4.3.2.6 $S_{10.7}$ Index

This index is based on observations recorded by the SOHO satellite which operates in the Lagrange Point 1 on the Earth-Sun line. Measurements of the 26–34 nm solar EUV emission are taken by the Solar Extreme-ultraviolet Monitor (SEM) with a sampling rate of 15 seconds. The EUV emission lines are dominated by the chromospheric He II line at 30.4 nm and the coronal Fe XV at 28.4 nm. The energy stems from solar active regions and is mostly absorbed by atomic oxygen in the thermosphere above 200 km.

Again, as in the case of the $F_{10.7}$ index, variations due to solar flares are eliminated in the data processing. Additionally, the data are converted to sfu based on a first degree polynomial fit with the $F_{10.7}$ index.

4.3.2.7 $Y_{10.7}$ Index

The most recently developed solar index is the $Y_{10.7}$ index. It is based on 0.1–0.8 nm solar X-ray emissions recorded by the GOES X-ray spectrometer (XRS) and Lyman-α emission, observed by TIMED/SEE and the SOLSTICE instrument aboard the UARS and SORCE satellites.

The solar X-rays stem from the cool and hot corona and represent a combination of bright solar active regions and solar flares [Tobiska et al., 2008b]. In the Earth's atmosphere, the photons are absorbed by molecular oxygen O_2 and molecular nitrogen N_2 at an altitude between 85 to 100 km. During medium and low solar activity the main energy source in these atmospheric regions is dominated by the Lyman-α emission, which is created in the upper chromosphere and in the transition zone. When estimating the $Y_{10.7}$ index, the GOES X-ray data are reduced by the flare component. Thus, they only represent the background radiation.

In order to summarise these last four solar indices, a comparison between the indices and the

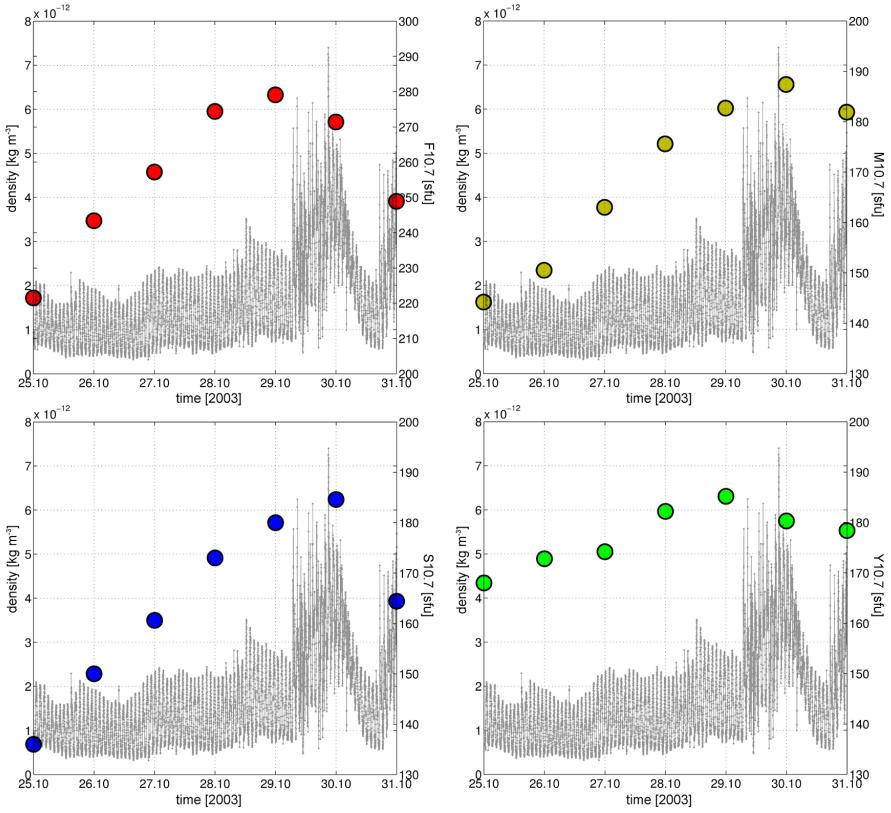

Figure 4.23: Comparison between the computed atmospheric mass densities (grey lines) and the solar indices $F_{10.7}$ (red dots), $S_{10.7}$ (blue dots), $M_{10.7}$ (yellow dots) and $Y_{10.7}$ (green dots) during the Halloween period in 2003.

computed atmospheric mass densities is shown in Fig. 4.23. The upper two panels illustrate the daily estimates of the $F_{10.7}$ radio flux and the $M_{10.7}$ index combined with the GRACE densities in the background. In the lower panels the solar indices $S_{10.7}$ and $Y_{10.7}$ are displayed together with the calculated densities from GRACE.
As we can see, all four solar indices can only roughly reproduce the behaviour of the densities due to the poor temporal resolution of one day. However, due to the fact that each of these indices map the energy from various solar irradiance sources into different atmospheric layers, a combined usage of all of them is certainly advantageous.

To conclude this section, Tab. 4.5 and Tab. 4.6 present an summary of the $F_{10.7}$, $S_{10.7}$, $M_{10.7}$ and $Y_{10.7}$ indices and lists some of their characteristics as stated in Tobiska et al. [2008b].

Solar Index	**Spectral Sub-category**	**Wavelength [nm]**	**Solar Source Temperature Region**	**Atmosphere Absorption [km]**
$F_{10.7}$	Radio	10.7×10^7	Transition region Cool corona	90-500
$M_{10.7}$	FUV	160	Photosphere Lower Chromosphere	95-110
$S_{10.7}$	EUV	26–34	Chromosphere Corona	200-300
$Y_{10.7}$	X-rays H Lyman α	0.1–0.8 121	Chromosphere, Hot Corona Transition Region	85-100

Table 4.5: Solar indices related to atmospheric heating [Tobiska et al., 2008b]

Solar Index	**Observing Facility**	**Instrument**	**Observation Time Frame**	**Measurement Cadence**
$F_{10.7}$	Penticton Observatory	Radio Telescope	1947–2009	3/day
$M_{10.7}$	NOAA-16,17,18 SORCE, ERS-2	SBUV,GOME SOLSTICE	1991–2009	2/day
$S_{10.7}$	SOHO, GOES	SEM, EUVS	1996–2009	15 seconds
$Y_{10.7}$	GOES-12, UARS SORCE, TIMED	XRS, SEE SOLSTICE	1991–2009	1min; 16/day

Table 4.6: Characteristics of daily JB08 solar indices [Tobiska et al., 2008b]

Chapter 5

Empirical Thermosphere Models

Over the last 50 years a large number of atmosphere models was developed in order to predict atmospheric temperature and densities. One of the first global models of the upper atmosphere was published by L.G. Jacchia in 1965 [Jacchia, 1965]. It is based on measurements of air drag acting on satellites, and represents thermospheric temperature profiles by an exponential equation, which increases asymptotically to the exosphere temperature. Atmospheric densities are calculated by assuming fixed boundary conditions at 120 km. Above this altitude, a diffuse distribution for each species is assumed. Revised versions of the model are the Jacchia-70 [Jacchia, 1970] and Jacchia-71 [Jacchia, 1971], which extended the predictions down to 90 km.

On June 6, 1969 the satellite mission Orbiting Geophysical Observatory-6 (OGO-6) was launched. The S/C carried a mass spectrometer which made the first in-situ measurements of atmospheric parameters possible. In March 1972 a first model based on this type of observations was presented [Hedin et al., 1972]. In analogue to the Jacchia-65, the model assumed fixed boundary densities at 120 km.

Since the temperature variations estimated by the OGO-6 model were similar to those found by the incoherent scatter radar (ISR) technique, revised versions of the model were named after these datasets: mass spectrometer and incoherent scatter data (MSIS).

During the following 30 years several improved MSIS models (MSIS-77, MSIS-83, MSIS86, MSIS90E, NRLMSISE-00) have been developed. A description of the latest NRLMSISE-00 will be given in the next section.

In addition to the MSIS-class models, a revised Jacchia model, J77 [Jacchia, 1977], based on in-situ measurements by OGO-6 and ESRO-4 satellites, was established in 1977. Based on the J70, NASA developed the Marshall Engineering Thermosphere model (MET, Hickey [1988]) in the late 1980's and provided an update called MET-2.0 [Owens, 2002] in 2002.

Since the beginning of the 21th century, the Jacchia models were further developed and published as Jacchia-Bowman 2006 (JB06, Bowman et al. [2007]), followed by an improved version JB08. Concerning the input parameters of the JB08 model, fundamental modifications were made by introducing three new solar indices ($M_{10.7}, S_{10.7}, Y_{10.7}$) and the ring current index D_{ST}. A more detailed description of the new JB08 model will be given in Sec. 5.2.

Beside the MSIS and Jacchia-class models, there exist also several generations of the Drag Temperature Model (DTM) starting in 1978 [Barlier et al., 1978]. Just like the other models at that time, it is based on observations of the satellite drag force. In the following years, further upgrades were published in terms of DTM-94 [Berger et al., 1998], DTM-2000 [Bruinsma et al., 2003] and, most recently, the DTM-2009 thermosphere model [Bruinsma et al., 2012]. In this process, the DTM-2000 already introduced, beside the mostly used $F_{10.7}$ solar radio flux, a further solar proxy, namely the Mg II solar EUV.

All the above mentioned models provide at least values for the total mass densities and exospheric temperatures. In the course of this study, the newest version of the MSIS and Jacchia-class models, namely MSISE-00 and JB08 were analysed. In addition, a comparison with the computed neutral densities from accelerometer measurements aboard the GRACE satellites covering the period 2003 to 2010 was performed.

5.1 NRLMSISE-00

The NRLMSISE-00 (MSISE-00, Picone et al. [2003]) is an extension of the previous MSIS-class models and represents the latest version of the series. As in the predecessor model MSISE-90, ground, rocket, and satellite measurements, as well as data from ISR, mass spectrometer, solar UV occultation, pressure gauge, falling sphere and grenade detonations from 1965 to 1983 are included. The letter “E” in the model name indicates that it is applicable from the Earth’s surface to space. In addition to components used in the earlier MSIS-class models, some new categories are used in the MSISE-00 dataset:

- satellite drag and orbit determination during 1961 to 1973 [Jacchia, 1970, Barlier et al., 1978, Hedin, 1988],
- mass densities from satellite accelerometer and from orbit determination,
- lower thermospheric temperature from ISR covering 1981 to 1997, and
- molecular oxygen O_2 density, from solar UV occultation covering 1988–1997 (NASA Solar Maximum Mission, NASA/SMM).

Since the MSISE-00 database includes drag measurements and satellite accelerometer data in the same way as the Jacchia-class models at the time of their release do, MSISE-00 should be equal to or better than the Jacchia models up to version J77 in terms of density prediction.

Referring to the main drivers of the upper atmosphere the model only uses the daily 10.7 cm solar radio flux, $F_{10.7}$, as a proxy for the solar EUV and the three-hourly geomagnetic index, a_p, for the geomagnetic component of the space weather.

Table 5.1 summarises the input and output parameters of the model. It can be seen that apart from total mass density, also exospheric temperatures and densities of the most important atmosphere constituents in terms of number densities are provided. Speaking of atmospheric constituents,

Input	**Output**
Date and Time	He number density [cm^{-3}]
Time of Day	O number density [cm^{-3}]
Geodetic Position (ϕ,λ,h)	O_2 number density [cm^{-3}]
Local Apparent Solar Time	Ar number density [cm^{-3}]
F10.7 Solar Flux (81 day average)	H number density [cm^{-3}]
F10.7 Solar Flux (previous day)	N number density [cm^{-3}]
Geomagnetic Index A_p	N_2 number density [cm^{-3}]
(with different time delays)	Total Mass Density [g cm^{-3}]
	Anomalous Oxygen[cm^{-3}]
	Exobase Temperature [K]
	Temperature at Altitude [K]

Table 5.1: Input and output values for the MSISE-00 model.

the MSISE-00 model includes a new component for altitudes above 500 km, namely "anomalous oxygen". The component comprises hot atomic oxygen or atomic oxygen ions near the exobase.

From a mathematical point of view the MSISE-00 model uses functions, that include time-independent terms, spherical harmonic terms, time-dependent low-order harmonic terms as well as polynomial terms to represent the solar EUV proxy $F_{10.7}$ and linear and exponential terms for the geomagnetic activity. [Picone et al., 2003].

The free source code of the model can be obtained from the National Space Science Data Center (NSSDC)[1].

[1] ftp://nssdcftp.gsfc.nasa.gov/models/atmospheric/msis/

5.2 Jacchia-Bowman 2008

The JB08 model as well as its predecessor JB06 originate from the CIRA72 model [Jacchia, 1972]. Unlike other empirical thermosphere models, which mostly use the $F_{10.7}$ as a proxy for the solar EUV, these two models (JB06, JB08) include additional EUV and far ultraviolett (FUV) solar indices ($M_{10.7}, S_{10.7}, Y_{10.7}$) in order to map energy from specific solar irradiance sources to major thermospheric layers [Tobiska et al., 2008b].

This enabled the developers to include new semi-annual density variation equations using multiple 81-day average solar activity indices to take into account the variations in the semi-annual density cycle that result from long-term EUV heating [Bowman et al., 2008]. Additionally, exospheric temperature equations based on the solar indices were introduced to represent the thermosphere EUV and FUV heating effects.

A disadvantage of the new solar indices is, that they originate from satellite observations, which are not available prior to 1997 (e.q. SOHO/SEM). Hence, the model is only applicable for the time after January 1, 1997.

In addition to the solar indices, the JB08 model uses one of two geomagnetic indices, depending on the actual geomagnetic activity level. In principal, the three-hourly a_p index serves as input parameter. However, in case of a geomagnetic storm ($a_\mathrm{p} > 40$), the model switches from the a_p to the D_ST index. As mentioned in Sec. 4.3.2.2, the D_ST index has a higher temporal resolution of one hour. Thus it is possible to analyse the different storm phases (Fig. 4.21; Tobiska et al. [2008b]) more accurately. Apart from total mass densities, the model also provides exospheric temperatures. Tab. 5.2 summarises the output as well as the input parameters used in the JB08 model.

Input	**Output**
Date and Time	Total Mass Density
Geodetic Position (ϕ,λ,h)	Temperature at Altitude
Geomagnetic Index A_p	Exobase Temperature
Ring-Current Index D_{st}	
Daily and 81-day average solar indices:	
$F_{10.7}$, $M_{10.7}$, $S_{10.7}$, $Y_{10.7}$	
F_{81}, M_{81}, S_{81}, Y_{81}	

Table 5.2: Input and Output values for the Jacchia-Bowman 2008 thermosphere model.

In order to model specific physical and chemical processes, the indices are used with different time delays. $F_{10.7}$ and the $S_{10.7}$ are applied with a lag of one day, $M_{10.7}$ and $Y_{10.7}$ with a two and five days time delay, respectively.
Like the MSISE-00 model also JB08 is freely available at the model website[1].

5.3 DTM-2009

For the sake of completeness, also the most recently presented thermosphere model DTM-2009, developed in the framework of the Advanced Thermosphere Modelling and Orbit Prediction project (ATMOP; http://www.atmop.eu), shall be described in more detail. Actually, this model serves as a benchmark for the upcoming DTM releases in the near future. This is why it was not included in the present analysis.
DTM-09 uses data from the LEO satellite missions CHAMP (2001-2008), GRACE (2003–2008) and GOCE (Nov./Dec 2009 and Mar./Apr. 2010) and, in addition, observations of the geodetic satellites Starlette ans Stella from 1994 to 2008. As a solar proxy for the EUV the model uses the $F_{10.7}$ radio flux. Concerning the geomagnetic activity, the planetary geomagnetic index K_m is used.
Just like the previous DTM models, the exospheric temperatures and the partial density variations are modelled by means of a spherical harmonic function $G(L)$ which is used to describe the periodic and non-periodic variations. Recently added was a direct coupling of diurnal, semi-diurnal, and seasonal amplitudes at mean solar activity [Bruinsma et al., 2012]. The total mass density ρ at an altitude h is calculated as

$$\rho(h) = \sum_i \rho_i(120\text{km}) f_i(z) exp(G_i(L)), \tag{5.1}$$

where $f_i(z)$ denotes the height function per constituent which results from the integration of the differential equation of diffuse equilibrium.

5.4 Comparison between S/C Densities and Model Densities

Similarly to the density determination from accelerometer measurements, the empirical thermosphere models were evaluated for the period between 2003 and 2010, thus covering periods of high and low solar activity. Furthermore, the comparison between the resulting model density and those

[1] http://sol.spacenvironment.net/~JB2008/

from the GRACE observations is divided into two parts.

First, some specific periods during solar minimum and solar maximum are analysed. This includes the famous Halloween period in 2003, which already served as an example in Sec. 4.2. The key issue will be to investigate, whether the empirical models are also able to reconstruct the effect of both source - the solar flare and the CME.

Second, the results from the various sources are investigated for the complete research period from July 2003 to December 2010. The long analysis period allows a more reliable statement of how the models behave during different solar activity levels compared to the in-situ measurements.

5.4.1 Difference between Periods of Solar Minimum and Maximum

The first comparison between the GRACE densities and those from the empirical models covers two periods where no specific solar events occurred. In the left panel of Fig. 5.1 the densities are illustrated at the turn of the year 2003/2004, thus, it is a representative for a fairly solar active period. On the right side of Fig. 5.1 densities from January 2009 are shown - a period where the solar activity was extremely low. As expected, the densities from all three sources are

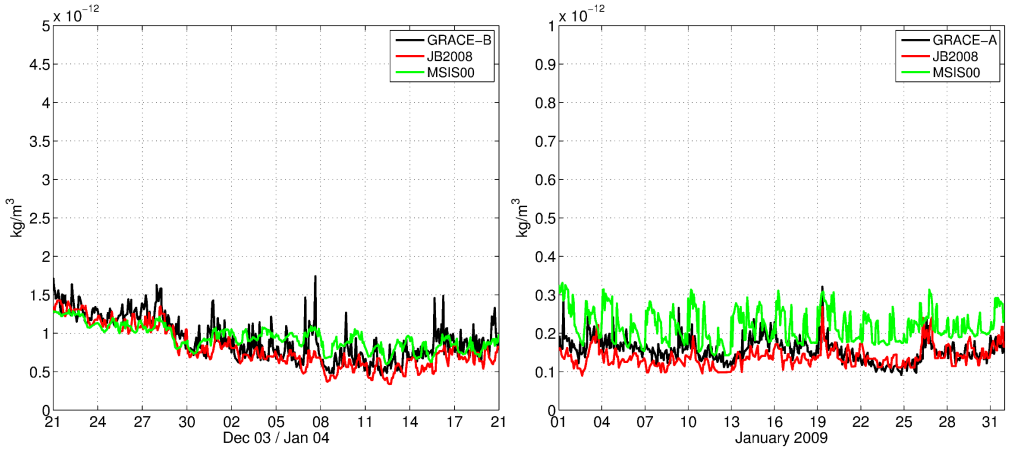

Figure 5.1: Comparison of atmospheric densities from GRACE in-situ measurements and empirical models during solar maximum (left panel) and solar minimum conditions (right panel).

significantly lower during solar minimum in 2009. The differences are in the range of approximately one magnitude. Concerning the empirical models, it can be recognised that the MSISE-00 delivers much higher mass densities during solar minimum than the other two sources. In times of solar maximum the results are in better agreement.

5.4.2 Atmospheric Densities during Disturbed Periods

As already known from Sec. 4.2.1, during the Halloween period in 2003 solar flares as well as CMEs have influenced the Earth's upper atmosphere. In the analysis of the GRACE densities it was possible to distinguish between the impact of the X17.2 solar flare on October 28 and the associated CME one day later. Fig. 5.2 depicts the computed day-side densities from accelerometer measurements as well as the evaluated densities from the empirical thermosphere models MSISE-00 and JB2008 during the Halloween period. Particularly before the perturbations triggered by the

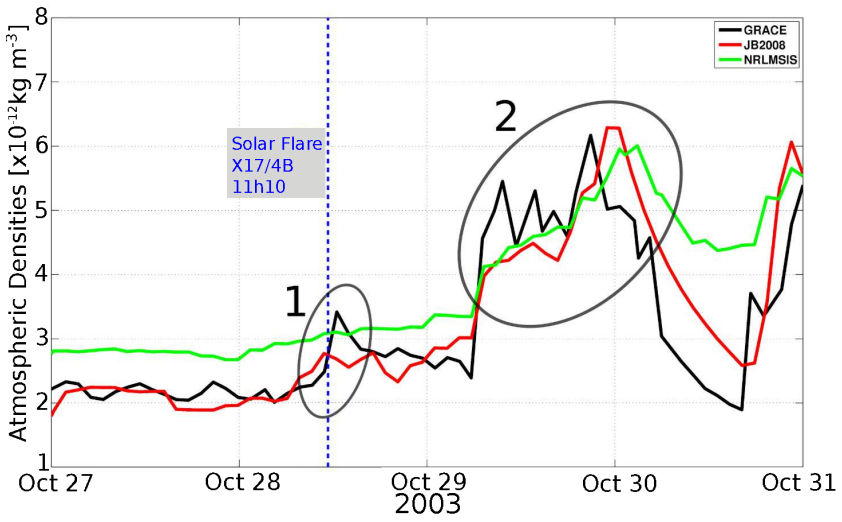

Figure 5.2: Comparison of day-side atmospheric densities during the Halloween period based on GRACE accelerometer measurements (black line) and the empirical thermosphere models JB08 (red line) and MSISE-00 (green line). Area 1 corresponds to the measured density enhancement caused by the X17.2 flare, area 2 marks the density variations due to the accompanied CME which originated one day after the flare exposure.

energetic particles occur (Fig. 5.2, region 2), the results of the JB08 are in good agreement with the GRACE measurements, while MSISE-00 shows a significant overestimation. Following Bowman et al. [2008], the overestimation of the MSISE-00 model before the storm can be attributed to an incorrect modelling of the solar EUV during this period. Furthermore, it is clearly evident that both models can not simulate the observed density response triggered by the solar flare (Fig. 5.2, region 1). The reason for this is the low temporal resolution of the solar indices of one day. Thus, short-term perturbations (∼90 min) caused by solar radiation are certainly not possible to simulate. Another issue that has to be kept in mind when evaluating the models are the time delays with which the specific solar indices are applied. As we have seen in the description of the

JB08 in Sec. 5.2, the model uses four solar indices ($F_{10.7}$, $S_{10.7}$, $M_{10.7}$, $Y_{10.7}$) with lag times varying between one and five days. This implies that due to the applied delay the model would still not recognise the impact of the solar flare even if we would calculate the solar indices with a higher resolution (e.g. $S_{10.7}$ is based on 15 s SOHO/SEM data).
In the case of the geomagnetic indices, a higher temporal resolution ranging from one to three hours is available. Hence, both empirical models show a better agreement with the in-situ measurements when the shock wave of the CME disturbs the Earth's magnetic field (Fig. 5.2, region 2). However, we can observe that compared with the GRACE measurement, the density decrease in time is too slow for both models.
In summary, the JB08 model shows a distinctly better agreement with the in-situ measurements than the MSISE-00 does during the disturbed Halloween period.

5.4.3 Long-Term Analysis

In the next step the models are compared to the in-situ measurements over the complete investigation period from July 13, 2003 to December 28, 2010. Since it was already shown that the models perform differently depending on the solar activity level, the resulting densities are divided into six classes, based on the 3-hourly K_P index. This means that each 3 h sample comprises two complete satellite revolutions. Table 5.3 summarises the deviation of the models from the reference solution based on GRACE acceleration measurements in percent. It can be seen that in particular the

Table 5.3: Deviation in percent of the total mass densities evaluated with the empirical models JB08 and MSISE-00 from the reference solution based on GRACE acceleration measurements. Investigation period: Jul. 13, 2003 to Dec. 28, 2010.

Geomagnetic Activity	**K_p**	**JB08** [%]	**MSISE-00** [%]
Quiet	0-1	-1.2	16.6
Unsettled	2-3	1.3	15.5
Active	4	2.4	16.4
Minor Storms	5	2.4	19.5
Major Storms	6	4.1	11.9
Severe Storms	7-9	5.1	7.8

MSISE-00 generally overestimates the measured GRACE densities. In contrast, the JB08 shows a good agreement with the densities from the in-situ measurements, especially during low solar activity. However, during high activity the differences between measurements and models decrease. By comparing the correlation coefficients between the models and the measurements, it becomes

obvious that the best correlation is during low solar activity (JB08: 0.94, MSISE-00: 0.93). With increasing solar activity the correlation coefficients decrease to 0.87 and 0.80 for the JB08 and the MSISE-00 models, respectively.

As mentioned at the beginning of this section, the empirical models also provide exospheric temperatures. Thus, in order to conclude this chapter, a combination plot of neutral densities from GRACE and exospheric temperatures from the JB08 model during late October and early November in 2003 is shown in Fig. 5.3. First of all, it is obvious that a high correlation between the

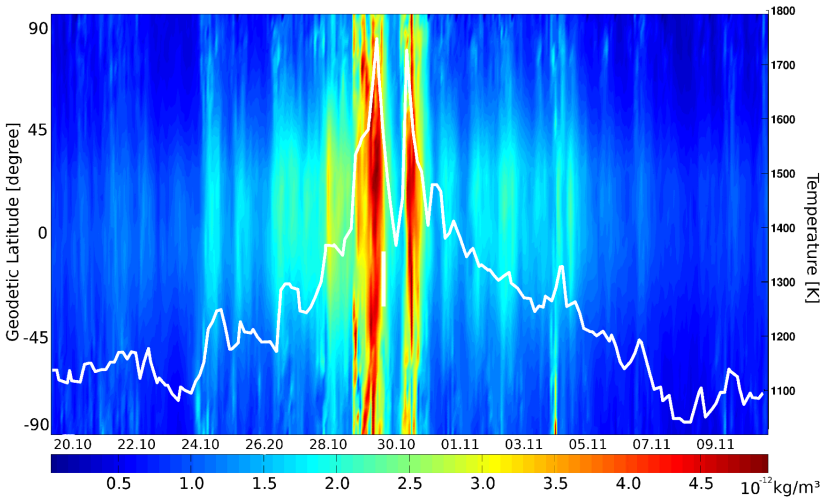

Figure 5.3: Combination plot of neutral densities from GRACE observations and exospheric temperature (white) from the JB08 model during the Halloween Period in 2003.

neutral densities and the exospheric temperatures is evident. Furthermore, it can be recognised that during these particular extreme solar events the upper atmosphere of the Earth was heated. As a result of this heating, the atmosphere expanded with a density increase at the satellite orbit [Lammer et al., 2012]. Related to that, also the exospheric temperature at the satellite position increases significantly from about 1000 K up to ∼1800 K when the CME hits the Earth's atmosphere. As for the densities, the JB08 model shows no increase in the exospheric temperatures when the gigantic X17.2 solar flare disturbed the Earth's upper atmosphere on October 28, 2003. It remains nearly constant at approximately 1350 K. This behaviour and the consequences for the present study will be discussed in the upcoming Sec. 6.

Chapter 6

Application for Atmospheric Evolution Studies

The escape and evolution of planetary atmospheres is strongly related to the evolution of the soft X-ray and EUV radiation and the particle environment of the planet's host star [Lammer et al., 2012]. Multi-wavelength observations and studies of solar analogue stars, so-called solar proxies, show that the solar flux, integrated over 0.1–120 nm, changes over time. Previous studies showed that the radiation was about 6 times higher 3.5 Gyr ago and larger than 20 times of the present Sun about 4.2 Gyr ago [Zahnle and Walker, 1982, Guedel et al., 1997, Guinan et al., 2003, Ribas et al., 2005, Guedel, 2007, Claire et al., 2012]. To illustrate this, Tab. 6.1 shows the integrated fluxes of several solar proxies of different ages in various wavelength in the EUV published in the course of the "Sun in Time" program [Ribas et al., 2005].

In the present study satellite observations from the extreme X17.2 solar flare during the Halloween period are analysed in order to verify the results from theoretical atmosphere models by Kulikov et al. [2007] and Tian et al. [2008a,b]. Since these models are mainly based on theoretical methods such a validation by observation based empirical thermosphere models (JB08), or in-situ measurements from LEO's is highly desirable. Due to the fact that GRACE is orbiting the Earth below the exobase at approximately 450 km altitude, it is predestined to be used as a diagnostic tool for retrieving thermospheric density and its variations during extreme solar events.

6.1 Theoretical Thermosphere Models of Tian and Kulikov

The region of the Earth's atmosphere where the main part of the EUV radiation is absorbed and a substantial fraction of its energy is transformed into heat extends from about 90 km to 500 km.

Table 6.1: Integrated fluxes of different solar analogues analysis in units of 10^{-7} J cm^{-2} s^{-1} [Ribas et al., 2005], in three wavelength ranges in the EUV. The stars with ages 0.1 (EK Dra), 0.3 (π^1 UMa, χ^1 Ori), 0.65 (κ^1 Cet) and 1.6 Gyr (β Com) represent well studied solar analogues with younger age (Ribas et al. [2005]), and the 4.56 Gyr old one represents the present Sun.

Wavelength range [nm]	**0.1 Gyr**	**0.3 Gyr**	**0.65 Gyr**	**1.6 Gyr**	**4.56 Gyr**
10-36	187.2	69.4	22.7	7.7	2.05
36-92	45.6	15.2	7.0	2.85	1.00
92-118	18.1	8.38	2.90	1.70	0.74

To model the influence of the solar EUV radiation on a terrestrial thermosphere and its enhanced erosion due to atmospheric loss processes during the early stages of the solar evolution, Kulikov et al. [2007] developed a hydrostatic, diffusive equilibrium and thermal balance model. They assumed present time chemical composition and included atmospheric heating by photoionisation and photodissociation processes, heating in exothermic chemical reactions, cooling by IR-radiating molecules such as CO_2, NO, and OH and heat transfer by thermal and eddy conduction. The model simulations resulted in a heated and extended terrestrial thermosphere, a condition which should have lead to a diffusion-limited atomic hydrogen blow-off and high Jeans escape [1] rates for heavier species during the first billion years after the Sun arrived at the zero-age main sequence.

However, Tian et al. [2008a,b] doubted that the thermosphere with its present chemical composition would have remained in hydrostatic equilibrium under extremely high temperatures of more than 10000 K during the first several hundred million years of the solar evolution. For this reason Tian et al. [2008a,b] developed a multi-component hydrodynamic thermosphere model to probe the Earth's thermosphere under extreme solar EUV conditions. They found that in case the EUV input is higher than approximately 5 times the present EUV flux, the hydrostatic equilibrium regime transits to a hydrodynamic regime resulting in reduced exobase temperatures and a lower Jeans loss rate of the atmosphere compared with the hydrostatic assumption (Fig. 6.1).
Nevertheless, the exosphere could have still expanded efficiently even beyond the protecting magnetopause. Thus, the early Earth with its assumed present time atmospheric composition would have been in danger of losing all of its initial N_2-inventory [Lichtenegger et al., 2010].
For a first comparison, Fig. 6.2 shows exobase temperatures obtained by the above mentioned theoretical atmosphere models for different EUV radiation levels. It can be seen that the Tian et al. [2008a] model provides throughout lower temperatures than Kulikov et al. [2007]. For a solar

[1] Jeans escape: Thermal escape, which occurs if the thermal velocity of a particle in the exobase exceeds the escape velocity.

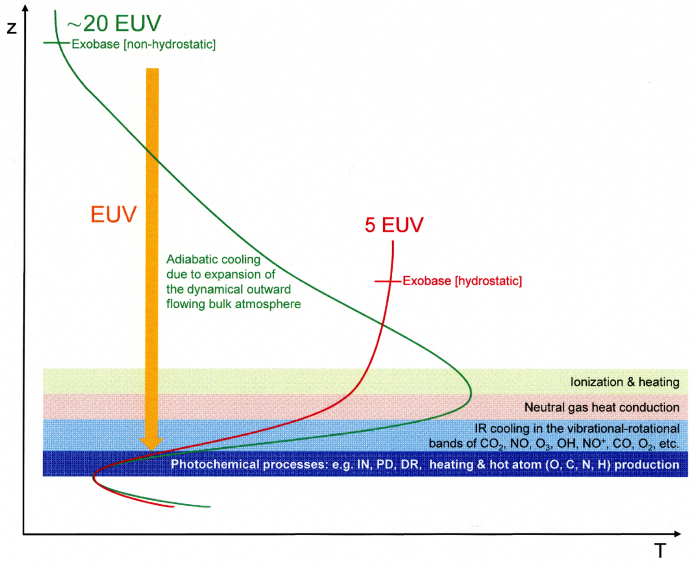

Figure 6.1: Illustration of the thermospheric temperature response to high solar/stellar EUV flux. Enhanced ionisation (IN) and photo-chemical processes like photo-dissociation (PD) and dissociative re-combination (DR) eventually lead to heating and subsequent expansion of the upper atmosphere and to the production of suprathermal atoms which may influence the energy balance in the thermosphere. Depending on atmospheric species and energy deposition, upper atmospheres can switch from hydrostatic [Kulikov et al., 2007] to hydrodynamic regimes [Tian et al., 2008a,b].

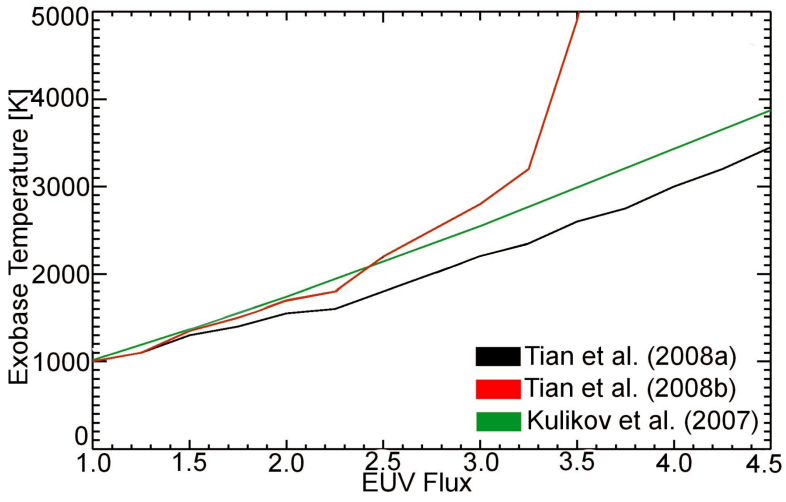

Figure 6.2: Exobase temperatures under different solar EUV conditions obtained from the theoretical models by Kulikov et al. [2007] and Tian et al. [2008a,b].

EUV flux larger than approximately 3 times its present value, the highest values are produced by the Tian et al. [2008b] due to the inclusion of an energetic electron transport model.

6.2 Estimation of the X17.2 Halloween flare radiation

As we see from Fig. 6.2, the theoretical models deliver exobase temperatures and the neutral densities depending on the intensity of the EUV radiation. Therefore, if we want to compare those results with our estimates from the JB08 and the GRACE measurements during the X17.2 flare, we must initially calculate the emitted radiation level of this specific flare. To accomplish this task, EUV measurements from TIMED/SEE (Fig. 6.3) are used.

The TIMED mission is operated by the NASA and was launched on December 7, 2001 into a low

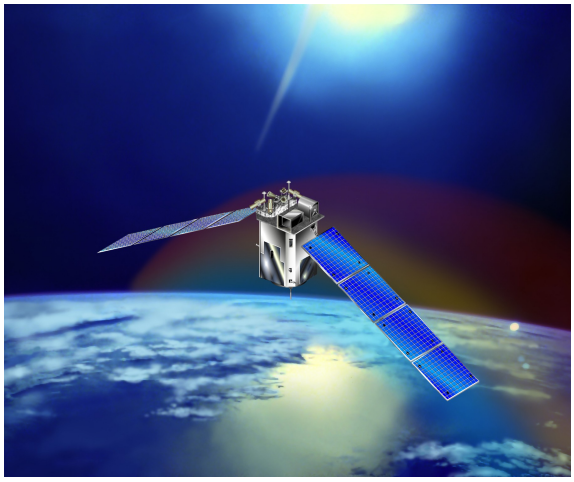

Figure 6.3: Illustration of the Thermosphere Ionosphere Mesosphere Energetics and Dynamics (TIMED) satellite. ©NASA

Earth orbit of approximately 625 km altitude. Due to several extensions of the planned mission life-time, observations over almost an entire solar cycle are presently available. The TIMED/SEE instrument determines the irradiance of the solar SXR, EUV and FUV radiation (26-194 nm). Thereby, the satellite observes the Sun approximately 12 to 15 times per day, with observations lasting about three minutes. The recorded data are provided in different processing levels to the community. For the current study, two of the provided datasets from the SEE EUV Grating Spectrograph (EGS) are used. Firstly, the SEE EGS L2 data record, which is based on daily-averaged solar spectral irradiance exempt from flares. Secondly, the SEE EGS L2A product, which contains the three minute observations including all flares events. Both datasets are available in the

netcdf-format and can be freely accessed from the mission website [1].

A comparison of the integrated flux in the EUV range (25–92 nm) during the X17.2 flare event with the EUV flux during quiet Sun conditions at moderate solar activity (E_0) shows that the flux intensity of the flare maximum (E_{flare}) was about 2.6 times higher [Fichtinger, 2011, Krauss et al., 2012]. Figure 6.4 substantiates this fact by illustrating the spectrum during the maximum of the

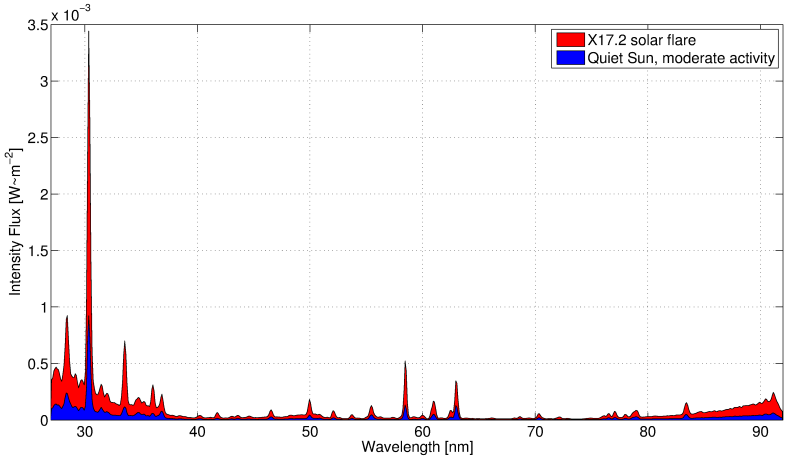

Figure 6.4: Flare spectrum in the EUV range (25–92 nm) during the maximum of the X17.2 flare on October 28, 2003 (red) and during moderate solar activity (black) on October 20, 2003 representing the quiet Sun.

Halloween flare (red) and a spectrum of the quiet Sun during moderate solar activity.

Additionally, it should be mentioned that further studies of this flare event revealed that the intensity of this specific flare event corresponds to a solar-like star at the age of ∼2.3 Gyr [Fichtinger, 2011, Krauss et al., 2012].

6.3 Comparison of Atmospheric Densities from JB08 with GRACE measurements

Based on the knowledge that the flare emitted an EUV radiation in the order of $2.6 \times E_0$, it is now possible to compare the neutral densities from the JB08 and the GRACE measurements with those from the theoretical models. Table 6.2 summarises the peak values from our former calculations (JB08, GRACE) and the estimates from the theoretical models by Tian and Kulikov. Thereby, it has to be mentioned that in Tian et al. [2008b] the neutral density is only given for $1 \times E_0$,

[1] http://lasp.colorado.edu/see/

$4\times E_0$ and $10\times E_0$. Thus, only a rough approximation of the neutral density for the flare conditions ($2.6\times E_0$) is possible.

Table 6.2: Normalised atmospheric densities calculated during the solar flare from GRACE accelerometer measurements, from the empirical model JB08 and the theoretical models from Kulikov et al. [2007] and Tian et al. [2008a,b].

Evaluation Type	**Neutral Density [10^{-12} kg m^{-3}]**
GRACE S/C	3.3
Jacchia-Bowman 2008	2.7
Kulikov 2007	8.4
Tian 2008a	23.0

Table 6.2 clearly shows that the neutral densities estimated from GRACE as well as those from the JB08 are significantly lower than those from the theoretical models, especially the Tian et al. [2008a] model. This outcome is entirely dissatisfying, however the discrepancies in both cases are explainable.

As far as GRACE is concerned, it has been already mentioned in Sec. 4.2.1 that there was no perfect overlap between the actual satellite position and the location of the flare impact. Thus, it is likely that the satellite observed a weaker thermosphere response when it returned from Earth's shadow to the planet's day-side.

In the case of the empirical thermosphere model the underestimation is even less surprising, since we have already seen in the previous sections that the applied solar indices have a low temporal resolution of one day and are used with specific lag times. Thus, the influence of the short-term solar flare is simply filtered out. A further issue which was not addressed so far is that the JB08 model also uses 81-day average values of the solar indices in order to consider long-term activities. This certainly causes inconsistencies if we compare the impact of a rather short flare irradiation with a permanent radiation of the same level ($2.6\times E_0$) emitted by a Sun at the age of about 2.3 Gyr.

To evaluate the JB08 model under such circumstances the input values for the solar indices have to be adapted. Contrary to Sec. 5.4.2 a permanent high radiation is now assumed, thus the constraint related to the lag time of the indices does no longer exist.

6.3.1 Determination of Pseudo Indices for the JB08

Since the empirical models can not reconstruct short-term perturbations originating from solar flares due to the usage of daily averaged solar indices, it is the aim to determine pseudo indices

which are intended to reflect a permanent high radiation of $2.6 \times E_0$. Based on these pseudo indices, it should be possible to estimate atmospheric densities and exospheric temperatures with the JB08 model in the same order of magnitude as the theoretical models reveal. However, it should be stressed that the usage of such pseudo indices is only valid if a certain constant radiation level is assumed. Thus, the different lag times can be neglected.

The basis of the algorithm to determine pseudo indices is a linear approximation between the averaged indices (F_{10}, S_{10}, M_{10} and Y_{10}) and the solar spectral irradiance measurements by the TIMED/SEE instrument. In general, the formalism to obtain the individual pseudo indices (I_P), which reflect the radiation of the Halloween flare (E_flare=$2.6 \times E_0$) as good as possible, can be written as

$$I_\mathrm{P} = I_0 \left(1 + k \left[\frac{E_\mathrm{flare}}{E_0} - 1 \right] \right), \tag{6.1}$$

where k denotes a scaling factor, defined as

$$k = \frac{I_\mathrm{max} - I_0}{E_\mathrm{max} - E_0} \cdot \frac{E_0}{I_0}. \tag{6.2}$$

Furthermore, both equations include mean (E_0, I_0) and maxima values ($E_\mathrm{max}, I_\mathrm{max}$) values of the EUV measurements and the various solar indices.

As mentioned in Sec. 5.2, the solar indices S_{10}, M_{10} and Y_{10} are only available since Jan. 1, 1997. Therefore, the mean and maxima values, for the 81-day average indices, are estimated between 1997 and 2008 to comprise approximately one solar cycle. Since we assume a permanent high radiation, the daily solar indices can then be equated with the 81-day averages.

In the case of the TIMED observations they do not cover a complete solar cycle, since the first data records started in 2002. Therefore, the mean and maxima are determined for the period 2002 to 2008 which is approximately half a solar cycle. The resulting numerical values for the input parameters for Eq. 6.1 and 6.2 are summarised in Tab. 6.3. Based on these numerical values we

Table 6.3: Numerical values concerning the mean and maxima of the EUV measurements and the various solar indices.

Input Parameter	Numerical Value	Source
E_0	0.0017753 [W m^{-2}]	SEE EGS L2
E_max	0.0031971 [W m^{-2}]	SEE EGS L2
E_flare	0.0046337 [W m^{-2}]	SEE EGS L2A
F_0 | F_max	120.2 | 226.7 [sfu]	JB08 database
S_0 | S_max	111.0 | 213.3 [sfu]	JB08 database
M_0 | M_max	118.8 | 214.4 [sfu]	JB08 database
Y_0 | Y_max	117.9 | 180.2 [sfu]	JB08 database

can evaluate Eq. 6.1 and 6.2 to obtain the desired pseudo indices which reflect the radiation of the Halloween flare (Tab. 6.4).

Table 6.4: Calculated pseudo indices which reflect the X17.2 solar flare on October 28 in 2003.

Pseudo Indices	Numerical Value [sfu]
F_{flare}	333.0
S_{flare}	315.4
M_{flare}	309.8
Y_{flare}	242.4

A re-evaluation of the JB08 model with the pseudo-indices of Tab. 6.4 yields a total mass density of 2.0829×10^{-11} kg m^{-3} and an exobase temperature of 1987.5 K. These results agree significantly better with those from the theoretical models than the previous ones, based on the regular, averaged solar indices (Tab. 6.2). The best agreement arises with the estimates from Tian et al. [2008a] which predicts a neutral density of 2.3×10^{-11} kg m^{-3} for $2.6 \times E_0$.

6.3.2 X2.0 Solar Flare on November 07, 2004

In case of the Halloween flare it was not possible to make a meaningful comparison between the neutral densities from GRACE and those from the theoretical models because the satellite measured a lower impact due to its improper position in space. In order to accomplish this task, a solar flare where the satellite had a better position to record the impact of the flare without a long time delay would be desirable.

However, the search for a suitable solar flare proved more difficulties than expected. The first limiting factor is that huge X-class flares mostly occur during high solar activity. Regarding the current investigation period (2003–2010) this means that only the first 3.5 years are of interest. The closer we come to the solar minimum, the smaller the solar flares and thus the impact on the S/C. Secondly, the solar flare must be directed towards the Earth, otherwise we will not observe any impact on the satellite. Another problem which arises is that the requested flare may not be superimposed by the impact of a CME, like it was the case with the X10 flare on October 29 in 2003 (Sec. 4.2.1). And last but not least, a suitable location of the GRACE satellite during the eruption is also quite rare.

A solar flare which mostly fulfilled the expectations occurred on November 07, 2004 at 15:24 UT with a peak intensity 42 minutes later. The first recorded impact on the GRACE satellites occurred at ∼16:15 UT. Thus, the measured densities should be nearly equal to those from the theoretical models and to those from the JB08 model - if pseudo indices are applied. This means that this flare offers the possibility to validate the previously described pseudo index determination process. An illustration of the atmospheric density variations during this period is shown in Fig. 6.5. As

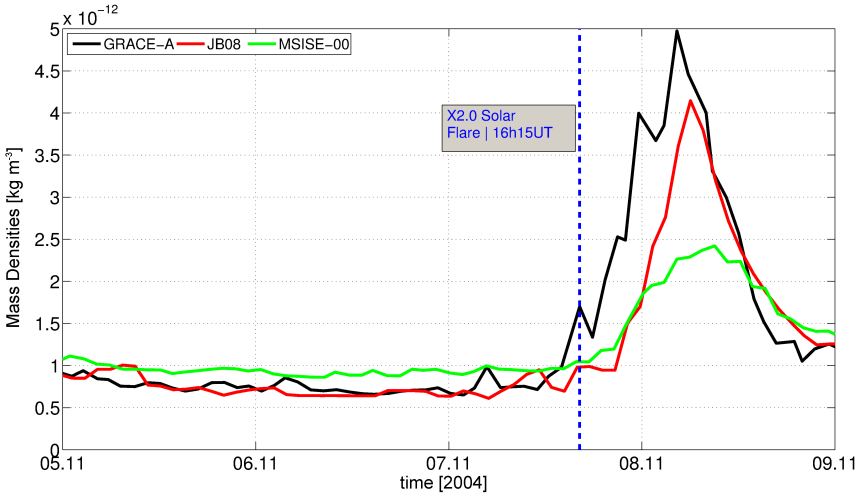

Figure 6.5: Atmospheric densities from GRACE and the empirical thermosphere models JB08 and MSISE-00 during the X2.0 flare on November 7, 2004.

expected, both empirical models are not able to model the impact of the solar flare and yield significantly lower values than GRACE (1.83×10^{-12} kg m^{-3}). Additionally, it is astonishing to see that the MSISE-00 model significantly underestimates the impact of the following CME on November 8, originating from three M-class flares occurred on November 6, in 2004. As Burke et al. [2007] stated, this underestimation might originate from the fact that ground magnetometers are primarily sensitive to ionospheric Hall currents, resulting in an underestimation of thermospheric energy budgets during geomagnetic storms.

According to the algorithm described above, the first step in the calculation process of the pseudo indices is the determination of the intensity of the solar flare by using satellite observations from TIMED/SEE. Unfortunately, there are no TIMED measurements from the X2.0 flare available. For this reason a different method was used to obtain a rough estimation of the flare intensity.

In Sec. 4.3 it was mentioned that the $S_{10.7}$ index is derived from satellite observations by SOHO with a sampling rate of 15 seconds. Based on a daily average of these high-rate observations, the

regular $S_{10.7}$ solar index can be calculated following Tobiska et al. [2008a]

$$S_{10.7} = -12.01 + 141.23 \times (\text{SOHO SEM}_{26-34}/1.9955 \times 10^{10}). \tag{6.3}$$

Here, SOHO SEM_{26-34} indicates the daily averaged EUV measurements in the wavelengths between 26 and 34 nm. The idea is to evaluate Eq. 6.3 using directly the high-rate observations during the flare event, instead of a daily average. The resulting $S_{10.7}$ index should then be in the same order as a $S_{10.7}$ pseudo index. Afterwards it would be possible to get an estimate of the intensity of the flare by inserting this $S_{10.7}$ in Eq. 6.1.

In order to verify this assumption, such a high-rate index will be initially determined for the Halloween event. This has the advantage that it is possible to compare the calculated value with the previously determined pseudo index. As stated in Sec. 2.1.4, the peak intensity of the X17.2 Halloween occurred at approximately 11:10 UT. At this time the SOHO/SEM[1] measured a flux of 4.593×10^{10}photons cm^{-2} s^{-1} at 1 AU. Inserting this value in Eq. 6.3 yields a high-rate $S_{10.7}$ of 313.08 sfu, which is only slightly lower than the determined pseudo index of 315.4 sfu.

In view of this good agreement the calculation of a high-rate $S_{10.7}$ for the X2.0 solar flare appears to be justified. For this event the SOHO/SEM instrument reveals a flux of 2.006×10^{10}photons cm^{-2} s^{-1} at 1 AU, resulting in a high-rate $S_{10.7}$ equal to 130.0 sfu. By evaluating Eq. 6.1 and 6.2 we obtain a peak intensity of the X2.0 flare in the order of about $1.15 \times E_0$. With this information, it is possibly to calculate the pseudo values for the three remaining solar indices F_{10}, M_{10} and Y_{10}. Table 6.5 summarises the resulting quantities.

Table 6.5: Calculated pseudo indices, which reflects the X2.0 solar flare on November 07, 2004.

Pseudo Indices	Numerical Values
E_{flare}	0.002039 [W m^{-2}]
F_{flare}	140.0 [sfu]
S_{flare}	130.0 [sfu]
M_{flare}	136.6 [sfu]
Y_{flare}	129.5 [sfu]

By using these pseudo indices within the JB08 model yields an atmospheric density in the order of 1.70×10^{-12} kg m^{-3} which is in good agreement with the observed value of 1.83×10^{-12} kg m^{-3} by GRACE. Concerning the exospheric temperature the JB08 delivers a value of 1168 K.

[1] http://www.usc.edu/dept/space_science/semdatafolder/semdownload.htm

In summary it can be stated that the algorithm for the calculation of the pseudo indices seems to be stable and that the usage of these indices within the JB08 model permits a meaningful comparison between empirical and theoretical atmosphere models. Regarding the real measurements from GRACE it has been shown that if the S/C is in a suitable orbit position the observations can be used to directly extract information concerning the influence of a solar flare event on the upper Earth's atmosphere.

6.4 Comparison assuming different EUV conditions

In Fig. 6.2 the exobase temperatures from the theoretical models were illustrated for different solar EUV conditions. Since the JB08 model also provides exospheric temperatures and the preceding comparisons between neutral densities from the theoretical models and the JB08 model were in good agreement, when using pseudo indices, we compute further pseudo indices for different solar EUV conditions and evaluate the JB08 model for a final validation. Figure 6.6 illustrates the resulting exobase temperatures for increasing EUV fluxes, estimated with the empirical JB08 model and the theoretical models [Kulikov et al., 2007, Tian et al., 2008a,b]. It can be seen that

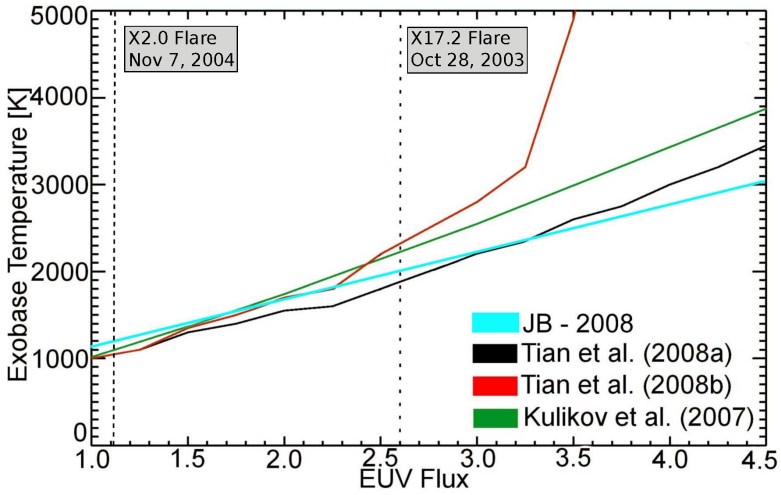

Figure 6.6: Exobase temperatures obtained from the empirical thermosphere model JB08 and the theoretical models of Kulikov et al. [2007] and Tian et al. [2008a,b] under different solar EUV conditions. The vertical dotted line corresponds to the $2.6 \times E_0$ enhancement inferred from the X17.2 Halloween flare on October 28, 2003.

the empirical JB08 model agrees very well with the results from the theoretical models for the moderate present time solar EUV conditions when the exobase is located at about 500 km with a temperature of ~1000 K. While the theoretical model of Kulikov et al. [2007] yields slightly higher

exobase temperatures for $2.6 \times E_0$, the theoretical model of Tian et al. [2008a] agrees also quite well with the JB08 model at higher EUV fluxes. In the case of a lower EUV radiation such as those emitted by the analysed X2.0 solar flare ($1.15 \times E_0$) all models are in good agreement to each other.

In summary it can be stated, that if we take into account the properties of the solar indices, it is indeed possible to validate the theoretical atmosphere models with an observation based empirical model like JB08 or directly with LEO observations implying a suitable orbit position of the S/C.

Chapter 7

Summary and Outlook

This thesis is an interdisciplinary study in the field of astronomy and geodesy that focuses on the response of the upper Earth's atmosphere during different of solar activity levels. By analysing satellite drag data from the LEO mission GRACE over 7.5 years and comparing them with the empirical thermosphere models MSISE-00 and JB08, the study indicates that the JB08 model reproduces the total mass density from GRACE significantly better than the MSISE-00 model - regardless of the solar activity level.

Additionally, the effect of the EUV radiation during an extreme X17.2 flare event on the Earth's thermosphere was investigated. This flare was a more or less isolated phenomenon which could be thoroughly separated from the CME-related particle events that occurred the day after. From the analysis of the peak EUV increase during the X17.2 flare it was found that both empirical models can not resolve the density and temperature enhancements in the thermosphere compared with the observed data. This can be related to the fact that the empirical models use daily average solar activity indices and thus are not capable to model the short-term perturbations originated from a solar flare that lasted about 90 minutes.

Concerning the in-situ measurements from the GRACE satellite during the Halloween event, is has been shown that the S/C was at the nightside of the planet when the flare occurred. This implies that the satellite observed only an aftermath of the flare impact on the thermosphere when it returned to the dayside. It is supposed that GRACE would have recorded a notably stronger density increase if it had been on the dayside at the time when the flare occurred. In that case the actual differences between the observed densities and the values calculated from the empirical models would have been even larger.

By analysing the EUV measurements from the TIMED/SEE instrument it has been found that the peak intensity flux of the X17.2 solar flare is approximately 2.6 times the intensity of

the quiet Sun during moderate solar activity. Assuming that the Sun permanently emitted an EUV flux of this magnitude, pseudo solar activity indices were calculated. A re-evaluation of the JB08 model yielded an average exobase temperature of ∼1988 K. This value agrees well with the exobase temperatures from the theoretical models [Kulikov et al., 2007, Tian et al., 2008a,b] in case similar EUV flux values are applied. Thus, the agreement between the theoretical models and the empirical JB08 model validates the results for EUV fluxes $\leq 2.6 \times EUV_0$. Hence, if we assume an atmospheric composition similar to that of the present Earth, the thesis verifies the results from Tian et al. [2008a, p. 14, Fig.8a,c], that the exosphere assuming $\sim 2.6 \times EUV_0$, was approximately twice as hot as today (∼2000 K).

Beside the analysis of the X17.2 Halloween flare, an additional X2.0 flare, that occurred on November 7, 2004 has been investigated. In contrast to the X17.2 flare, this event had the advantage that GRACE recorded the perturbations caused by this flare without a large time delay. Thus, the atmospheric densities from GRACE are directly comparable to the theoretical model densities and can be used to verify the algorithm for the computation of pseudo indices. It is apparent that the algorithm provides adequate results and that the intensity of the X2.0 solar flare corresponds to $\sim 1.15 \times EUV_0$. Therefore, the thesis has shown that the results of the theoretical models are realistic and that in-situ measurements from LEO satellites during extreme solar events are suitable to validate and improve theoretical models. However, it has also been emphasised that the number of suitable solar flare events is rather small due to several necessary prerequisites. These include the intensity of the flare which is correlated with the solar activity level, the position of the satellite, the direction of the solar flare and the influence of other disturbance sources like CMEs. Due to these restrictions it will be important to analyse additional solar events which fulfil the mentioned requirements in the future to further enhance our understanding of the evolution of planetary atmospheres.

Additionally, the JB08 model was evaluated assuming different high EUV flux levels, which are emitted by the early Sun at different ages. The difference between the various models concerning the exobase temperatures at EUV fluxes higher than approximately three times than today, characterises the current level of uncertainties inherent in the models. This is due to the insufficient understanding of the main processes that determine the energy balance of an N_2-rich terrestrial thermosphere exposed to extremely high EUV radiation of the early Sun.

Furthermore, it was interesting to observe that CMEs may cause stronger density enhancements in the thermosphere than the analysed EUV radiation by the flare. The thesis indicates that energetic particle events may have even a stronger impact than the EUV radiation on the evolution

of the early solar system planets or terrestrial exoplanets orbiting active young stars [Zaqarashvili et al., 2011, Khodachenko et al., 2007].

Since the impacts of CMEs affect not only the Earth's upper atmosphere but also the Earth's magnetic field the upcoming ESA mission SWARM[1] (launch: March 2013) might be of interest for future studies. This LEO mission will consist of three S/C and has the main objective to measure magnetic signals stemming from Earth's core, mantle, crust, oceans, ionosphere, and magnetosphere. Each of the three satellites will be equipped with accelerometers. As a consequence, the mission offers a great possibility to examine the response of the thermosphere and the Earth's magnetic field to extreme CMEs more closely.

[1] http://www.esa.int/esaLP/LPswarm.html

References

F. Barlier, C. Berger, J.L. Falin, G. Kockarts, and G. Thuillier. A thermospheric model based on satellite drag data. *Annales Geophysicae*, 34(1):9–24, 1978. 70

J. Bartels, N.H. Heck, and H.F. Johnston. The three -hour-range index measuring geomagnetic activity. *Journal of Geophysical Research*, 44(4):411–454, 1939. URL Bartels1939. 59

W. Baumjohann and R.A. Treumann. *Basic Space Plasma Physics*. Imperial College Press, revised ed edition, 2012. ISBN 13 978-1-84816-894-7. 9, 12

C. Berger, R. Biancale, and F. Barlier. Improvement of the empirical thermospheric model DTM: DTM94 – a comparative review of various temporal variations and prospects in space geodesy applications. *Journal of Geodesy*, 72(3):161–178, 1998. 70

S. Bettadpur. GRACE 327-720 (CSR-GR-03-02) Gravity Recovery and Climate Experiment Product Specification Document. Technical report, Center of Space Research, 2007. xix, 22, 25

S. Bettadpur. Recommendation for a-priori Bias & Scale Parameters for Level-1B ACC Data (Version 2). pages 1–2, 2009. xiv, xix, 28, 29, 31

A. Bhatnagar and W. Livingston. *Fundamentals of Solar Astronomy*. World Scientific Publishing Co. Pte. Ltd., 2005. ISBN 981-238-244-5. xix, 10

B.R. Bowman, K.W. Tobiska, F. Marcos, and C. Valladares. The JB2006 empirical thermospheric density model. *Journal of Atmospheric and Solar-Terrestrial Physics*, 70(5):774–793, 2007. ISSN 13646826. doi: 10.1016/j.jastp.2007.10.002. 70

B.R. Bowman, W.K. Tobiska, F.A. Marcos, C.Y. Huang, C.S. Lin, and William J Burke. A New Empirical Thermospheric Density Model JB2008 Using New Solar and Geomagnetic Indices. *AIAA 2008-6438, AIAA/AAS Astrodynamics Specialist Conference*, (August), 2008. 1, 63, 65, 72, 75

S. Bruinsma and J.M. Forbes. Solar flux variability and MARS thermosphere densities derived from orbital tracking data. *Earth*, pages 1–4, 2003. 43, 51

S. Bruinsma and J.M. Forbes. Properties of traveling atmospheric disturbances inferred from CHAMP accelerometer observations. *Advances in Space Research*, page 9, 2008. doi: 10.1016/j.asr.2008.10.031. 57

S. Bruinsma, G. Thuillier, and F. Barlier. The DTM-2000 empirical thermosphere model with new data assimilation and constraints at lower boundary: accuracy and properties. *Journal of Atmospheric and Solar-Terrestrial Physics*, 65(9):1053–1070, June 2003. ISSN 13646826. doi: 10.1016/S1364-6826(03)00137-8. URL http://linkinghub.elsevier.com/retrieve/pii/S1364682603001378. 70

S. Bruinsma, D. Tamagnan, and R. Biancale. Atmospheric densities derived from CHAMP/STAR accelerometer observations, Plan. *Planet*, 52:297–312, 2004. 51

S. Bruinsma, J.M. Forbes, R.S. Nerem, and X. Zhang. Thermosphere density response to the 20–21 November 2003 solar and geomagnetic storm from CHAMP and GRACE accelerometer data. *Journal of Geophysical Research*, 111(A6):1–14, 2006. ISSN 0148-0227. doi: 10.1029/2005JA011284. 1, 53

S. Bruinsma, R. Biancale, and F. Perosanz. Calibration parameters of the CHAMP and GRACE accelerometers. In *IUGG XXIV General Assembly*, Perugia, 2007. ISBN 3550935389284. xix, 30, 31, 51

S. Bruinsma, N. Sánchez-Ortiz, E. Olmedo, and N. Guijarro. Evaluation of the DTM-2009 thermosphere model for benchmarking purposes. *Journal of Space Weather and Space Climate*, 2(A04):14, June 2012. ISSN 2115-7251. doi: 10.1051/swsc/2012005. URL http://www.swsc-journal.org/10.1051/swsc/2012005. 70, 73

W. J. Burke, C.Y. Huang, F. Marcos, and J.O. Wise. Interplanetary control of thermospheric densities during large magnetic storms. *Journal of Atmospheric and Solar-Terrestrial Physics*, 69(3):279–287, March 2007. ISSN 13646826. doi: 10.1016/j.jastp.2006.05.027. 87

K. Case, G. Kruizinga, and S.C. Wu. GRACE Level 1B Data Product User Handbook. Technical report, Jet Propulsion Laboratory, California Institute of Technology, 2010. 22

REFERENCES

M.W. Claire, J. Sheets, M. Cohen, I. Ribas, V.S. Meadows, and D.C. Catling. THE EVOLUTION OF SOLAR FLUX FROM 0.1 nm TO 160 μm: QUANTITATIVE ESTIMATES FOR PLANETARY STUDIES. *The Astrophysical Journal*, 757(1):95, September 2012. ISSN 0004-637X. doi: 10.1088/0004-637X/757/1/95. URL http://stacks.iop.org/0004-637X/757/i=1/a=95?key=crossref.d1f0533cd0d7024957183609ca9b0ae3. 1, 79

National Research Council Committee on Solar and Space Physics. *Plasma Physics of the Local Cosmos*. The National Academies Press, 2004. ISBN 0309532159. URL http://www.nap.edu/openbook.php?record_id=10993. xiii, 13

G.E. Cook. The Aerodynamic Drag of Near Earth Satellites 3. Technical report, 1960. 2, 39, 40

G.E. Cook. Satellite drag coefficients. *Planetary and Space Science*, 13(10):929–946, October 1965. ISSN 00320633. doi: 10.1016/0032-0633(65)90150-9. 2, 39

E. Doornbos, M. Förster, B. Fritsche, T.V. Helleputte, J.V.D. Ijssel, G. Koppenwallner, H. Lühr, D. Rees, and P. Visser. Air density models derived from multi-satellite drag observations. Technical Report May, DEOS TU Delft, 2009. 1, 52

M.R. Drinkwater, R. Floberghagen, R. Haagmans, D. Muzi, and A. Popescu. GOCE: ESA's first Earth Explorer Core mission. In G.B. Beutler, M.R. Drinkwater, R. Rummel, and R. von Steiger, editors, *Earth Gravity Field from Space - from Sensors to Earth Sciences*, volume 18, pages 419–432. Kluwer Academic Publishers, Dordrecht, space scie edition, 2003. ISBN 1402014082. 19

D.P. Drob, J.T. Emmert, G. Crowley, J.M. Picone, G.G. Shepherd, W. Skinner, P. Hays, R.J. Niciejewski, M. Larsen, C. Y. She, J. W. Meriwether, G. Hernandez, M.J. Jarvis, D.P. Sipler, C.A. Tepley, M.S. O'Brien, J.R. Bowman, Q. Wu, Y. Murayama, S. Kawamura, I.M. Reid, and R.A. Vincent. An empirical model of the Earth's horizontal wind fields: HWM07. *Journal of Geophysical Research*, 113(A12):1–18, December 2008. ISSN 0148-0227. doi: 10.1029/2008JA013668. URL http://www.agu.org/pubs/crossref/2008/2008JA013668.shtml. xv, 46, 47

J.T. Emmert, D.P. Drob, G.G. Shepherd, G. Hernandez, M.J. Jarvis, J.W. Meriwether, R.J. Niciejewski, D.P. Sipler, and C.A. Tepley. DWM07 global empirical model of upper thermospheric storm-induced disturbance winds. *Journal of Geophysical Research*, 113(A11):1–16, November 2008. ISSN 0148-0227. doi: 10.1029/2008JA013541. URL http://www.agu.org/pubs/crossref/2008/2008JA013541.shtml. 46

ESA. The four Candidate Earth Explorer Core Missions - Gravity Field and Steady-State Ocean Circulation Mission. ESA SP-1233. Technical Report July, 1999. 21

B. Fichtinger. *Using extreme solar events as proxy for the active young Sun: Implications for planetary atmosphere evolution*. PhD thesis, University of Graz, 2011. 83

C. Foerste, F. Flechtner, R. Schmidt, U. Meyer, R. Stubenvoll, M. Rothacher, F. Barthelmes, H. Neumayer, R. Biancale, S. Bruinsma, J.M. Lemoine, and S. Loyer. Global Mean Gravity Field Models from Combination of Satellite Mission and Altimetry/Gravimetry Surface Data, 2006. 30

J.M. Forbes. Dynamics of the Thermosphere. *Journal of the Meteorological Society of Japan*, 85B:193–213, 2007. ISSN 0026-1165. doi: 10.2151/jmsj.85B.193. 15

J.E. Frederick, R.P. Cebula, and D.F. Heath. Instrument characterization for the detection of long-term changes in stratospheric ozone: An analysis of the SBUV/2 radiometer. *Journal of Atmospheric and Oceanic Technology*, 3:472–480, 1986. 65

M. Guedel. The Sun in Time: Activity and Environment. *Living Reviews in solar Physics*, 4(3), 2007. 1, 79

M. Guedel, E.F. Guinan, and S.L. Skinner. The X-Ray Sun in Time: A Study of the Long-Term Evolution of Coronae of Solar -Type Stars. *Astrophysical Journal*, 483:947, 1997. 1, 79

E.F. Guinan, I. Ribas, and G.M. Harper. Far-Ultraviolet Emissions of the sun in Time: Probing Solar Magnetic Activity and Effects on Evolution of Paleoplanetary Atmospheres. *Astrophysical Journal*, 594:561–572, 2003. 1, 79

W.A. Gustafson. The newtonian diffuse method for computing aerodynamic forces. Technical report, Missiles and Space Division, Lockheed Aircraft Corporation, Sunnyvale, California, 1958. 2, 39

W.R. Hamilton. On Quaternions; or on a new System of Imaginaries in Algebra (letter to John T. Graves, dated October 17, 1843), 1843. 25

A. Hanslmeier. *The sun and space weather*. Kluwer Academic Publisher, 2002. ISBN 1-4020-0684-5. 3, 7, 9, 10

A.E. Hedin. High Altitude Modeling Atmospheric. NASA Technical Memorandum 100707. Technical report, NASA, Greenbelt, Maryland, 1988. 70

A.E. Hedin, H.G. Mayr, C.A. Reber, G.R. Carignan, and N.W. Spencer. A global empirical model of thermospherc composition based on OGO-6 mass spectrometer measurements. Technical report, Goddard Space Flight Center, Greenbelt, Maryland, 1972. 69

A.E. Hedin, B.B. Hinton, and G.A. Schmitt. Role of Gas-Surface Interactions in the Reduction of Ogo 6 Neutral Particle Mass Spectrometer Data. *Journal of Geophysical Research*, 78(22):4651–4668, 1973. 42

M.P. Hickey. The NASA Marshall Engineering Thermosphere Model. Technical report, Universities Space Research Association, Huntsville, Alabama 35806, 1988. 69

B. Hoffmann-Wellenhof, H. Lichtenegger, and J. Collins. *GPS Theory and Practice*. SpringerWienNewYork, 5th edition, 2001. 24

C.Y. Huang and W.J. Burke. Transient sheets of field-aligned current observed by DMSP during the main phase of a magnetic superstorm. *Journal of Geophysical Research*, 109, 2004. doi: 10.1029/2003JA010067. 62

L.G. Jacchia. Astrophysical Observatory. *Smithsonian contributions to astrophysics*, 8(9):52, 1965. 69

L.G. Jacchia. New static models of the thermosphere and exosphere with empirical temeprature profiles. Technical report, Smithsonian Astrophysical Observatory, 1970. 69, 70

L.G. Jacchia. Revised statistic models of the thermosphere and exosphere with empirical temperature profiles. Special Report 332. Technical report, Smithsonian Astrophysical Observatory, 1971. 69

L.G. Jacchia. Atmospheric Models in the Region from 110 to 2000 km. In: CIRA 1972: COSPAR International Reference Atmosphere. Technical report, 1972. 72

L.G. Jacchia. Thermospheric temperature, density and composition: New models. Technical report, Smithsonian Institute, Astrophysical Observatory, Cambridge, Massachusetts, 1977. 69

Z. Kang, B. Tapley, S. Bettadpur, J. Ries, and P. Nagel. Precise orbit determination for GRACE using accelerometer data. *Advances in Space Research*, 38(9):2131–2136, January 2006. ISSN 02731177. doi: 10.1016/j.asr.2006.02.021. URL http://linkinghub.elsevier.com/retrieve/pii/S0273117706000755. 51

M.L. Khodachenko, I. Ribas, H. Lammer, J.M. Grieß meier, M. Leitner, F. Selsis, C. Eiroa, A. Hanslmeier, H.K. Biernat, C.J. Farrugia, and H.O. Rucker. Coronal mass ejection activity of low mass M stars as an important factor for the habitability of terrestrial exoplanets. I. CME impact on expected magnetospheres of Earth-line exoplanets in close-in habitable zones. *Astrobiology*, 129:207–243, 2007. 93

G. Koppenwallner. Comment on Special Section: New Perspectives on the Satellite Drag Environments of Earth, Mars, and Venus. *Journal of Spacecraft and Rockets*, 45(6):1324–1327, 2008. ISSN 0022-4650. doi: 10.2514/1.37539. 42

H. J. Kramer. *Observation of the Earth and Its Environment*. Springer, 4th edition, 2002. ISBN 978-3-540-42388-1. xix, 20

S. Krauss, A. Maier, and G. Stangl. Regional Ionosphere Models for Improving GNSS Navigation. *Österreichische Zeitschrift für Vermessung und Geoinformation*, 02(99):131–137, 2011. 17

S. Krauss, B. Fichtinger, H. Lammer, W. Hausleitner, I. Ribas, V.I. Shematovich, D. Bisikalo, T.V. Zaqarashvili, M.L. Khodachenko, and A. Hanslmeier. Solar flares as proxy for the young Sun: Satellite observed thermosphere response to an X17.2 flare of Earth's upper atmosphere. *Annales Geophysicae*, 30:1129–1141, 2012. doi: 10.5194/angeo-30-1129-2012. 12, 83

Y.N. Kulikov, H. Lammer, H.I.M. Lichtenegger, T. Penz, D. Breuer, T. Spohn, T. Lundin, and H.K. Biernat. A comparative study of the influence of the active young sun on the early Earth Atmospheres of Earth, Venus and Mars. *Space Science Reviews*, 129:207–243, 2007. xvii, xx, 1, 2, 79, 80, 81, 84, 89, 92

P. Kurzweil, B. Frenzel, and F. Gebhard. *Physik Formelsammlung*. Vieweg+Teubner, Wiesbaden, 2nd edition, 2009. ISBN 978-3-8348-0875-2. 45

H. Lammer, M. Güdel, Y. Kulikov, I. Ribas, T.V. Zaqarashvili, M.L. Khodachenko, K.G. Kislyakova, H. Gröller, P. Odert, M. Leitzinger, B. Fichtinger,

REFERENCES

S. Krauss, W. Hausleitner, M. Holmström, J. Sanz-Forcada, H. Lichtenegger, A. Hanslmeier, V.I. Shematovich, D. Bisikalo, H. Rauer, and M. Fridlund. Variability of solar/stellar activity and magnetic field and its influence on planetary atmosphere evolution. *Earth Planets Space*, 63:1–21, 2012. doi: 10.5047/eps.2011.04.002. 1, 77, 79

H.I.M. Lichtenegger, H. Lammer, J.M. Griemeier, Y.N. Kulikov, P. von Paris, W. Hausleitner, S. Krauss, and H. Rauer. Aeronomical evidence for higher CO2 levels during Earth's Hadean Epoch. *Icarus*, 210(1): 1–7, 2010. 80

J. Lilensten, editor. *Space Weather*. Springer, 344 edition, 2007. ISBN 1-4020-5445-9. 11

F. Lyard, F. Lefevre, T. Letellier, and O. Francis. Modelling the global ocean tides: modern insights from FES2004. *Ocean Dynamics*, 56 (5-6):394–415, September 2006. ISSN 1616-7341. doi: 10.1007/s10236-006-0086-x. URL http://www.springerlink.com/index/10.1007/s10236-006-0086-x. 30

J.A. Marusek. Solar Storm Threat Analysis. *Impact*, pages 1–29, 2007. 18

D.D. McCarthy and G. Petit. IERS Conventions (2003). Technical report, 2004. 25

M. Menvielle, N. Papitashvili, L. Haekkinen, and C. Sucksdorff. Computer production of K indices: review and comparison of methods. *Geophysical Journal International*, 123:866–886, 1995. 62

K. Moe and B.R. Bowman. The Effects of Surface Composition and Treatment On Drag Coefficients of Spherical Satellites. In *AAS/AIAA Astrodynamics Specialists Conference*, page 17, Lake Tahoe, California, 2005. AAS Publications Office, P.O. Box 28130. 40, 42

K. Moe and M.M. Moe. Gas–surface interactions and satellite drag coefficients. *Planetary and Space Science*, 53(8):793–801, July 2005. ISSN 00320633. doi: 10.1016/j.pss.2005.03.005. 2, 40, 42, 44

M.M. Moe and K. Moe. The roles of kinetic theory and gas-surface interactions in measurements of upper-atmospheric density . *Planetary and Space Science*, 17(5):917–922, May 1969. ISSN 00320633. doi: 10.1016/0032-0633(69)90097-X. 42

M. Moldwin. *An Introduction to Space Weather*. Cambridge University Press, Cambridge, 2008. ISBN ISBN 978-0-521-71112-8. 3, 4, 5, 11, 15, 18

O. Montenbruck and E. Gill. *Satellite Orbits Model Methods Applications*. Springer-Verlag Berlin Heidelberg, 2nd edition, 2001. ISBN 354067280. 25, 33

NASA. Earth Science Reference Handbook 2006, 2006. 21, 23, 27

J.K. Owens. NASA Marshall Engineering Thermosphere Model-Version 2.0. Technical report, Marshall Space Flight Center, Alabama, 2002. 69

C. Pardini, L. Anselmo, K. Moe, and M.M. Moe. Drag and energy accommodation coefficients during sunspot maximum. *Advances in Space Research*, 45(5):638–650, March 2010. ISSN 02731177. doi: 10.1016/j.asr.2009.08.034. URL http://linkinghub.elsevier.com/retrieve/pii/S0273117709006188. 42

J.M. Picone, D.P. Drob, R.R. Meier, and A.E. Hedin. NRLMSISE-00: A New Empirical Model of the Atmosphere, 2003. 1, 70, 71

G.W. Proelss. *Physik des erdnahen Weltraums*. Springer, 2001. ISBN 3-540-42052-5. xiv, 15, 41

D. Rees. WP4300: Comparison of Satellite data from GRACE and CHAMP with Empirical and Physical Models of Thermospheric Wind and Density. Technical report, November 2008. URL http://www.ncbi.nlm.nih.gov/pubmed/21752794. 48

C. Reigber, H. Luehr, and P. Schwintzer. CHAMP Mission Status. *Advances in Space Research*, 30(2): 129–134, 2002. 19

I. Ribas, E.F. Guinan, M. Guedel, and M. Audard. Evolution of the Solar Activity over Time and Effects on Planetary Atmospheres. I. High-Eergy Irradiances (1-1700 A). *Astrophysical Journal*, 622: 680–694, 2005. xx, 1, 79, 80

C. Sakulin. *Gravity field recovery: Applying the energy integral approach to CHAMP POD & accelerometry data*. Master thesis, Technical University of Graz, 2004. 25

R. Schamberg. Analytic Representation of Surface Interaction for Free Molecular Flow with Application to Drag of Various Bodies, 1959. 2, 39

L. Sentman. Free molecule flow theory and its application to the determination of aerodynamic forces. 1961. 2, 39, 41, 43

J.A. Storch. Aerodynamic Disturbances on Spacecraft in Free-Molecular Flow. Technical Report 3397, Space and Missile Systems Center Air Force Space Command, Los Angeles, 2003. 41

E.K. Sutton. *Effects of Solar Disturbances on the Thermosphere Densities and Winds from CHAMP and GRACE Satellite Accelerometer Data*. PhD thesis, University of Colorado, 2008. xix, 1, 33

E.K. Sutton, R.S. Nerem, and J.M. Forbes. Density and Winds in the Thermosphere Deduced from Accelerometer Data. *Journal of Spacecraft and Rockets, Vol. 44, No.*, 6:102514/128641, 2007. 33

E.K Sutton, R.S. Nerem, and J.M. Forbes. Technical Comments to Koppenwallner. *Journal of Spacecraft and Rockets*, 45(6):2, 2008. doi: 10.2514/1.39556. 52

B.D. Tapley, J.C. Ries, S. Bettadpur, and M. Cheng. Neutral Density Measurements from Gravity Recovery and Climate Experiment Accelerometers. *Journal of Spacecraft and Rockets*, 44(6):102514/128843, 2007. doi: 10.2514/1.28843. 1

K.F. Tapping and D.P. Charrois. Limits to the Accuracy of the 10.7cm Flux. *Solar Physics*, 150:305–315, 1994. 64

F. Tian, J.F. Kasting, H. Liu, and R.G. Roble. Hydrodynamic planetary thermosphere model: 1. Response of the Earth's thermosphere to extreme solar EUV conditions and the significance of adiabatic cooling. *Journal of Geophysical Research*, 113(E5), May 2008a. ISSN 0148-0227. doi: 10.1029/2007JE002946. xvii, xx, 1, 2, 79, 80, 81, 84, 86, 89, 90, 92

F. Tian, S.C. Solomon, L. Qian, J. Lei, and R.G. Roble. Hydrodynamic planetary thermosphere model: 2. Coupling of an electron transport/energy deposition model. *Journal of Geophysical Research*, 113(E7): 1–29, July 2008b. ISSN 0148-0227. doi: 10.1029/2007JE003043. xvii, xx, 1, 2, 79, 80, 81, 82, 83, 84, 89, 92

W.K. Tobiska, S. Bouwer, and B.R. Bowman. The development of new solar indices for use in thermospheric density modeling. *Journal of Atmospheric and Solar-Terrestrial Physics*, 70(5):803–819, March 2008a. ISSN 13646826. doi: 10.1016/j.jastp.2007.11.001. 88

W.K. Tobiska, B.R. Bowman, and S. Bouwer. Solar and Geomagnetic Indices for the JB2008 Thermosphere Density Model, 2008b. xx, 63, 64, 65, 66, 67, 72

P. Touboul, E. Willemenot, B. Foulon, and V. Josselin. Accelerometers for CHAMP, GRACE and GOCE space missions: synergy and evolution. *Boll. Geof. Teor. Appl.*, 40:321–327, 1999. 51

J.M. Wright, T.J.L. Lennon, R.W. Correll, N.A. Ostenso, W.T. Huntres Jr., J.F. Devine, P. Crowley, and J.B. Harrison. The National Space Weather Program Strategy Plan.pdf, 1995. 3

S.C. Wu, G. Kruizinga, and W. Bertiger. Algorithm Theoretical Basis Document for GRACE Level-1B Data Processing V1.2. Technical report, Jet Propulsion Laboratory, 2006. 26

M. Yamada, R. Kulsrud, and H. Ji. Magnetic reconnection. *Reviews of Modern Physics*, 82(1): 603–664, March 2010. ISSN 0034-6861. doi: 10.1103/RevModPhys.82.603. URL http://link.aps.org/doi/10.1103/RevModPhys.82.603. 9

K. Zahnle and J.C.G. Walker. Evolution of solar ultraviolet luminosity. *Rev. Geophys. Space Phys.*, 20: 280–292, 1982. 1, 79

T.V. Zaqarashvili, R. Oliver, J.L. Ballester, M. Carbonell, M.L. Khodachenko, H. Lammer, M. Leitzinger, and P. Odert. Rossby waves and polar spots in rapidly rotating stars: implications for stellar wind evolution. *A&A*, 532(A138), 2011. 93